30

037 09

UMI
MICROFILMED 2001

INFORMATION TO USERS

This manuscript has been reproduced from the microfilm master. UMI films the text directly from the original or copy submitted. Thus, some thesis and dissertation copies are in typewriter face, while others may be from any type of computer printer.

The quality of this reproduction is dependent upon the quality of the copy submitted. Broken or indistinct print, colored or poor quality illustrations and photographs, print bleedthrough, substandard margins, and improper alignment can adversely affect reproduction.

In the unlikely event that the author did not send UMI a complete manuscript and there are missing pages, these will be noted. Also, if unauthorized copyright material had to be removed, a note will indicate the deletion.

Oversize materials (e.g., maps, drawings, charts) are reproduced by sectioning the original, beginning at the upper left-hand corner and continuing from left to right in equal sections with small overlaps.

Photographs included in the original manuscript have been reproduced xerographically in this copy. Higher quality 6" x 9" black and white photographic prints are available for any photographs or illustrations appearing in this copy for an additional charge. Contact UMI directly to order.

Bell & Howell Information and Learning
300 North Zeeb Road, Ann Arbor, MI 48106-1346 USA
800-521-0600

UMI®

ANGLE-RESOLVED SECOND HARMONIC LIGHT SCATTERING FROM COLLOIDAL SUSPENSIONS AND SECOND HARMONIC PARTICLE MICROSCOPY

Ningping Yang

A DISSERTATION

in

PHYSICS AND ASTRONOMY

Presented to the Faculties of the University of Pennsylvania in Partial Fulfillment of the Requirements for the Degree of Doctor of Philosophy

2001

Arjun G. Yodh

Supervisor of Dissertation

Randall D. Kamien

Graduate Group Chairperson

UMI Number: 3003709

UMI®

UMI Microform 3003709

Copyright 2001 by Bell & Howell Information and Learning Company.
All rights reserved. This microform edition is protected against
unauthorized copying under Title 17, United States Code.

Bell & Howell Information and Learning Company
300 North Zeeb Road
P.O. Box 1346
Ann Arbor, MI 48106-1346

To Yunfeng and Jessica

ACKNOWLEDGEMENTS

I am most grateful to my advisor, Professor Arjun G. Yodh, for his financial support and for his guidance throughout this project. His original ideas and his critical discussions have benefited me the most. His professional approach towards the scientific research and his tireless working attitude in solving scientific problems have always inspired me, both in lab and in real world. I thank him for all his help.

I would also like to thank Dr. Mohsen Yeganeh for writing an excellent thesis and for his willingness to discuss problems when I first set foot in nonlinear optics. His thesis becomes my favorite introductory material in nonlinear optics. I also like to thank Dr. William E. Angerer, who actually helped me with my first hands-on experience on nonlinear optical experiments. I spent significant periods of time throughout this project with him. I enjoyed the discussion with him and certainly thank him for sharing his knowledge and the collaboration with him especially in the nonlinear microscope project. I would also like to thank Professor Robert J. Hunter, the author of the popular book, "Foundations of Colloid Science", for sharing with me his knowledge in the optical experiment in colloid science. His rigorous scientific approach to the problems and his numerous timely help greatly help my understanding of colloid science. I would also like to thank Professor Tony F. Heinz for sharing his theoretical work with us.

I thank Professor Anthony F. Garito and the graduate stuents in his group for

the convenient access to their optical measurement equipment. I thank Professor Alan Johnson, Dr. Rad Antonov and Dr. Zhiming Yu for helping me design and manufacture the sample mask. Without their help, the project won't move forward as smoothly.

I benefited a lot from the discussions with Dr. Hongfei Wang. Especially, his experience on Malachite Green dye sample preparation and the adsorption isotherm have greatly helped my project. I also enjoyed the time when we tried to figure out the mechanism behind SHG from single particle.

It has been a great pleasure and a valuable opportunity to work with all the graduate students, postdocs in Arjun's group. In particular, I would like to thank Drs. John Crocker, Eric Weeks, Tony Dinsmore, Cecil Cheung, Joe Culver, Xingde Li, Ritu Verma, Amani Gandour, Mohammad F. Islam, Subrata Sanyal, Keng-hui Lin, Jian Zhang, Daniel Chen and Ahmed Alsayed. I enjoyed working with them and thank them for all the help and advice.

I also enjoy the friendship with fellow graduate students in Physics department. In particular, I enjoy all the fun with Zhiming Yu, Yan Gu, Limin Wang, Jing Wang and Hiuming Qiu. The jokes and chattings had been an invaluable part of this endeavor.

My greatest appreciation goes to my wife, Yunfeng and my lovely daughter, Jessica. The love and support they showed over the whole course of the project has been tremendous. Without their continued encouragement, I would not be able to walk

out the lab as I do today.

ABSTRACT

ANGLE-RESOLVED SECOND HARMONIC LIGHT SCATTERING FROM COLLOIDAL SUSPENSIONS AND SECOND HARMONIC PARTICLE MICROSCOPY

Ningping Yang

Arjun G. Yodh

We have carried out two nonlinear optical experiments with colloidal particles. Our first nonlinear optical experiment studied Second-Harmonic Generation (SHG) light scattering from colloidal suspension. In particular, we measured the angle-resolved second-harmonic generation light scattering from suspensions of centrosymmetric micron-size polystyrene spheres with surface-adsorbed dye (malachite green). The second-harmonic scattering angular profiles differ qualitatively from the linear light scattering angular profiles of the same particles. We have investigated these radiation patterns using several polarization configurations and particle diameters. We introduce a simple Rayleigh-Gans-Debye model to account for the SHG scattering anisotropy. The model compares favorably with our experimental data. Our measurements suggest scattering anisotropy may be used to isolate particle nonlinear optical effect from other bulk nonlinear optical effects in suspension.

Our second nonlinear optical experiment studied the Second-Harmonic Generation (SHG) from single micron-size particles. We built a nonlinear optical microscope

for this purpose. We report experimental observations of second harmoinc generation from single micron-size polystyrene (PS), silica, and PolyMethylMethAcrylate (PMMA) spheres on flat substrates by SHG microscopy. At low input light intensities the SH signals depend quadratically on the intensity of the excitation beam, but at larger input intensities some of the SH signals increase exponentially with increasing input intensity. This exponential enhancement depends on particle size and sphere composition. We describe the experiments, report the observations and provide an aproximate analytical framework for understanding our measurements.

Contents

1 Introduction **1**

2 General Theoretical Background on Second-order Nonlinear Optics **8**

2.1 Second-order Nonlinear Wave Equation 8

2.2 Second-order Nonlinear Susceptibility 10

2.2.1 Higher Order Nonlinear Process 13

2.3 SH Electric Field From Colloidal Particle Surfaces: General Discussion 14

2.4 SH Generation From Highly Focused Laser Beams: General Discussion 20

3 Angle-Resolved SHG Scattering From Colloidal Suspension: Experimental **27**

3.1 Experimental Setup 27

3.2 Ti:Al_2O_3 Laser 32

3.2.1 Pulse Width 39

3.3 Autocorrelation 43

3.4 Signal Detection 46

4 Angle-resolved SHG Scattering From Colloidal Suspension: Sample 51

4.1 Malachite Green 51

4.2 Polystyrene Particle 53

4.3 Sample Preparation 55

4.4 Adsorption Isotherm of Malachite Green on Polystyrene Particles . . 56

4.4.1 Experimental Setup for Adsorption Isotherm 57

4.4.2 Results of Adsorption Isotherms and Discussions 59

4.5 SHG Dependence on Particle Concentration 63

4.6 Effect of Electrolyte on SH Generation 63

5 Angle-resolved SHG Scattering From Colloid Suspension: Data and Analysis 69

5.1 Two-photon Angular Profile for Malachite Green Solution Only . . . 69

5.2 SHG Scattering Angular Profile From Colloidal Suspension: Raw Measurements 77

5.3 SHG Scattering Angular Profile From Colloidal Suspension: Background Substraction 77

5.4 Rayleigh-Gans-Debye Approximation For SHG Light Scattering . . . 84

5.4.1 Calculations of Surface Nonlinear Polarizations 86

5.4.2 Complete Solution of Nonlinear Wave Equation 90

5.4.3 Experimentally Detected SHG field 94

5.5 Data Analysis Using the RGD Approximation 94

5.5.1 Discussion On s-polarized SHG Radiation 96

5.6 General Comparision with SHG Rayleigh scattering 97

6 SHG Microscopy of Single Micron-size Particle On a Substrate 108

6.1 SHG Microscopy for Single Particle: Apparatus 109

6.2 Synchronous Photon Counting 112

6.3 Sample Registering 115

6.4 SHG From Single Micron-size Particle 117

6.5 Discussion 118

7 Linear Optical Measurements 129

7.1 Measurements of Particle Index of Refraction 129

7.2 Measurement of Focus Spot Size of Microscope Objective 133

8 Conclusion 144

A Theory of Dye Adsorption on Particles 147

B Surface Potential of Charged Colloidal Particle 150

C Derivation of Integral in Equation (5.13) 155

D Derivation of Integral (5.19) 157

E Rayleigh-Gans-Debye Approximation for Linear Light Scattering 160

F Coding for Mie Scattering Calculations 165

List of Figures

2.1 Wave-mixing example in a three-level system. Resonance is at $2\omega_0$. . 11

2.2 Schematic view of MG adsorption on particle surface. 16

2.3 Model for two MG molecules adsorbed on particle surface. 18

2.4 $|1 - e^{iqL}|^2$ versus L curve 24

2.5 SHG rotational symmetry of Si(100) and Si(111) measured by the non-linear optical microscope. 26

3.1 Schematic of experimental setup for angle-resolved SHG scattering from colloid suspension. 29

3.2 Prism pair. 30

3.3 Transmission spectrum of BG39 filter. 33

3.4 Schematic of Ti:Al_2O_3 laser. 35

3.5 Slit size and beam cross section for Ti:Al_2O_3 laser 38

3.6 Chirp in a pulse. 40

3.7 GVD compensation. 41

3.8 Schematic of autocorrelator. 44

3.9 Diagram showing type-I phase matching. 45

3.10 Quantum Efficiency for Hamamatsu PMT model R4220P. 48

3.11 Pulse height distribution curve for PMT. 49

4.1 Molecular structure of Malachite Green hydrochloride. 52

4.2 Experimental setup for adsorption isotherm. 58

4.3 Adsorption isotherm for Malachite Green on polystyrene particles. . . 60

4.4 MG adsorption on PS particles: linear region 62

4.5 SHG Intensity versus colloidal particle density. 64

4.6 SHG dependence on electrolyte concentration for suspension with only colloidal particles. 67

4.7 SHG dependence on electrolyte concentration for PS+MG suspension. 68

5.1 Schematic of experimental geometry for SHG scattering from colloidal suspensions. 71

5.2 Angular profile for two-photon fluorescence signal from MG solution: p-out case 73

5.3 Angular profile for two-photon fluorescence signal from MG solution: s-out case 74

5.4 Schematic of Malachite Green electronic states. 75

5.5 Malachite Green two-photon excited fluorescence spectrum. 76

5.6 Raw measurement for SHG scattering from colloidal suspension. The particle size is 980nm in diameter, the polarization configuration is p-in/p-out. 78

5.7 Raw measurement for SHG scattering from colloidal suspension. The particle size is 700nm in diameter, the polarization configuration is p-in/p-out. 79

5.8 Raw measurement for SHG scattering from colloidal suspension. The particle size is 510nm in diameter, the polarization configuration is p-in/p-out. 80

5.9 Raw measurement for SHG scattering from colloidal suspension. The particle size is 980nm in diameter, the polarization configuration is s-in/p-out. 81

5.10 Raw measurement for SHG scattering from colloidal suspension. The particle size is 700nm in diameter, the polarization configuration is s-in/p-out. 82

5.11 Raw measurement for SHG scattering from colloidal suspension. The particle size is 510nm in diameter, the polarization configuration is s-in/p-out. 83

5.12 The linear form factor comparison between Mie theory and RGD approximation. 87

5.13 The coordinate system for SHG RGD Model. 89

5.14 The directional relationship between various vectors in SHG RGD theory 93

5.15 SHG scattering from colloidal suspension. p-in/p-out and D=980nm. 99

5.16 SHG scattering from colloidal suspension. p-in/p-out and D=700nm. 100

5.17 SHG scattering from colloidal suspension. p-in/p-out and D=510nm. 101

5.18 SHG scattering from colloidal suspension. s-in/p-out and D=980nm. 102

5.19 SHG scattering from colloidal suspension. s-in/p-out and D=700nm. 103

5.20 SHG scattering from colloidal suspension. s-in/p-out and D=510nm. 104

5.21 Raw measurement for SHG scattering from colloidal suspension. p-in/s-out and d=980nm. 105

5.22 Extracted signal for SHG scattering from colloidal particle. p-in/s-out and D=980nm. 106

5.23 Schematic view of SH Rayleigh scattering model and our model . . . 107

6.1 Apparatus for SHG microscope. 111

6.2 The timing relationship between chopper and photoncounter gates. . 114

6.3 Sample mask and SHG scan versus laser spot position for SHG microscope 116

6.4 SHG from PS beads versus input peak intensity 119

6.5 SHG from PMMA beads versus input peak intensity 120

6.6 SHG from silica beads versus input peak intensity 121

6.7 SHG From PS beads: transition region 126

7.1 Experimental setup for linear light scattering form factor measurement. 132

7.2 Linear light scattering form factor measurement. 134

7.3 Schematic view for the measurement of objective focus spot size. . . . 137

7.4 Schematic showing the definition of beam diameter at different positions. 138

7.5 The scanned laser beam profile at position z_1. 142

7.6 The scanned laser beam profile at position z_2. 143

B.1 Double layer model for colloidal solution 152

E.1 Schematic of coordinate system for Rayleigh-Gans-Debye approximation for linear light scattering. 161

E.2 Geometrical relationship between $\mathbf{k}_i$, $\mathbf{k}_s$ and $\mathbf{Q}$. 162

F.1 Coordinate system for Mie calculations. 166

List of Tables

2.1 Non-zero Elements of Γ_{ijkl} For Si(100) 25

3.1 Characteristics of Ti:Al_2O_3 Laser 34

4.1 Specifications of Malachite Green Dye 53

4.2 Specifications of Polystyrene Microparticles 54

4.3 Geometrical parameters of lens used in Fig. 4.2 57

4.4 Fitting parameters for MG Adsorption Isotherm 61

6.1 Fitting parameters for quadratic region 123

6.2 Fitting Parameters for Transition Region 127

7.1 χ^2 Values For Our Polystyrene Particles 133

7.2 χ^2 Values For Our PMMA Particles 135

7.3 χ^2 Values For Our Silica Particles 135

D.1 The Integral Value For Each Term in Equation (D.1) 159

Chapter 1

Introduction

Linear light scattering from spherical particles has been well studied, is rigorously based upon Mie theory [1, 2], and currently provides the basis for characterization of a wide variety of particle dispersions ranging from colloids and emulsions to cells. However, the linear light scattering technique has drawbacks. For example, it is relatively insensitive to the changes or variations occurring at the surfaces or interfaces. It is therefore difficult to study surface processes using the linear light scattering technique. The nonlinear optical technique, especially Second-Harmonic Generation (SHG) and Sum-Frequency Generation (SFG), are particularly useful in this regard due to its intrinsic surface sensitivity [3, 4, 5, 6, 7].

SHG from centrosymmetric media is forbidden in the electric dipole approximation. However, bulk symmetry is effectively broken at the interface between two dissimilar media. This interface region is usually defined as the atomic or molecular layers that constitute the junction between the two dissimilar media. Because bulk

symmetry is broken, SHG emission is dipole-allowed from interfaces. In many systems, this interface SHG dominates the overall signal and one can study the surface process using SHG with great success.

The application of nonlinear optical techniques to study solutions and suspensions began with the advent of high-power laser. However, due to above-mentioned suppression of SHG from bulk solutions, the experimentally observed second-order light scattering from solution has long been incoherent Hyper-Rayleigh scattering [8, 9, 10, 11]. Hyper-Rayleigh scattering originates from the density and orientational fluctuations of solution molecules which break the centrosymmetry locally. In past 10 years, Hyper-Rayleigh scattering has found some interesting applications. Clays et. al. [12, 13, 14, 15, 16] used Hyper-Rayleigh scattering to measure the first hyperpolarizability β of ogranic molecules without having to independently determine the dipole moment μ, and the second hyperpolarizability γ as in the traditional electric-field-induced second-harmonic generation techniques [17, 18]. Hyper-Rayleigh scattering has also been used to probe the spatial orientational correlations between chromophores in polymer films. Many other different groups also independently reported silimar results [19, 20, 21, 22]. Hyper-Rayleigh scattering was also used in some new materials [23, 24, 25]. For example, Vance et. al. used Hyper-Rayleigh scattering to study the nanocrystalline gold particle suspensions and they found enormous Hyper-Rayleigh scattering. On the theoretical side, Andrews et. al. [26] developed

the general theory for treating the second-order light scattering from the randomly oriented species suspensions; they found a relationship between the coherent process of second harmonic generation and its incoherent counterpart, Hyper-Rayleigh scattering. Heesink's group and Levine's group calculated theoretical expressions for the hyperpolarizability tensor components of dye molecules and the effects of molecular interactions on hyperpolarizabilities [27, 28]. Cammi et. al. computed the macroscopic susceptibilities in solution generally [29]. There are also some reports of observations of Hyper-Raman scattering from the solutions [30, 31].

It was not until recently that coherent SHG from centrosymmetric solution containing micron-size colloidal particles was reported [32]. This work was important in that, by using micron-size particle and by adsorbing nonlinear dye molecules on the surfaces of particles, one effectively obtains a large nonlinear source term on the surface of the particle. The not-so-small particle size insures that the phase cancellation, which occurs for much smaller particles, is eliminated and strong coherent SH radiation is achieved. Further experimental studies [33, 34, 35, 36, 37] demonstrate the superiority of SHG on the investigations of surface processes occurring on the particle surface. For example, the adsorption dynamics of dye on particles has been investigated. On the theoretical front, Dadap [38] et. al. calculated SHG scattering from spherical particles when particle size is substantially smaller than light wavelength. That is, the case of SH generation light scattering in the Rayleigh region.

Our angle-resolved SHG scattering from colloidal suspensions is motivated by these observations. Unlike linear light scattering, where people are familiar with and fully understand the process, SHG light scattering from particles is unknown territory. Though important as a fundamental study, SHG scattering from particles has rarely been studied either theoretically or experimentally. The reason for this is partly because the SHG signal from solutions is very small, and partly because the theory describing SHG scattering is much more complicated than its linear counterpart. In this thesis, we present the first experimental studies on the angle-resolved SHG light scattering from micron-size particles. Our studies reveal differences between linear and nonlinear particle scattering. Most notably, the forward scattering for SHG is forbidden, while in the linear case it is the strongest contribution. Also, the in-plane, s-polarized SHG scattering is found to be forbidden regardless of input polarization configuration (again different from the linear case). We have carefully studied the different contributions to our raw measurements and have extracted the SHG signal from the particles. We then derived the non-linear analog of Rayleigh-Gans-Debye (RGD) approximation for SHG scattering, and used RGD to analyze our results. Reasonable agreement was achieved.

In second part of this thesis, we present SHG microscopy studies on single micron-size particles. Nonlinear optical microscopy was first suggested by Robert Hellwarth and Paul Christensen in 1974 [39, 40]. They imaged the structure of a polycrys-

talline nonlinear material, ZnSe, by utilizing the fact that the second-order nonlinear susceptibility of a ZnSe polycrystal varies spatially and is detectable by SHG approach. This is potentially valuable especially when conventional linear microscopy is unable to resolve structural inhomogeneities. For example, linear microscopy has serious limitations in samples that have small (or negligible) variations in the refractive indices accompanying the structural inhomogeneities. However, these structural inhomogeneities are invariably accompanied by large spatial variations in the nonlinear refractive indices. Nonlinear optical processes are highly sensitive to material symmetry, and therefore, using SHG, one can detect structures previously invisible in the linear microscope. Since their pioneering work, several groups also reported their studies on this nonlinear optical microscope [41, 42, 43, 44, 45, 46, 47].

We built a SHG microscope system to investigate the response of single micron-size particles. We studied these responses as a function of excitation power intensity, particle type and size. We report the first measurements of SHG from *single* micron-size particles, and we compare their nonlinear responses over a range of particle type (e.g., Polystyrene (PS), poly-methyl-methacrylate (PMMA), and silica) and size (e.g., diameters between 1 to 5 μm). At relatively low input powers, the particle SHG signals depend on the square of the fundamental excitation beam intensity. At higher input powers however, reversible exponential SHG responses are observed from many of the particles up to the point where the signal saturates and the particle is dam-

aged. This exponential enhancement depends on particle size and sphere composition. We describe the experiments and parameterize observations. We also suggest some possible mechanisms for the enhanced SHG signals.

This thesis is organized as follows. In Chapter 2 we introduce the general discussion of second-order nonlinear optics and where relevant, the discussion about the symmetry effect on the Second-Harmonic Generation. We also discuss in general the origin for the SHG generation for our sample colloidal solutions. We leave the rigorous theoretical derivation to Chapter 5. We also discuss the Gaussian beam focusing which will be relevant when we try to handle the complexities in SHG microscope project.

In Chapter 3 we discuss the experimental setup for the SHG scattering from colloidal solutions. We discuss the laser source, the detection system and some relevant experimental techniques. In Chapter 4 we discuss the colloidal sample and its preparations. Some relevant measurements of experimental parameters are presented too. In Chapter 5, we present our major results on angle-resolved SHG scattering from colloidal suspensions. We detail our data analysis and present the SH generation Rayleigh-Gans-Deybe theory which we use to fit our experimental data. We compare our results with the RGD theory. We also compare RGD for the SHG scattering and for the linear scattering cases.

We present the experimental setup for SHG microscopy project in Chapter 6.

We discuss the implementation of system and some important aspects in the sample preparation and characterization. We report results, and analyze the data and suggest the possible mechanism for the observed phenomenon. We also comment on the complexity of this problem. In Chapter 7, we discuss the linear optical methods that we used to characterize the particle index of refraction and the microscope objective focus spot size. A brief conclusion is given in Chapter 8.

Chapter 2

General Theoretical Background on Second-order Nonlinear Optics

In this chapter, we will introduce the basic theory behind Second-Harmonic Generation. We will also examine aspects of SHG relevant to colloidal particles and to our nonlinear microscope.

2.1 Second-order Nonlinear Wave Equation

When an optical medium is subjected to light excitation, the induced polarization can be expressed in a general form [48]:

$$\mathbf{P}(\mathbf{k},\omega) = \mathbf{P}^{(1)}(\mathbf{k},\omega) + \mathbf{P}^{(2)}(\mathbf{k},\omega) + \mathbf{P}^{(3)}(\mathbf{k},\omega) + ..., \tag{2.1}$$

with

$$\begin{aligned}
\mathbf{P}^{(1)}(\mathbf{k},\omega) &= \chi^{(1)}(\mathbf{k},\omega)\cdot\mathbf{E}(\mathbf{k},\omega), \\
\mathbf{P}^{(2)}(\mathbf{k},\omega) &= \chi^{(2)}(\mathbf{k}=\mathbf{k}_i+\mathbf{k}_j,\omega=\omega_i+\omega_j):\mathbf{E}(\mathbf{k}_i,\omega_i)\mathbf{E}(\mathbf{k}_j,\omega_j), \qquad (2.2)\\
\mathbf{P}^{(3)}(\mathbf{k},\omega) &= \chi^{(3)}(\mathbf{k}=\mathbf{k}_i+\mathbf{k}_j+\mathbf{k}_l,\omega=\omega_i+\omega_j+\omega_l):\mathbf{E}(\mathbf{k}_i,\omega_i)\mathbf{E}(\mathbf{k}_j,\omega_j)\mathbf{E}(\mathbf{k}_l,\omega_l),
\end{aligned}$$

where $\mathbf{P}^{(n)}$ is nth-order polarization and $\chi^{(n)}$ is nth-order susceptibility which is a (n+1)th rank tensor. $\mathbf{k}$ is the wave vector of light and ω is the angular frequency of light. $\mathbf{E}(\mathbf{k}_i, \omega_i)$ represents the incident light field with wave vector $\mathbf{k}_i$ and frequency ω_i.

In Second-Harmonic Generation, the radiated light frequency is twice the input light frequency, i.e. $\omega = 2\omega_0$, with ω_0 the fundamental beam frequency. The relevant nonlinear source polarization is:

$$\mathbf{P}^{(2)}(\mathbf{k}, \omega) = \chi^{(2)}(\mathbf{k} = \mathbf{k}_i + \mathbf{k}_j, \omega = 2\omega_0) : \mathbf{E}(\mathbf{k}_i, \omega_0)\mathbf{E}(\mathbf{k}_j, \omega_0). \tag{2.3}$$

With knowledge of $\chi^{(2)}(\mathbf{k} = \mathbf{k}_i + \mathbf{k}_j, \omega = 2\omega_0)$, one can solve for the second-order nonlinear source polarization, and then compute its radiated fields.

This second-order nonlinear polarization will radiate at frequency $\omega = 2\omega_0$. The radiated electric field is governed by the nonlinear wave equation:

$$\nabla \times \nabla \times \mathbf{E}(\omega) + \frac{\epsilon(\omega)}{c^2}\frac{\partial^2}{\partial t^2}\mathbf{E}(\omega) = -\frac{4\pi}{c^2}\frac{\partial^2}{\partial t^2}\mathbf{P}^{(2)}(\omega). \tag{2.4}$$

Here ϵ is the frequency-dependent linear dielectric constant of the medium, c is speed of light. Eq. 2.4 is basic equation governing the relationship between nonlinear source polarization and the radiated electric field. We will start from this equation in Chapter 5 to derive the scattering SHG field in Rayleigh-Gans-Debye approximation.

2.2 Second-order Nonlinear Susceptibility

Second-order nonlinear susceptibility $\chi^{(2)}$ is generally derived using the density matrix formalism [48]. The microscopic expressions for second-order susceptibility describing second-harmonic generation in the dipole approximation is:

$$\begin{aligned}\chi^{(2)}_{ijk}(\omega = 2\omega_0) &= -2N\frac{e^3}{\hbar^2}\sum_{png}[\frac{< g|r_i|n >< n|r_j|p >< p|r_k|g >}{(\omega - \omega_{ng} + i\Gamma_{ng})(\omega_0 - \omega_{pg} + i\Gamma_{pg})} \\ &+ \frac{< g|r_j|n >< n|r_i|p >< p|r_k|g >}{(\omega - \omega_{pn} + i\Gamma_{pn})(\omega_0 + \omega_{ng} - i\Gamma_{ng})} \\ &+ \frac{< g|r_j|n >< n|r_i|p >< p|r_k|g >}{(\omega + \omega_{np} - i\Gamma_{np})(\omega_0 - \omega_{pg} + i\Gamma_{pg})} \\ &+ \frac{< g|r_j|n >< n|r_k|p >< p|r_i|g >}{(\omega + \omega_{pg} - i\Gamma_{pg})(\omega_0 + \omega_{ng} + i\Gamma_{ng})}]\rho_g^{(0)}.\end{aligned} \tag{2.5}$$

Here (i, j, k) are explicit Cartesian coordinates. N is the number of atoms or molecules per unit volume. $|g>$, $|p>$, and $|n>$ are eigenstates of the unperturbed system. $\rho_g^{(0)}$ corresponds to the unperturbed density of the state at ground state $|g>$. Γ represents the damping factor. For example, Γ_{np}^{-1} is the relaxation time of a coherence created between the states $|n>$ and $|p>$. $\hbar\omega_{np}$ is the energy difference between states $|n>$ and $|p>$. The different terms in equation (2.5) correspond to different time ordering of the photons. The product of the three matrix elements in each term corresponds to the coupling of the photons with matter in three separate steps. As an example, $(r_i)_{gn}(r_j)_{np}(r_k)_{pg}$ corresponds to: (1) the coupling of the ground state, $|g>$, to the excited state, $|p>$, with the k component of the field in the first step of the mixing, (2) the coupling of the excited state, $|p>$, to another excited state, $|n>$, with the j

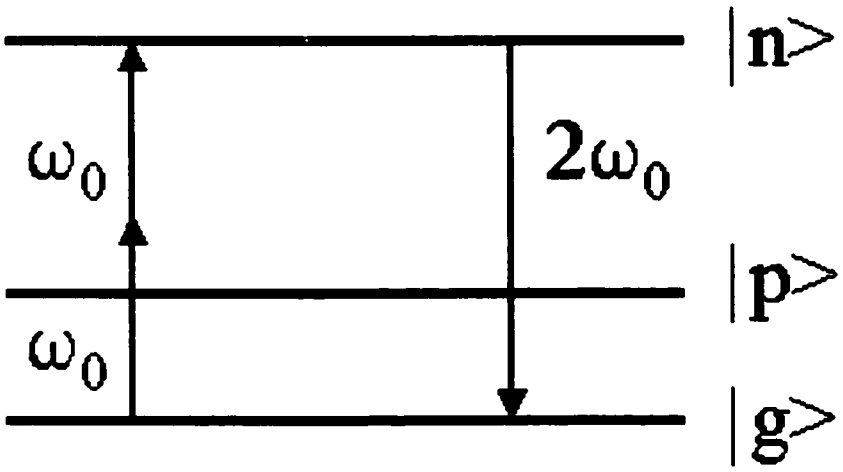

Figure 2.1: Wave-mixing example in a three-level system. Resonance is at $2\omega_0$.

component of field in the second step, and (3) the coupling of the excited state, $|n>$, with the ground state, $|g>$, with the i component of the field in the final step. The summation indicates that the process must go over all possible excited states. One example of the mixing processes is shown in Fig. 2.1.

One important conclusion that can be drawn from equation (2.5) is that for centrosymmetric system, $\chi^{(2)}$ is always zero. This stems from the fact that under inversion symmetry the product of three matrix elements, independent of the subscripts i, j, and k, is always zero. This important result tells us that in the dipole approximation, SHG is forbidden in a centrosymmetric system. Therefore, in isotropic

liquid solutions or colloidal suspensions, one would expect no SHG (in the dipole approximation). If symmetry is broken $\chi^{(2)}$ is non-zero. This fact about $\chi^{(2)}$ renders second-order nonlinear optics a powerful tool for studying interfaces [3, 4, 5, 6, 7], where symmetry in the direction normal to the junction (at least) is broken. In the next section, we will briefly discuss SH Generation in higher order approximations.

Another important feature in equation (2.5) is the denominator of each term. From these denominators we see that resonances arise whenever the energy of the incident or second-harmonic photons, $\hbar\omega_0$ or $2\hbar\omega_0$ matches an energy difference between two states in the medium. This property is the basis for nonlinear spectroscopy: an resonant increase in measured SHG signal can be correlated with an electronic or vibrational excitations of the medium. This effect, along with the fact that the nonlinear optical process is sensitive to changes in interface symmetry, combine to make nonlinear optical spectroscopy a powerful tool for studies of surfaces or buried interfaces. A great number of works have focused on many aspects of this problem [3, 4, 49, 5, 6, 50, 7, 51].

Finally, it has to be pointed out that the three-wave mixing process shown in Fig. 2.1 is a virtual process. That is, there need be no population transfer between eigenstates. Population transfer can occur only under some circumstances such as one-photon or two-photon absorption. In one-photon absorption, a single photon excites a material and this process is mediated by linear susceptibility, $\chi^{(1)}$. Two-

photon absorption is a process involving two photons simultaneously. Two-photon adsorption is mediated by the third-order nonlinear susceptibility, $\chi^{(3)}$ [52].

2.2.1 Higher Order Nonlinear Process

The discussions in previous sections all consider SHG within the dipole approximation. In reality, higher-order excitation of nonlinear waves do exist, though they are often small compared to the dipole contributions. In system with centrosymmetry, when dipole contribution is suppressed, higher order nonlinear processes become more important and in some cases are observable. We briefly summarize the theory for higher order contributions to SHG.

The general nonlinear polarization including both dipole and higher order multipole contributions are:

$$P_i^{(\omega)} = \chi_{ijk}^{(\omega)} : \mathbf{E}_j^{(\omega_0)}\mathbf{E}_k^{(\omega_0)} + \Gamma_{ijkl}^{(\omega)}\mathbf{E}_j^{(\omega_0)}\nabla_k\mathbf{E}_l^{(\omega_0)}, \tag{2.6}$$

where as usual, ω_0 and ω are fundamental and SH frequency respectively, and (ijk) represents Cartesian coordinates. The first term is the dipole contribution, which is a function of the local electric field. The second term arises from the nonlocal response of the system, which is due to an expansion of $\mathbf{P}$ in terms of the derivatives of the electric field. This nonlocal response carries the electric quadrupole and magnetic dipole contributions. Γ is a fourth-rank tensor relating the field and its gradient to the nonlinear polarizations. For cubic symmetry, an alternative expression for the

second term in equation (2.6) is [53, 54, 55, 56]:

$$P^{(\omega)}_{i,higher\_order} = (\delta - \beta - 2\gamma)(\mathbf{E}\cdot\nabla)E_i + \beta E_i(\nabla\cdot\mathbf{E}) + \gamma\nabla_i(\mathbf{E}\cdot\mathbf{E}) + \zeta E_i\nabla_i E_i. \quad (2.7)$$

Note that δ, β, γ, and ζ are phenomenological constants. Also note that the first three terms are isotropic in character, and the last term is anisotropic with respect to the orientation of the material.

As in dipole case, the fourth-rank tensor Γ has only a few independent non-zero elements. From the symmetry properties of the relevant material, one can find out all those non-zero independent elements and thus greatly simplify the treatment for the higher-order contributions. In this thesis, because our SHG signal is dipole dominated, we will not consider higher-order contributions further. Note however, if our particle size becomes much smaller than the wavelength, then the higher-order contributions will be non-negligible, as is the case for SHG scattering from Rayleigh particles [38].

2.3 SH Electric Field From Colloidal Particle Surfaces: General Discussion

As shown in section 2.2, an isotropic solution or suspension won't produce SH Generation in the dipole approximation. This is true for solutions containing molecules much smaller than the optical wavelength, and wherein the whole material is effectively centrosymmetric. However, when particles in solution have a size comparable to the input wavelength, coherent SH radiation is possible. To understand this point,

consider the sample colloidal suspension of our experiment. Our colloidal suspension consists of micron-size particles whose surfaces are uniformly covered with Malachite Green (MG) dye. A schematic view of the sample is in Fig. 2.2. Each MG molecule is about $\sim 5\AA$ in length, much smaller than the optical wavelength and the particle diameter. Due to electrostatic interactions, all MG molecules are oriented radially on the particle surface [32]. Each molecule has a non-zero non-linear hyperpolarizability $\alpha^{(2)}$ along the radial direction. The particle SHG is dominated by this surface nonlinearity. The question of SH generation amounts to whether the emission from oppositely oriented MG molecules on the particle surface will destructively interfere to produce no SH radiation. We therefore simplify our discussion, and consider only two oppositely oriented molecules as shown in Fig. 2.3. Where we assume the fundamental beam is along z-direction, the displacement vector between these two molecules is $\mathbf{L} = \mathbf{r_2} - \mathbf{r_1}$, the observation direction is at a distant point at an angle θ with respect to z-direction in the scattering plane of xz. Assume the fundamental beam electric field is $\mathbf{E}_0(\omega_0, \mathbf{r}) = \mathbf{E}_0 e^{i(\mathbf{k}_{\omega_0}\cdot\mathbf{r} - \omega_0 t)}$ ($\mathbf{k}_{\omega_0} = k_{\omega_0}\hat{e_z}$), then from equation 2.4, replacing $\nabla \times \nabla \times$ with $-\nabla^2$, we get:

$$[\nabla^2 + k_{2\omega_0}^2]\mathbf{E}_{2\omega_0}(\mathbf{r}) = -\frac{4\pi(2\omega_0)^2}{c^2}\mathbf{P}_{2\omega_0}^{NL}(\mathbf{r}). \tag{2.8}$$

Here $k_{2\omega_0}^2 = \frac{\epsilon(2\omega_0)}{c^2}(2\omega_0)^2$, $\mathbf{P}_{2\omega_0}^{NL}$ is the nonlinear source polarization on the particle surface.

To solve this wave equation, we use the Green Function method. The appropriate

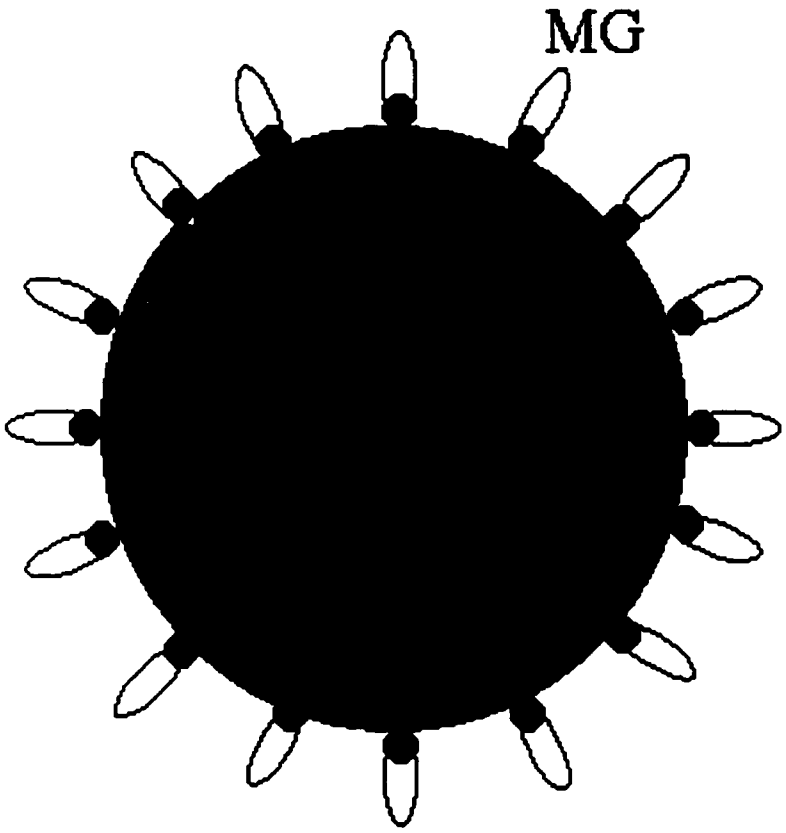

Figure 2.2: Schematic view of MG adsorption on particle surface. MG molecules are radially oriented.

Green function is [57]

$$G_{2\omega_0}(|\mathbf{r}-\mathbf{r}'|) = \frac{e^{ik_{2\omega_0}|\mathbf{r}-\mathbf{r}'|}}{|\mathbf{r}-\mathbf{r}'|}. \tag{2.9}$$

Therefore, the general solution for equation (2.8) is [57]

$$\mathbf{E}_{2\omega_0}(\mathbf{r}) = \frac{(2\omega_0)^2}{c^2}\int d^3\mathbf{r}'\frac{e^{ik_{2\omega_0}|\mathbf{r}-\mathbf{r}'|}}{|\mathbf{r}-\mathbf{r}'|}\mathbf{P}^{NL}_{2\omega_0}(\mathbf{r}'). \tag{2.10}$$

Note that $\mathbf{r}$ corresponds to the detector coordinate, $\mathbf{r}'$ corresponds to the nonlinear source coordinate and has to be integrated over the source distribution.

In our simplified case where only two MG molecules are oriented oppositely, we can write

$$\mathbf{P}^{NL}_{2\omega_0}(\mathbf{r}') \propto \alpha^{(2)}(\delta(\mathbf{r}'-\mathbf{r}_1) - \delta(\mathbf{r}'-\mathbf{r}_2))e^{i2\mathbf{k}_{\omega_0}\cdot\mathbf{r}'}\hat{e}'_r. \tag{2.11}$$

Here the "-" sign is from the fact that the two molecules point in opposite directions. Using the far field approximation ($r \gg r'$)

$$|\mathbf{r}-\mathbf{r}'| = \sqrt{r^2+r'^2-2\mathbf{r}\cdot\mathbf{r}'} = r\sqrt{1+\frac{r'^2}{r^2}-2\frac{\mathbf{r}}{r}\cdot\frac{\mathbf{r}'}{r}} \approx r(1-\frac{\mathbf{r}}{r}\cdot\frac{\mathbf{r}'}{r}) = r-\hat{n}\cdot\mathbf{r}'$$

and $\frac{1}{|\mathbf{r}-\mathbf{r}'|} \sim \frac{1}{r}$ (leading term) [57], where $\hat{n} = \frac{\mathbf{r}}{r}$, then we get

$$|\mathbf{E}_{2\omega_0}(\mathbf{r})| \propto \alpha^{(2)}(1-e^{i\mathbf{q}\cdot\mathbf{L}}). \tag{2.12}$$

Here, $\mathbf{q} \equiv 2\mathbf{k}_{\omega_0} - \mathbf{k}_{2\omega_0}$ is the wave vector mismatch, it is somewhat akin to the scattering vector in linear light scattering. Equation (2.12) relates the radiated SH field to the particle size in a simplified but physically meaningful way. The minus sign is the direct result of oppositely oriented molecules. From equation (2.12), we obtain

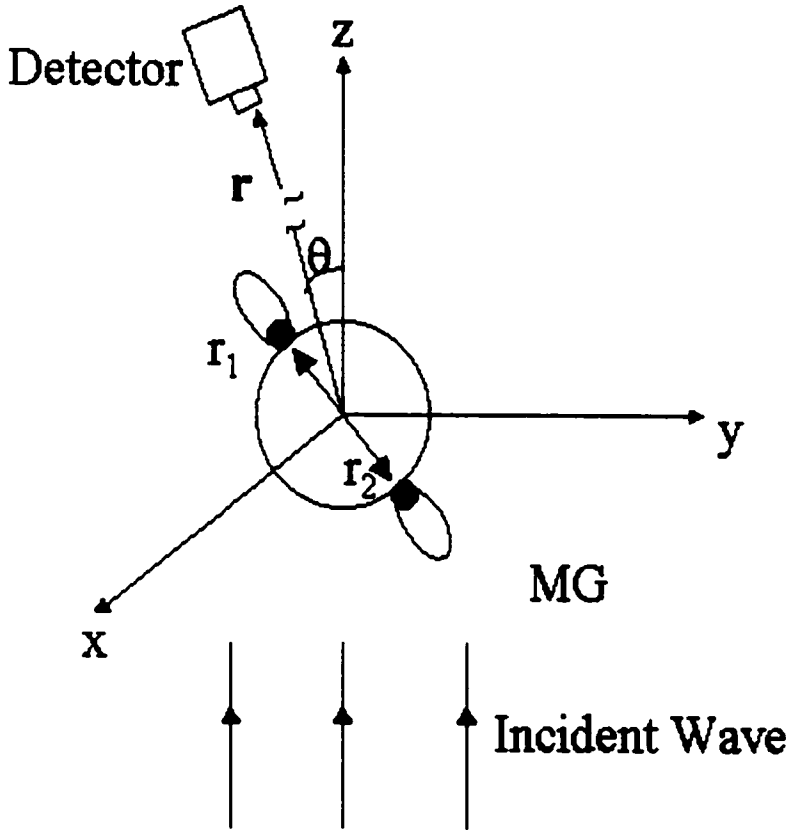

Figure 2.3: A simplified model showing only two oppositely oriented molecules on particle surface. θ is the scattering angle. $\mathbf{r}_1$ and $\mathbf{r}_2$ are position vectors for these two MG molecules respectively. $\mathbf{r}_1 = -\mathbf{r}_2$.

the following conclusions:

(1) When the separation L between the molecules is much less than the wavelength of light, i.e. $\mathbf{q} \cdot \mathbf{L} \ll 1$, $E_{2\omega_0} \cong 0$. This means that there is no SH radiation when particle size is much smaller than the wavelength. This is the case of centrosymmetry we discussed in section 2.2.

(2) When the separation L between the molecules is comparable to wavelength such that $\mathbf{q} \cdot \mathbf{L} \sim \pi$, then there will be constructive interference between these two molecules. It is on the length scale of microns that one must consider the interference described herein.

In Fig. 2.4, we plot the factor $|1 - e^{i\mathbf{q}\cdot\mathbf{L}}|^2$ versus L, the particle size. We use $\lambda = 840nm$, $\Delta n = n(2\omega_0) - n(\omega_0) \sim 0.01$. It is clear that the SH signal approaches zero as the particle size goes to zero, while SH radiation is non-zero when the particle size is comparable with the wavelength. Therefore, in our sample system where we cover the micron-size particles with nonlinear molecules, even though the whole suspension is still macroscopically isotropic, we can obtain coherent SH radiation from such system. And what is more important, such SH radiation is generated from the surface of centrosymmetric particles in isotropic solutions. This property provides a useful method for investigating the surface processes of relatively small particles in

a centrosymmetric environment. The ability to detect coherent SHG in our sample suspension is based upon this. In Chapter 5, we will look at the SHG issue from the point of view of Rayleigh-Gans-Debye approximation.

2.4 SH Generation From Highly Focused Laser Beams: General Discussion

In the nonlinear microscope experiment, one uses high numerical aperture (N.A.) objectives to focus the input beam into the sample. In order to achieve high spatial resolution, one has to focus the beam to as small a spot as possible. This tightly focused laser beam will introduce some very complicated field distributions relevant to SH generation, e.g. features not seen in normal planewave excitation.

We start with Si(100). Si(100) is a material with cubic symmetry. The inversion symmetry of Si(100) dictates that there is no SHG allowed from Si(100) under the dipole approximation. The only possible bulk source for SHG could come from higher-order contributions, i.e. the non-local electric quadrupole and magnetic dipole contributions. As we showed in equation (2.6), the second-order polarization at this case is:

$$P_i^{\omega} = \Gamma_{ijkl} E_j \nabla_k E_l. \tag{2.13}$$

Here (ijkl) is the Cartesian coordinates. The non-zero elements for Γ are listed in Table 2.1 [56]. All elements not listed are zero. ζ is a phenomenological constant

reflecting the anisotropic contributions, (see equation (2.7)), θ is a constant angle offset between lab coordinate axis and the crystal coordinate axis [56].

For an ideally normal incidence light beam, ∇_k will have zero values except for k=z direction, where $\hat{z}$ is normal to the crystal surface and xy decides the crystal surface plane. Considering the fact that for normal incidence beam propagating along $\hat{z}$ direction, there is no electric field component along the $\hat{z}$ direction, it is not hard to show from equation (2.13) and Table 2.1 that no SHG is expected from Si(100) in normal incidence. i.e., even the electric quadrupole and magnetic dipole contributions are disallowed in normal incidence.

This is not what we have observed. Our observations indicate the complexity of dealing with SHG in the nonlinear microscope system. In Fig. 2.5, we show our SHG observation from Si(100) along with Si(111) data [51]. Here, we rotate the Si crystal about the axis perpendicular to its surface and ϕ is the rotation angle relative to one arbitrarily chosen direction on the surface plane. It is very clear that for Si(100) non-zero SH radiation can be observed by nonlinear microscope system.

The discrepancy between theory and experiment can be explained considering many factors. First, as Angerer [51] pointed out, SHG microscopy requires a Gaussian wave description instead of plane wave description. The electric field of a Gaussian beam in the focal plane (z=0) takes the form:

$$\mathbf{E}(x, y, z = 0) = \hat{x} E e^{-\frac{x^2+y^2}{d^2}}, \tag{2.14}$$

where d is the spot size or beam waist of the focused beam. The transverse profile of the Gaussian wave varies appreciably in the focal plane of a tight focused beam which introduces large field gradient in the sample and this Gaussian wave induces a nonlinear polarization with components parallel to the silicon surface [51]. The induced nonlinear polarization can radiate SH field into the vacuum that can be detected by our experimental setup.

Secondly, a tightly focused Gaussian beam will have a longitudinal field in the focal plane as pointed out by Carter [58, 59]. The electric field at the focal plane takes the form:

$$\mathbf{E}(x, y, z = 0) = \hat{x}Ee^{-\frac{x^2+y^2}{d^2}} - i\hat{z}\frac{x}{kd^2}Ee^{-\frac{x^2+y^2}{d^2}}. \tag{2.15}$$

This longitudinal field will again induced anomalous polarization by coupling with appropriate non-zero Γ_{ijkl} elements [51]. In particular, this anomalous behavior of the polarization of a highly focused beam could dominate nonlocal effects for samples with large non-linear susceptibilities that have components perpendicular to a surface. An example of such a sample is a film of rod-like nonlinear molecules that lie nearly perpendicular to a substrate.

Therefore, it is a daunting theoretical challenge to fit the experimental data from first principles in a rigorous way. Besides the above-mentioned factors, one still requires a thorough knowledge of beam characteristics near the focal plane, this includes beam profile, beam polarization status and light beam geometry, and the possible

change of nonlinear susceptibilities caused by these factors. All these present a huge complexity to the problem. In this thesis, instead of attacking the nonlinear microscope problem from a theoretical point of view, we try to present our experimental measurements and point out what are the most interesting observations without getting lost in mountains of mathematics. Whenever appropriate, we will try to suggest the possible mechanisms responsible for our observations.

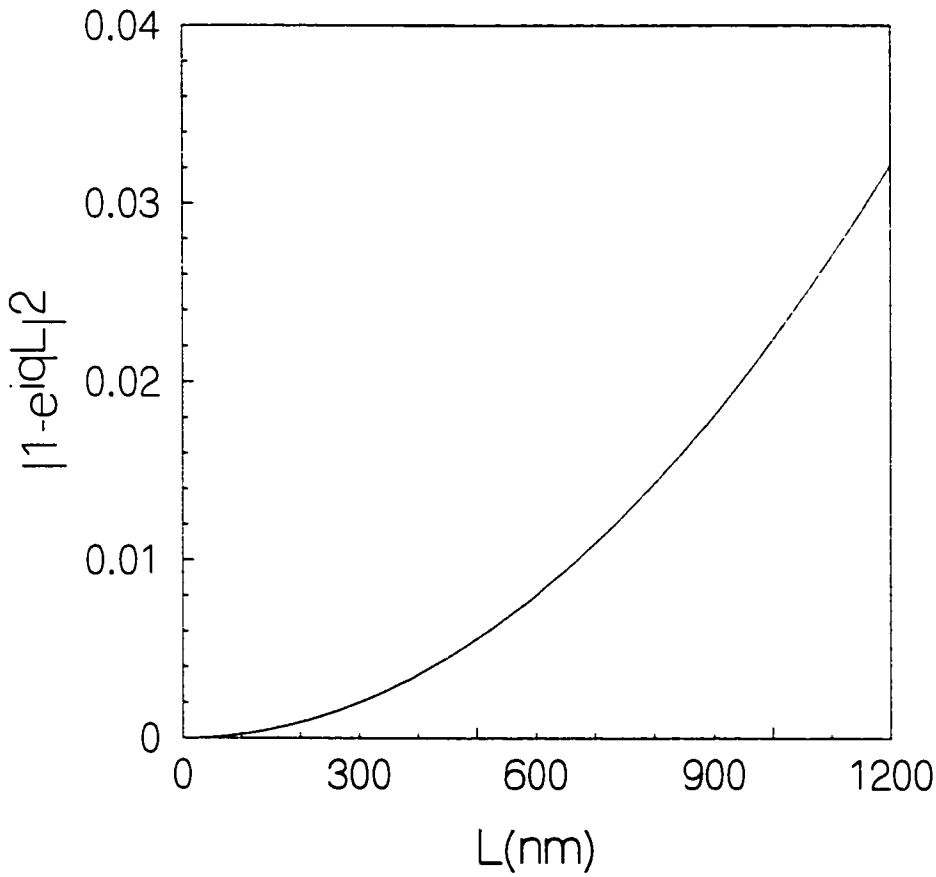

Figure 2.4: $|1 - e^{iqL}|^2$ versus L. It shows that SH radiation is not zero when particle size is comparable with the wavelength while SH radiation rapidly approach to zero when particle size decreases.

Table 2.1: Non-zero Elements of Γ_{ijkl} For Si(100)

Elements	Values
Γ_{1121}	$-\frac{1}{4}\zeta sin(4\theta)$
Γ_{2222}	$\frac{1}{4}\zeta(3 + cos(4\theta))$
Γ_{1222}	$\frac{1}{4}\zeta sin(4\theta)$
Γ_{1122}	$\frac{1}{4}\zeta(1 - cos(4\theta))$

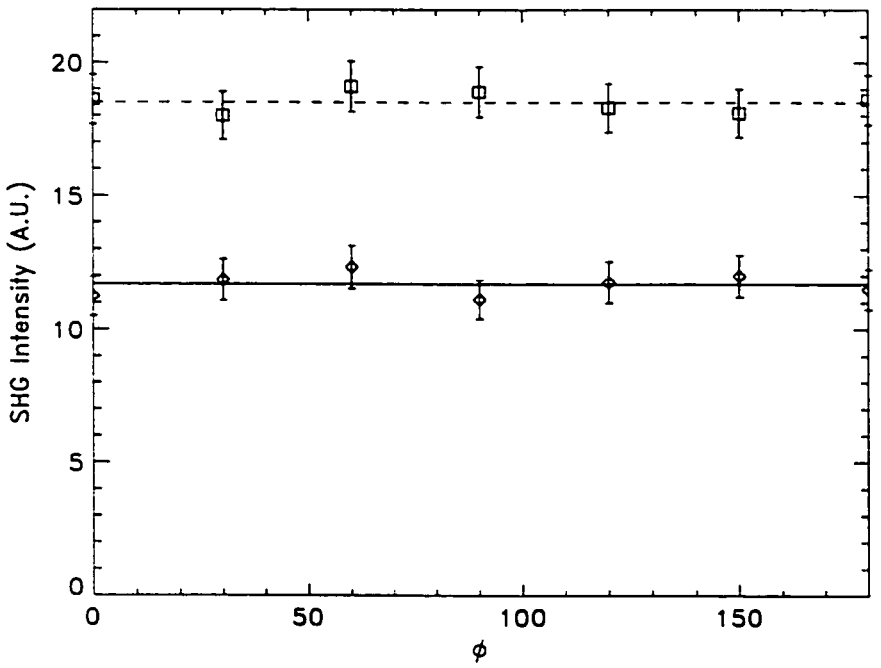

Figure 2.5: SHG rotational symmetry of Si(100) and Si(111) measured by the non-linear optical microscope. ◇ is the experimental data from Si(100) and □ is the experimental data from Si(111). The lines are isotropic fitting.

Chapter 3

Angle-Resolved SHG Scattering From Colloidal Suspension: Experimental

In this chapter, we describe the experimental setup for our angle-resolved SHG scattering from colloidal suspensions. We will discuss general issues regarding the experiment including the setup, the laser source, the detection system and characterization of some key quantities.

3.1 Experimental Setup

Fig. 3.1 displays a schematic view of the experimental setup we use for the SHG light scattering. The experiments were performed using a 76Mhz mode-locked pulsed Ti:Al_2O_3 laser pumped by Ar Ion laser. Details about the Ti:Al_2O_3 laser will be given in section 3.2. Briefly, the Ti:Al_2O_3 was set to produce a train of ultrashort pulses of duration $\sim$ 100fs, at the wavelength of 840nm. We set λ=840nm because at this wavelength, our dye sample, Malachite Green (MG), has big nonlinear SHG response, and a small two-photon fluorescence response. We will discuss the sample

in Chapter 4. The typical peak pulse power for this laser output is $\sim$ 50KW, which is good for nonlinear optical experiment. The output of the Ti:Al_2O_3 laser is p-polarized (parallel to the optical table and in the plane of incidence).

We direct the fundamental beam to pass through a long pass filter before focusing into the sample. The long pass filter allows only the 840nm fundamental beam to transmit while blocking the residual 2ω light in the source (i.e., block the 420nm blue light). This insures we have a pure 840nm fundamental excitation beam, and all the SHG signal we pick up later on the detector results from the sample. If we choose to use s-polarized fundamental beam, then we put a prism-pair into the beampath to effectively convert the light polarization from p-polarized to s-polarized. The prism pair is shown in Fig. 3.2. The input beam passes through one polarizer before being sent to a lens to be focused into the sample. The lens we use to focus the beam is 100 mm in focal length. The beam waist at the sample is $\sim 40\mu m$ in diameter. The sample cell sits right at the focal point and is also situated at the center of goniometer. The sample cell is cylindrical glass tube with inner and outer diameter of 3mm and 5mm respectively. Because of the circular shape of the sample cell, part of the input energy will be reflected back to the air. It is therefore very important when aligning the input beam to pass it through the sample cell. A misaligned beam will usually exhibit a distorted beam profile and significantly less beam intensity, and it is therefore not that hard to correct the problem.

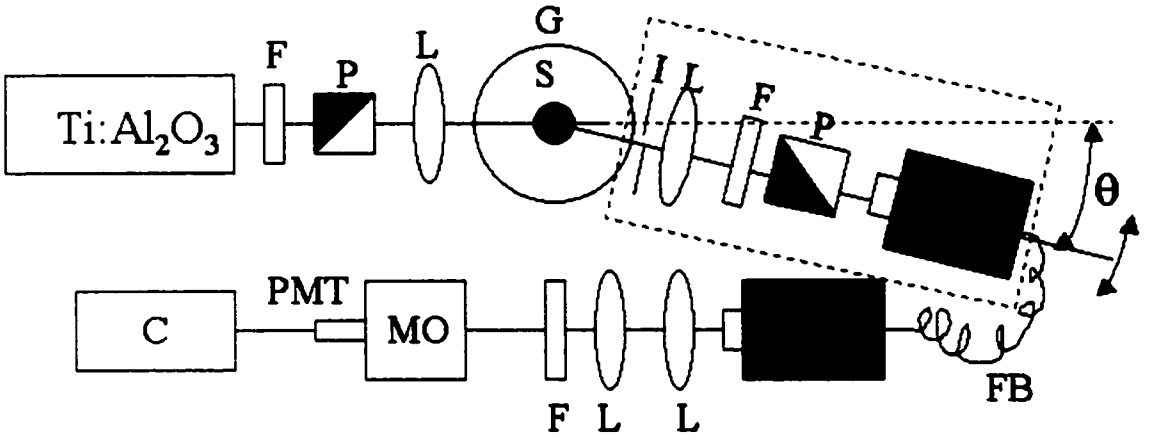

Figure 3.1: Schematic of experimental setup for angle-resolved SHG scattering from colloid suspension. Notation: F:filter, P:polarizer, L:lens, G:Goniometer, S:sample, I:iris, FB:fiber, MO:Monochromator, PMT:Photomultiplier, C:photon counter. The filter before sample eliminates 2ω light and pass ω light, while the filters after sample can pass only 2ω signal. S-direction is perpendicular to the paper, p-direction is parallel to the paper.

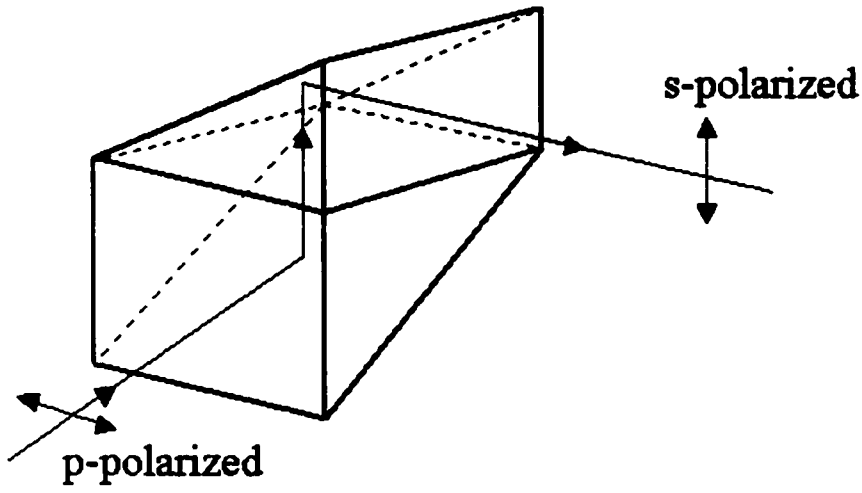

Figure 3.2: Prism pair. Showing the conversion from p-polarized light to s-polarized light.

Scattered signal at 2ω was recollimated using same focal length lens, polarization-selected and then coupled into an optical fiber. The components inside the dashed outlined box are all mounted on one single rigid arm, which at the same time is fixed to the rotating plate on the goniometer. The rotating plate of goniometer can be rotated about the axis through the sample center in both clockwise and counter-clockwise directions and is perpendicular to the scattering plane. This configuration makes it possible for us to rotate the whole detection arm when doing the angular scan without destroying the optical alignment. This is the most important and unique feature of our apparatus: angle resolution. The low N.A. (i.e. 0.16) detection fiber together with the $\sim$ 1mm iris determined our angular resolution of $\sim 1^0$. The fiber collimator, which we use to couple the light into the fiber, is model F230SMA-A from Thorlabs Inc. The AR coating of $350nm \sim 600nm$ for the collimator makes it ideal for our SHG signal collection. The optical fiber itself is silica/silica multimode fiber with glass-cladding. The glass-cladding allows high power, better alignment and it has better UV transmission compared to polymer-cladding. Finally, the low N.A. (i.e. 0.16) of the optical fiber also makes sure the low beam divergence and uniform spot size. The typical energy coupling efficiency for this fiber optics system is about 75%.

The output from fiber was recollimated before being coupled into a monochromator and collected by photomultiplier tube (PMT). A lock-in photon counter (SR400) was used for signal averaging. We will discuss the detection system later in section

3.4. Note that after the laser beam passes through the sample, we use two BG39 filters to spectrally filter the unwanted fundamental 840nm beam and pass only the 420nm SHG signal. The transmission spectrum of a typical BG39 filter is shown in Fig. 3.3. It has about 65% transmission efficiency for our SHG signal, while it completely blocks the fundamental light. Two BG39 filters can attenuate the fundamental beam by 12 orders of magnitude. With the additional filtering by monochromator and PMT, our detection system effectively blocks the fundamental beam by an order of magnitude of more than 10^{17} and is optimized to detect the SHG signal. Finally, the whole experimental setup is well shielded from the room scattering light source by completely covering them with black cloth. All the measurements are performed in dark environment. The background noise in our system is less than 1 count per second.

3.2 Ti:Al_2O_3 Laser

The fundamental light generating source in our experiments is a Coherent Ti:Al_2O_3 laser model Mira 900B. A Coherent Innova 310 Ar ion laser pumps the Ti:Al_2O_3 in a multiline configuration with 8W. A schematic of the laser is displayed in Fig .3.4. Table 3.1 displays some of the key parameters about this Ti:Al_2O_3 laser. The gain medium is a piece of Ti:Al_2O_3 crystal which sits in the lasing cavity. There are two different cavities in this laser: an auxiliary cavity and a main cavity. The

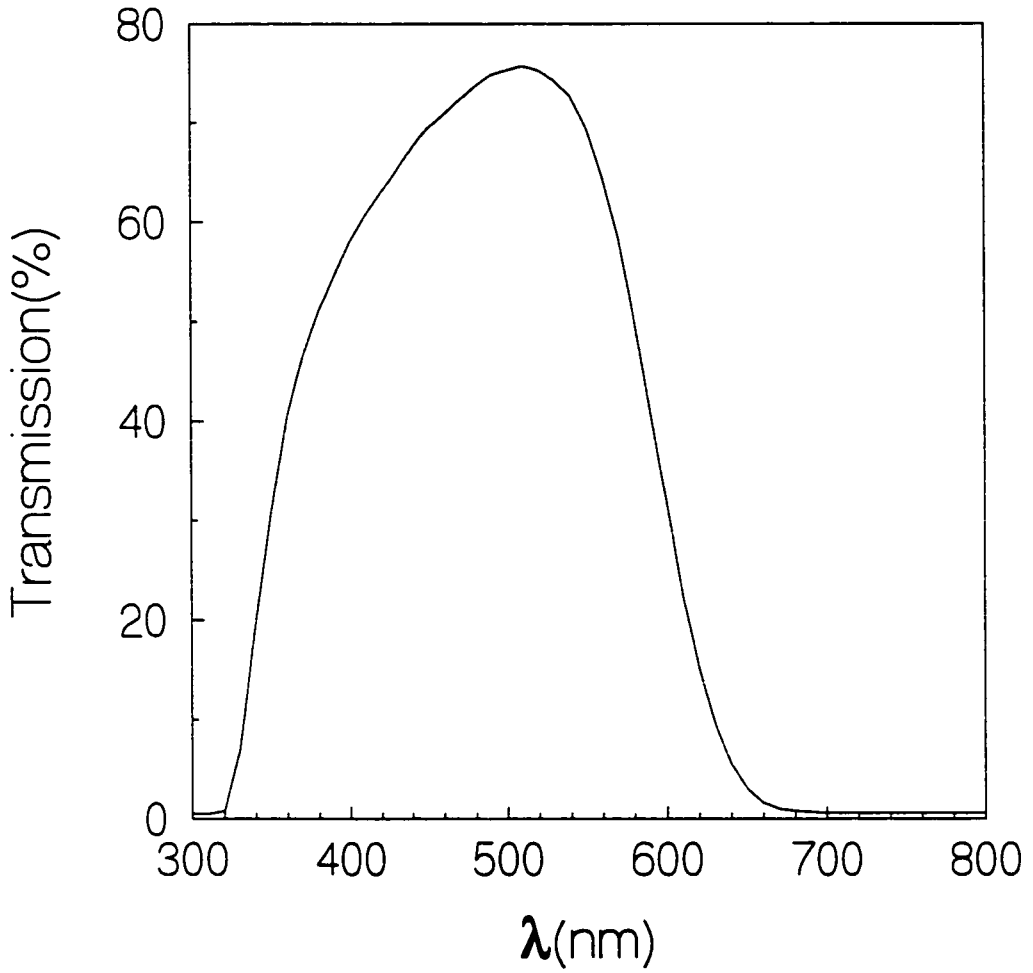

Figure 3.3: Transmission spectrum of BG39 filter. It shows that BG39 is a good low pass filter while blocking 840nm fundamental beam.

Table 3.1: Characteristics of Ti:Al_2O_3 Laser

characteristic	value
pump source	8W Ar ion laser
wavelength range	700-1000 nm
CW power	1.5 W at 800 nm
mode-locked power	800 mW at 800 nm
typical pulse width	80-150 fs
pulse peak power	50 kW
repetition rate	76 MHz
spatial mode	TEM_{00}
polarization	horizontal
bandwidth of modelocked pulse	10 meV

auxiliary cavity consists of M1 (output coupler) on one end of the cavity and M9 on the other end of the cavity with BP1 moving out of the path. (dashed line in Fig. 3.4). This auxiliary cavity is solely for the purpose in the initial laser alignment and is very useful troubleshooting the laser alignment at the very beginning stage. After auxiliary cavity alignment is done, BP1 is inserted into the beam path and the lasing shifted to main cavity which consists of M1 on one end and M7 on the other end. All the experiments are performed for Ti:Al_2O_3 laser to operate at the main cavity. The

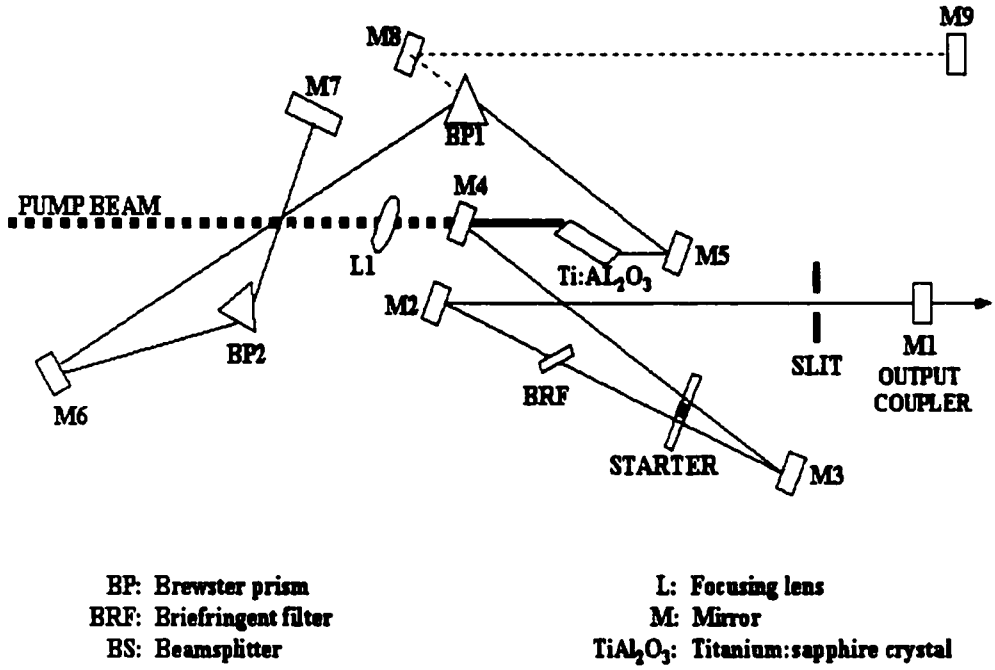

Figure 3.4: Schematic of Ti:Al_2O_3 laser. The dashed line part (M8 and M9) is auxiliary cavity.

most distinct features about this Ti:Al_2O_3 laser are its tunability and generation of ultrashort pulses. The tunability of Ti:Al_2O_3 is achieved by the coupling of the active medium (Ti ion) to the host crystal (Al_2O_3) and by the setting of birefringent filter (BRF) to select the desired wavelength. Moreover, there are 3 sets of optics (short wavelength, medium wavelength, and long wavelength), each of which is optimized for some specific spectrum range. In our experiments in this thesis, we use medium optics and choose the wavelength of 840nm.

The generation of ultrashort pulse is very critical to nonlinear optical experiments. In Ti:Al_2O_3 laser, the achievement of ultrafast, high peak power pulses is through a passive modelocking process called Kerr-lens modelocking. The idea is that the initial CW (continuous wave) laser light in the laser cavity consists of a spectrum of discrete frequencies called modes. These discrete frequencies are decided by the cavity length with the requirement that each lasing wavelength must satisfy the condition that precisely an integral number of half wavelengths must "fit" between the mirrors. When laser is operating in cw mode, the phases between the cavity modes are random. If by some means we can lock the phase relationships between different modes, then all these modes will add coherently to form temporal interference, much like the multi-slit spatial interference. The result will be sharp peak in the temporal space, i.e., ultrafast pulses.

In Ti:Al_2O_3 system, an electric mechanical device called starter galvo (shown in

Fig. 3.4) is inserted in the cavity. After triggered, the starter modulates the cavity length and thus modulates the cavity modes at a designed speed. The modulation speed is carefully chosen such that the modulation frequency is equal to the cavity mode frequency spacing and the addition of the modulated modes will result in each mode strongly coupled with each other, thus achieving the effect of phase locking. The mathematics behind this process is excellently detailed in the book by P.W.Milonni and J.H. Eberly [60]. Once a modelocked pulse is created, it will generate instantaneous high power intensity in the cavity. Because the laser crystal itself is also a Kerr medium, i.e. the active medium has an intensity dependent index of refraction. This high power intensity will create a gradient index lens, the Kerr lens, where the center of the beam has a higher index of refraction and the edge will have less index of refraction. The Kerr lens will therefore focus and narrow the pulsed beam. On the other hand, the CW beam doesn't have enough high power intensity to create the Kerr lens and thus CW beam will have larger beam profile. By putting one adjustable slit before the output coupler and adjust the slit width (Fig. 3.5) one can make sure that the narrowed pulsed beam can pass unattenuatedly through the slit while the CW beam will incur loss at the slit. The result is that the pulse will get amplified at the expense of the CW beam and finally being coupled out of the laser cavity. This is the whole basis for the creation of mode-locked ultrashort pulse. Once the laser is mode-locked, one can optimize the performance by monitoring the laser signal with

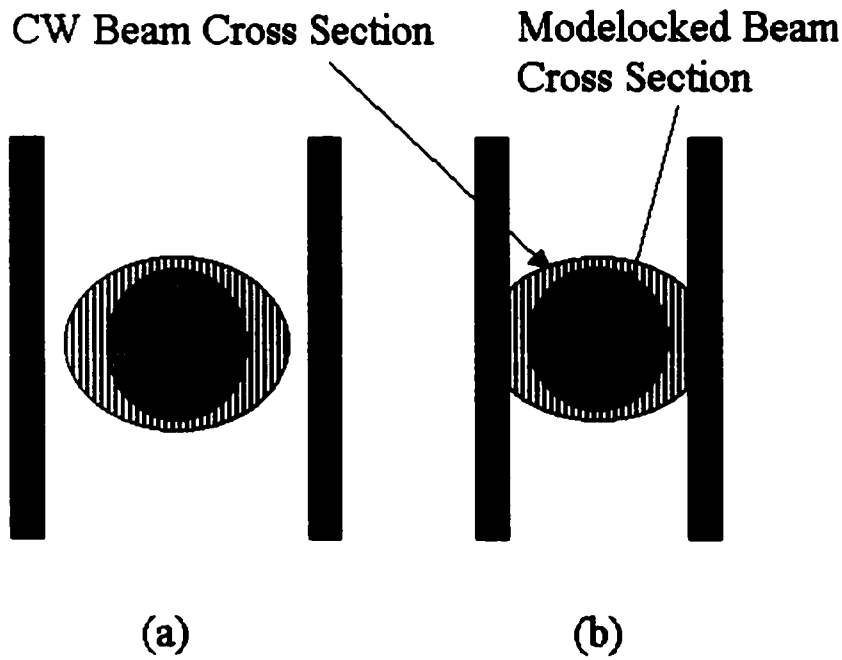

Figure 3.5: Slit size and beam cross section. (a)Slit full-open. No loss for either modelocking or CW. Stable mode-locking can't be achieved. (b)Slit half-open. The CW beam is partially cutoff while modelocked beam can go through. Stable mode-locking can be achieved.

a fast silicon photodiode terminated by a 50Ω resistor on an oscilloscope.

3.2.1 Pulse Width

In theory, the shortest pulse duration is approximately the reciprocal of the gain linewidth. However, in a real laser system, the pulse width is complicated by many factors. An ultrashort pulse is actually formed by the sum of a distribution of wavelengths on either side of the center wavelength. The width of the distribution is inversely proportional to the length of the pulse. Moreover, in order to produce a short pulse of light from the distribution, the timing or phase between each component wavelength must be precisely correct. Otherwise the pulse will not be as short as it could be.

When one ultrashort pulse passes through optics such as glass, its different frequency components will experience different group velocity dispersions. i.e. $\frac{d^2n(\lambda)}{d\lambda^2}$, which governs the rate at which the frequency components of a wave packet change their relative phases, will be different for different frequency components. The group velocity dispersion (GVD) will cause temporal reshaping of wave packets. This can be a broadening or a shortening shape change depending upon the initial conditions (chirp) of the wave packet spectrum. Fig. 3.6 shows example of positive chirp and negative chirp. For glass material, the pulse is positively chirped. i.e. its instantaneous frequency increases from leading edge to trailing edge. Its blue spectral

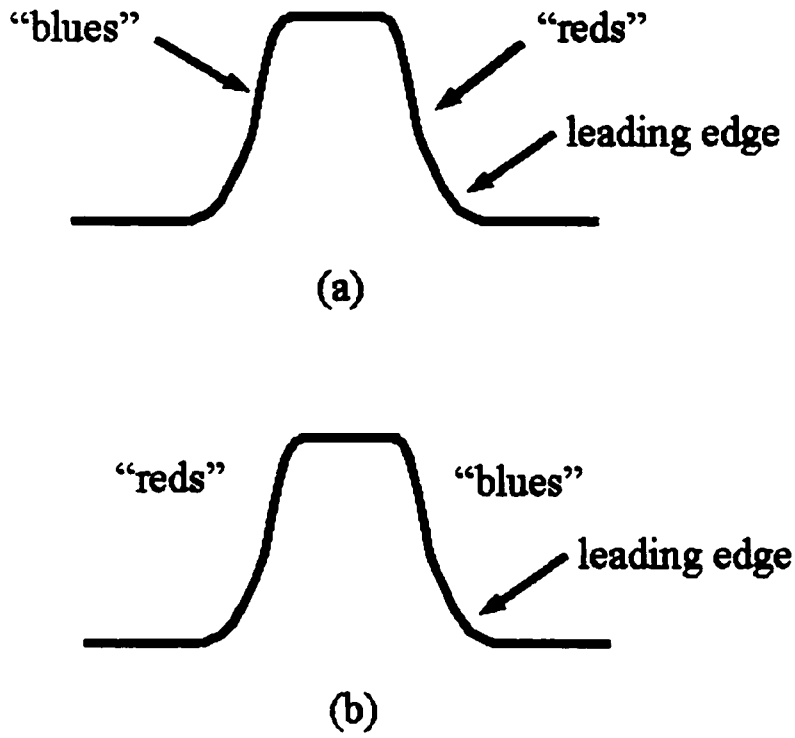

Figure 3.6: Chirp in a pulse. (a)Positive chirp. Red frequency components lead the blue components. This results from positive group velocity dispersion (b)Negative chirp. Blue frequency components lead the red components. This results from negative group velocity dispersion

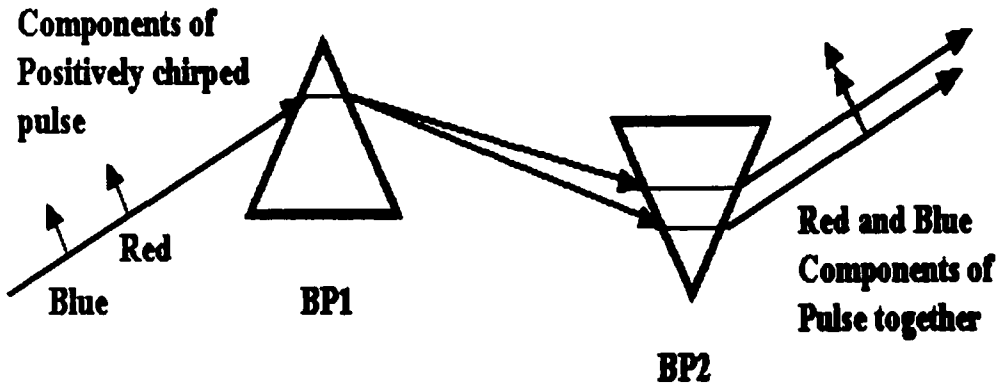

Figure 3.7: GVD compensation. The positively chirped pulse is compensated when passing through two Brewster prisms as-positioned.

components will be retarded with respect to the red, creating a systematic variation of phase with respect to wavelength. In addition to the group velocity dispersion, pulses in ultrafast lasers are also affected by self-phase modulation (SPM). Due to the optical Kerr effect, intense light pulses propagating through dense media create a local index of refraction that is dependent on the light field intensity. Therefore, the leading and trailing edges of the pulse will cause less change in the index than the center where the intensity is highest. Frequency components propagating through the material are thus phase shifted differently depending upon when they occur in

the pulse. These frequency components are inherently chirped and can broaden the pulse unless the chirp is compensated. It is known that for normal optical material such as glass, the chirp which results from SPM has the same sign of the chirp as that introduced by GVD.

Because there are many dispersive optical elements within the laser cavity, and because the pulse will bounce back and forth many times within the cavity, the cumulative effect of even a very small chirp per round trip would create significant broadening and pulse substructure. Therefore, some method must be employed to allow the slow frequencies or wavelengths to catch up with the faster ones. Ti:Al_2O_3 system uses a pair of Brewster prisms to compensate this (BP1 and BP2 in Fig. 3.4). These two prisms are separated by a distance and oriented in a specific way with respect to each other. The net GVD of this prism pair is negative as shown in Fig. 3.7.

The advantage of the prism pairs is that it is very easy to adjust the GVD compensation by simply changing the amount of prism glass within the cavity. One achieves this by just translating the prism into or out of the beam path more or less. Moreover, experience shows that this GVD has big impact on the stable operation of laser mode-locking. Therefore, adjustment of prism pairs is sometimes very useful for trouble-shooting the mode-locking problem.

3.3 Autocorrelation

Ultrashort pulse is essential in performing nonlinear optical experiment. To quantitatively have idea of the peak power intensity, upon which SHG is quadratically dependent, is also very critical. Autocorrelation is the technique we use to measure the width for our ultrashort pulse. We built the autocorrelation apparatus as shown in Fig. 3.8. The autocorrelator is essentially a nonlinear optical interferometer, it detects the autocorrelation function [61, 62, 63, 64].

$$S(t) = \int E_f(t')E_v(t' - A(t))dt'. \tag{3.1}$$

Here E(t) is the electric field envelop function for the pulse. Subscripts "f" and "v" indicate the copies of pulse at the "fixed" and "variable" arms respectively (explained below), and A(t) is the time difference introduced by the autocorrelator between the fixed and the variable copies of the pulse.

The Ti:Al_2O_3 ultrashort pulse enters the autocorrelator and is split by a 50/50 beam splitter. One copy of the pulse travel along the "fixed" arm which has two high reflective mirrors mounted on a speaker which is vibrating at 60Hz. Another copy of the pulse travel along the "variable" arm on which two mirrors are mounted on a translation stage and can move the beam at directions shown in the Fig. 3.8. The two copies of pulse meet at the lens but separated at a distance ~1cm. The lens has a focal length of 100mm and it focuses the two beams to a point inside a nonlinear crystal. We used a 0.4mm thick KDP crystal cut for type I phase matching. i.e. the

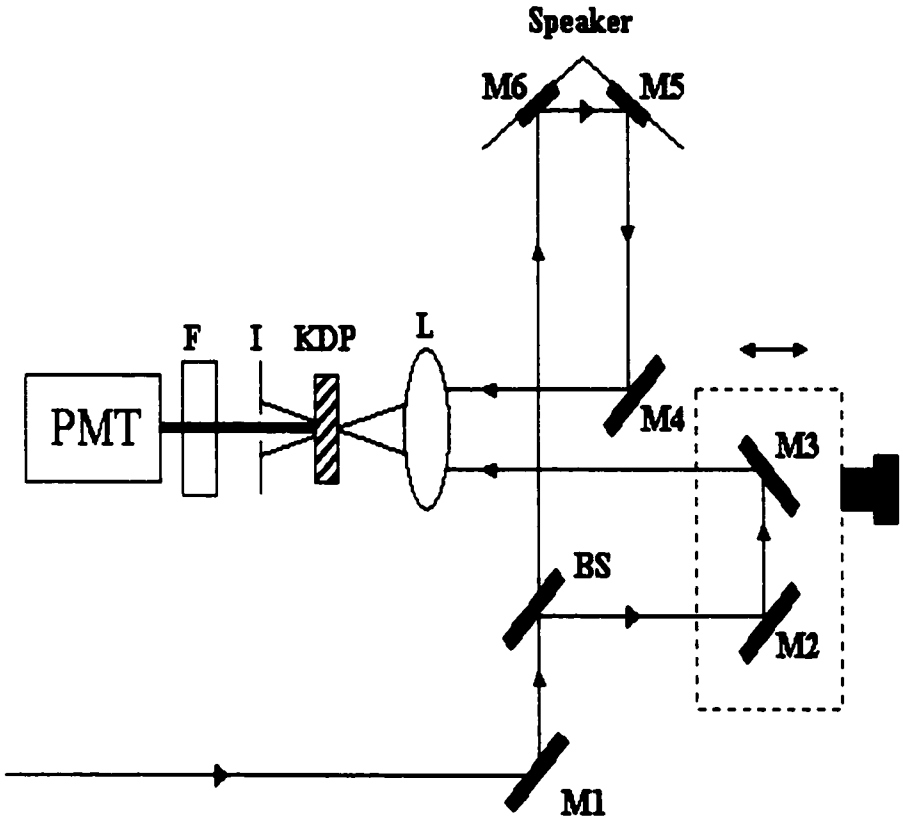

Figure 3.8: Schematic of autocorrelator. Notations: M:mirror, BS:beam splitter, L:lens, KDP:nonlinear crystal, I:iris, F:filter, PMT:photomultiplier. The thick line represents autocorrelated SHG signal.

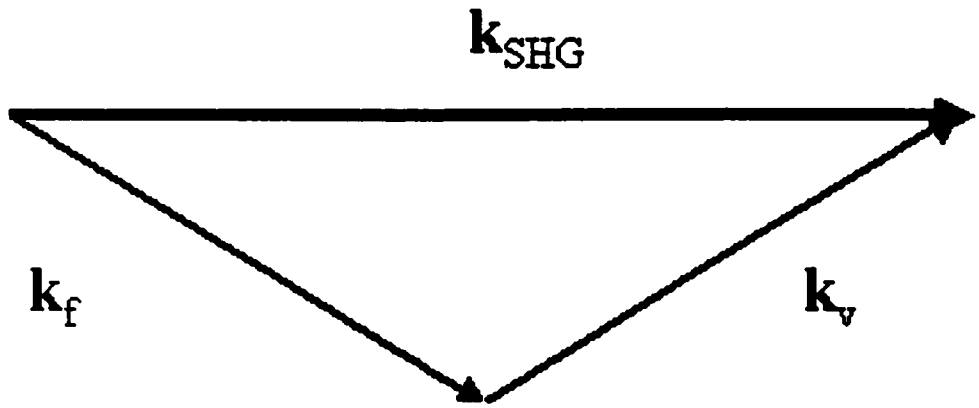

Figure 3.9: Diagram showing type-I phase matching. The direction of $\mathbf{k}_{SHG}$ is different from $\mathbf{k}_f$ and $\mathbf{k}_v$.

phase matching condition requires that

$$\mathbf{k}_f + \mathbf{k}_v = \mathbf{k}_{SHG}. \tag{3.2}$$

As shown in Fig. 3.9, this non-collinear phase matching separated the fundamental beams from the generated SHG, it is therefore well suited to detect the SHG with considerably less background noise. After careful alignment with both copies of pulse overlaying both spatially and temporally, we can observe the autocorrelated signal on an oscilloscope. We use following methods to decide the pulse width. We first

measure the width of the autocorrelated function, say $\Delta t_{initial}$, then the translation stage with the reflecting mirrors is moved $\sim 50\mu m$. This changes the round trip distance for the variable arm by $100\mu m$, corresponding to 300fs. (speed of light has a value of $0.3\mu m/fs$). The corresponding autocorrelation function envelop on the oscilloscope will shift by some amount of ms, denoted by Δt_{shift}, then the width of the Ti:Al_2O_3 pulse is obtained:

$$\Delta t_{Ti:Al_2O_3} = \delta_c \frac{2L\Delta t_{initial}}{c\Delta t_{shift}}. \tag{3.3}$$

Here L is the distance translation stage moved, $\delta_c = 0.648$ is a factor that relates the autocorrelation envelop function width of S(t) to the true pulse width of E(t). For Mira pulses, the S(t) trace is described by a $sech^2$ and the appropriate conversion factor is 0.648 [65].

Our measurements of Ti:Al_2O_3 laser pulse width at λ=840nm is $\sim 106fs$.

3.4 Signal Detection

In this section we discuss the detection part of the experiment. We design our detection system such that they will be optimized for our SHG collection while filtering out the fundamental light. Also, the ability to detect small signal while maintaining decent signal to noise ratio is also our concern.

The monochromator we use is Thermo Vision MonoSpec 18. The grating has a groove of 1200 g/mm blazed at 300nm. We use 1mm slit at both the entrance

and exit window to block scattering background noise while maintain decent signal throughput. Before the entrance window, there is always a BG39 filter to cut off the fundamental beam. We use a cooled Hamamatsu side-on PMT model R4220P to collect the SHG signal exiting from the Monochromator. This PMT has a bialkali photocathode with a gain of 1.2×10^7 at a bias voltage of 1150V, a rise time of 2.2ns, and a quantum efficiency of $\sim$ 20% at a wavelength 420nm (see Fig. 3.10). The PMT is cooled to -20^0C by a Products For Research liquid heat exchanged, thermoelectric cooled housing model TE177RF. This configuration greatly reduce the thermal noise in the detection system. We also cover the whole experimental setup by a black cloth to well shield the setup from room scattering light. Our detection system thus built has less than 1 count/second noise.

One important characteristic about PMT is the pulse height distribution. This characteristic is critical to the discriminator level setting on the photoncounter. Usually, the PMT output exhibits fluctuations in the pulse height and one has to set the discriminator level such that we discard most of the noise while pick up as many as signal photons as possible. We measured the pulse height distribution curve for our model PMT and it is shown in Fig. 3.11. From that curve we can decide the correct level to set the discriminator level (shown as vertical line in the Figure) is 30mV. The photoncounter we use is Stanford Research System Model SR400 gated photon counter. The gated photon counter is an integrated photon counting system

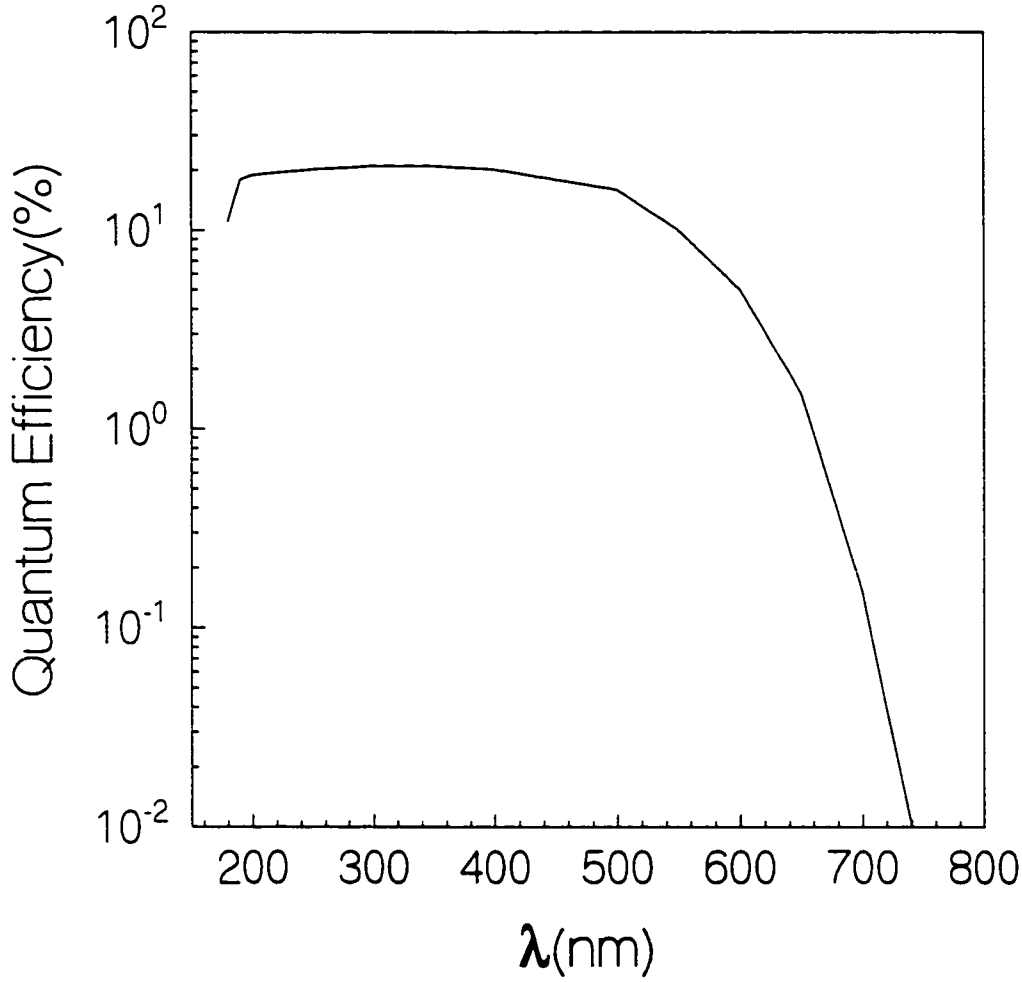

Figure 3.10: Quantum Efficiency for Hamamatsu PMT model R4220P. The efficiency at $\lambda = 420nm$ is $\sim 20\%$

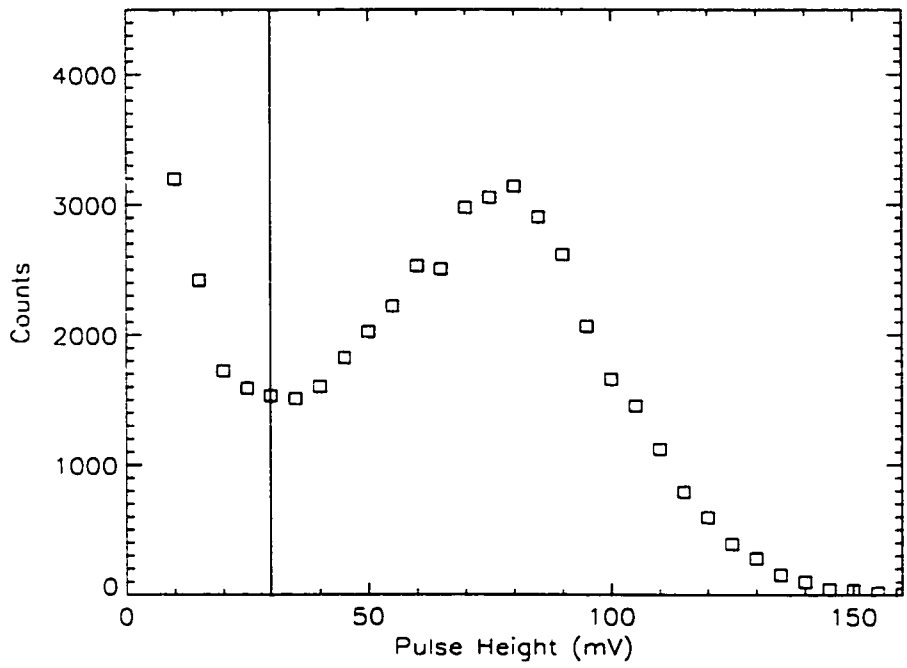

Figure 3.11: Pulse height distribution. The correct discriminator level is at 30mV shown as the vertical line.

that consists of amplifiers, discriminators, gate generators, and counters. It has dual channel photon counter and a variety of counting modes to match different needs. In the SHG scattering from colloid suspension experiment, we use single channel photon counting. In Chapter 6, we will discuss one technique to use dual channel photon counting.

Chapter 4

Angle-resolved SHG Scattering From Colloidal Suspension: Sample

In this chapter we discuss the samples we used in our angle-resolved SHG scattering experiments. We discuss sample preparation, sample characteristics, and some characterizations relevant to our SHG scattering experiment.

4.1 Malachite Green

Malachite Green (MG) is a water-soluble triphenylmethane dye [66]. Our MG sample was purchased from Sigma Chemical Company [67]. The basic specifications of Malachite Green are tabulated in Table 4.1. The molecular structure is shown in Fig. 4.1.

Malachite Green is very easy to dissolve in the water. When in water solution, Malachite Green usually takes on different ionized forms depending upon the solution pH [66, 68]. When solution pH is below ~ 1.5, MG will take the form of MG^{++}. If solution pH value is between 2 and 7, MG will take the MG^{+} form. When the solution pH value is larger than 7, MG will react with hydroxyl ions of the water to

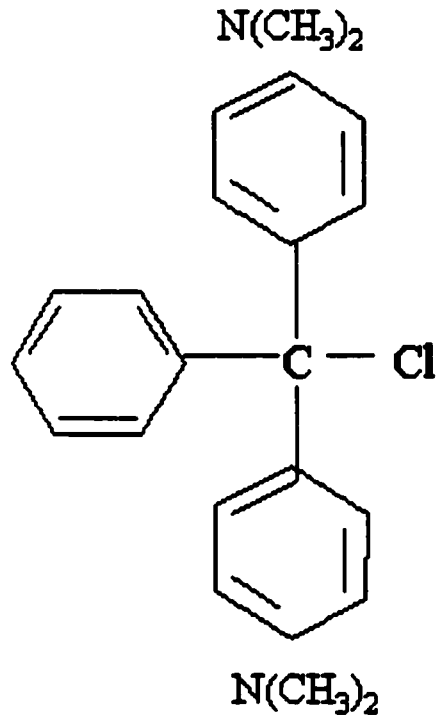

Figure 4.1: Molecular structure of Malachite Green hydrochloride. Three phenyl groups are attached to the central carbon atom. But only two amine groups $N(CH_3)_2$ present.

Table 4.1: Specifications of Malachite Green Dye

item	specifications
Aldrich Catalogue No.	21,302-0
Sigma Product No.	M9636
Molecular Form	$C_{23}H_{26}N_2O{\cdot}HCl$
Formula Weight	382.94
Adsorption peak in water	615 nm
Solubility	H_2O

form color white $MGOH$. In reality, all three ionized forms exist in the solution and one particular form dominates within the specific pH value range.

For Malachite Green to actively react with negative charges such as the negative surface charges on colloidal Polystyrene particles, MG^+ has to be the major form of MG. This MG^+ is also the stable stock solution form. Therefore, in our experiment, we keep the solution pH value at ~5.7. We achieve this by adding appropriate hydrochloric acid (HCl) to control the ionic strength.

4.2 Polystyrene Particle

Our Polystyrene particles were purchased from Bangs Laboratories, Inc. We used 3 different particle sizes. The specifications of the microspheres are summarized in Table

Table 4.2: Specifications of Polystyrene Microparticles

item	D=0.98μm	D=0.70μm	D=0.51μm
Catalog Code	PC03N	PC03N	PC03N
Bangs Lot Number	987	860	2164
Standard Deviation(μm)	0.04	0.04	0.03
Surface Functional Group	COOH/1	COOH/1	COOH/1
Density of Solid Polymer(g/ml)	1.060	1.060	1.060
Parking Area ($\mathring{A}^2$/Surface Group)	63.9	32.0	52.5
number of surface charges ($\times 10^6$/particle)	4.72	4.81	1.56
Inorganic salts	$\sim$ 0.05%	$\sim$ 0.05%	$\sim$ 0.05%

4.2. Note that D is the particle diameter, the surface charge number is calculated based upon the parking area. The inorganic salt concentration is the value that came with the source solution. We usually dilute the solution about 1000 times when we prepare our experimental samples, therefore, in our experimental sample solution, the inorganic salt solution was about 10μM. All source samples have 10% solids content.

All three particles have negative surface charges due to the surface functional group $-COO^-$. These carboxyl groups provide an attractive electrostatic interaction for the positive MG^+. Also, the negative charges provide a hydrophilic surface and provide colloidal stability.

4.3 Sample Preparation

We prepare our samples by mixing Malachite Green and PS particles using Deionized Ultra Filtered (DIUF) water at varying concentrations. To illustrate, we give the process for preparing one sample of PS+MG suspension, with PS particle size of $0.70\mu m$ and density of $6.3 \times 10^8/cm^3$, MG concentration at $7\mu M$.

(1)Prepare 500ml DIUF water, add proper HCl to make the solution pH at about 5.7.

(2)Weigh 22.5mg of Malachite Green source sample, mix them with 50ml water from (1).

(3)Get 0.5ml solution from (2) and mixed it with 50ml water from (1). Now we get MG solution of $\sim 10\mu M$.

(4)Get 7.0ml MG solution of (3) and mixed it with 3.0ml water of (1). Now we get MG solution of $\sim 7\mu M$.

(5)Get $11.3\mu l$ source solution of D=$0.70\mu m$ PS microsphere and mixed it with the 10ml solution of (4). Now We obtain the suspension with PS particle density about $\sim 6.3 \times 10^8$ particles/cm^3.

(6)Double check the solution pH value and adjust if necessary.

The sample made this way looks light green in color and transparent. And it

is found that after 2 or 3 days idle, particles settle at the bottom of sample cell. Therefore, all our measurements are performed with fresh-made sample and they are quite uniform within the time period of our measurements (which is typically about 2 hours).

4.4 Adsorption Isotherm of Malachite Green on Polystyrene Particles

As a popular dye, Malachite Green has been extensively studied in a variety of fields. Mostly, the interest has been focused on the internal conversion mechanism of this dye that involves the twisting of molecular constituents around single or double bonds in the excite state [69, 70, 71]. These studies can provide ultrafast dynamics about the barrierless isomerization of the excited state [72, 73, 74, 75], and these in turn provide insights about the fluorescence quantum yield of these dyes on solvent viscosity [76, 77, 78, 79]. Recently, the SHG technique has been used in studying these processes [80, 81, 82, 83]. In addition, polarization spectroscopy was also used to obtain quantitative values of the nonlinear susceptibility of dye solutions [84, 85].

In our work, we use SHG to study the adsorption isotherm of Malachite Green on Polystyrene particles. As we show in Chapter 2, SHG is unique in studying the surface process. Also, the studies of the MG adsorption isotherm will better serve our goal to study SHG light scattering from *particles*. The adsorption isotherm can serve as one characteristic of our sample.

Table 4.3: Geometrical parameters of lens used in Fig. 4.2

lens	focal length (mm)	diameter (in.)
f_1	100	1
f_2	70	$2\frac{1}{4}$
f_3	200	3
f_4	50	1
f_5	50	1

4.4.1 Experimental Setup for Adsorption Isotherm

Fig. 4.2 is the schematic view of the experimental setup for MG adsorption isotherm measurement. This setup is different from the angle-resolved light scattering setup (Fig. 3.1). We don't use the goniometer here. Moreover, instead of using an optic fiber to collect signal, we use large diameter lens to collect the SHG signal. This configuration increases the signal. Table 4.3 lists the geometry of lens used. In this way, we collect SHG signal over a large solid angle, and obtain a better signal-to-noise ratio. The laser source and detection system are as described previously (Chapter 3).

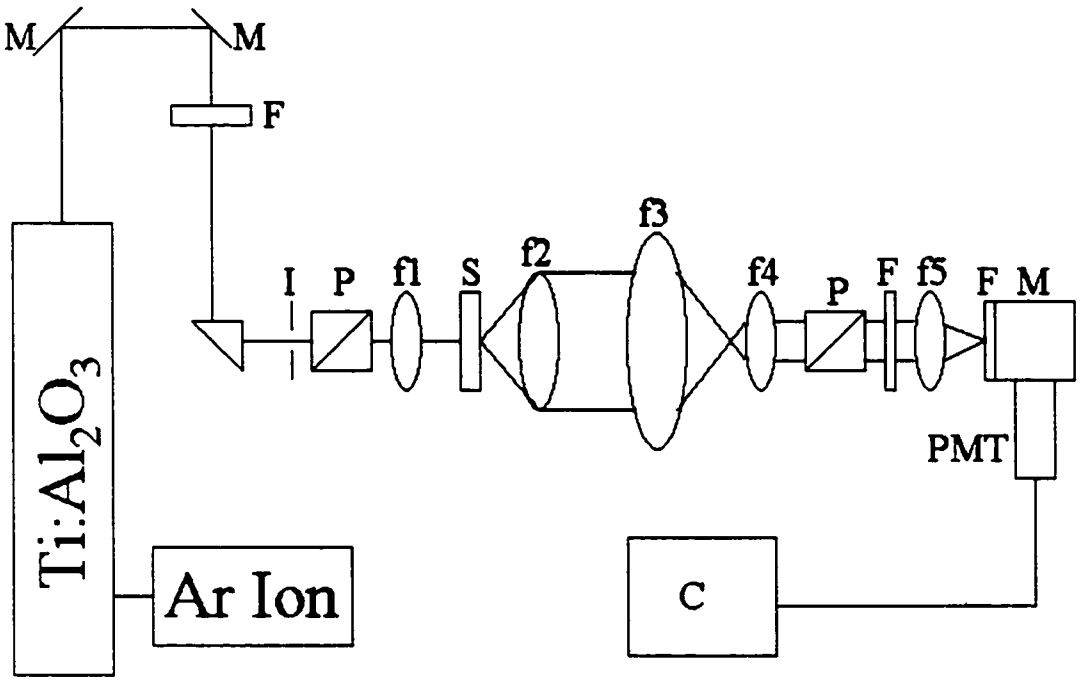

Figure 4.2: Schematic of experimental setup for adsorption isotherm. Notations: M:mirror; F:filter; I:iris; f1-f5:lens; S:sample; P:polarizer; M:monochromator; PMT:photomultiplier; C:photon counter.

4.4.2 Results of Adsorption Isotherms and Discussions

The SHG signal we detect is due to MG molecules adsorbed onto the surface of microspheres as described in Chapter 2, and from MG molecules mainly in bulk solution. The signal from the bulk solution is actually two-photon excited fluorescence (discussed in Chapter 5). This two-photon excited fluorescence signal was found to be about 200 times smaller than the SHG from particle surfaces in the systems we studied. The detected SHG intensity was therefore approximately proportional to square of the coverage of MG molecules on the particle surface, i.e.

$$I_{2\omega_0} = I_0(\frac{N}{N_{max}})^2, \tag{4.1}$$

where I_0 is a constant to be decided by fitting, N_{max} is the maximum number of sites per unit volume and N is the number of adsorbed molecules per unit volume. By measuring the SHG intensity versus the added Malachite Green concentration, we obtain adsorption information about the Malachite Green of the particles, i.e. the adsorption isotherm. We show the adsorption isotherm for MG on three PS particles in Fig. 4.3. We fit the data using the following expression derived from modified Langmuir model (see Appendix A).

$$\frac{N}{N_{max}} = \frac{(C + N_{max} + 55.5/K) - \sqrt{(C + N_{max} + 55.5/K)^2 - 4CN_{max}}}{2N_{max}}. \tag{4.2}$$

The best fits are shown as lines in Fig. 4.3. Here C is the MG concentration in μM, K is the equilibrium constant of the adsorption reaction in unit of $(\mu M)^{-1}$. Our result

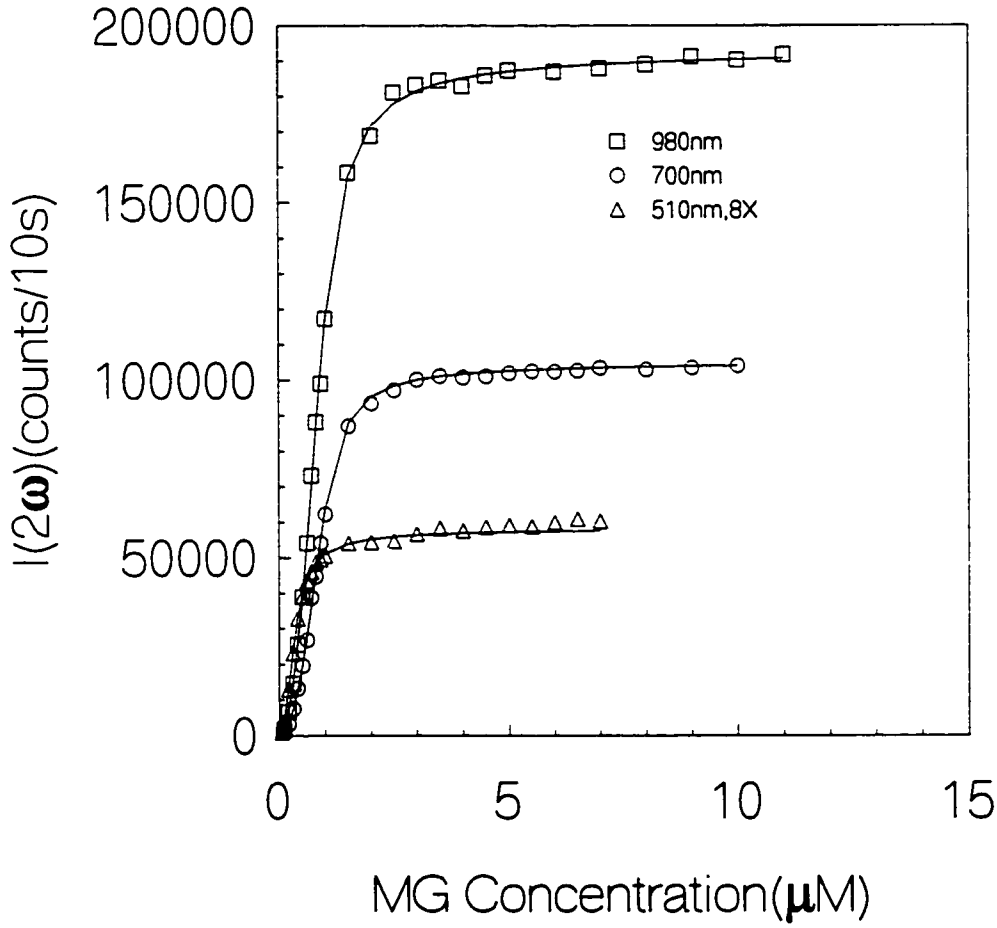

Figure 4.3: Adsorption isotherm for Malachite Green on polystyrene particles. The solid lines are fittings to the modified Langmuir model. The Polystyrene particle concentration is $6.3 \times 10^8/cm^3$.

Table 4.4: Fitting parameters for MG Adsorption Isotherm

diameter(μm)	I_0	$N_{max}(\mu M)$	$K((\mu M)^{-1})$
0.98	193227.39	0.99	851.72
0.70	105261.69	1.06	1123.13
0.51	7297.03	0.35	1214.79

fits pretty well with theory. The fitting parameters for 3 particles are tabulated in Table 4.4.

In the limit where the Malachite Green concentration is very small, it is easy to show that

$$\frac{N}{N_{max}}|_{c\to 0} = \frac{K}{N_{max}K + 55.5}C. \tag{4.3}$$

That is, when Malachite Green concentration is very small, the adsorption of MG on PS particles is linearly proportional to the MG concentration. The observed SHG is therefore quadratically dependent on the solution concentration within this region. Fig. 4.4 shows the observed SHG versus the MG concentration. The solid line is the fit to equation (4.3), a straight line with slope 1.9 on a log-log plot suggests that the MG adsorption on particles is indeed linear when MG concentration is low.

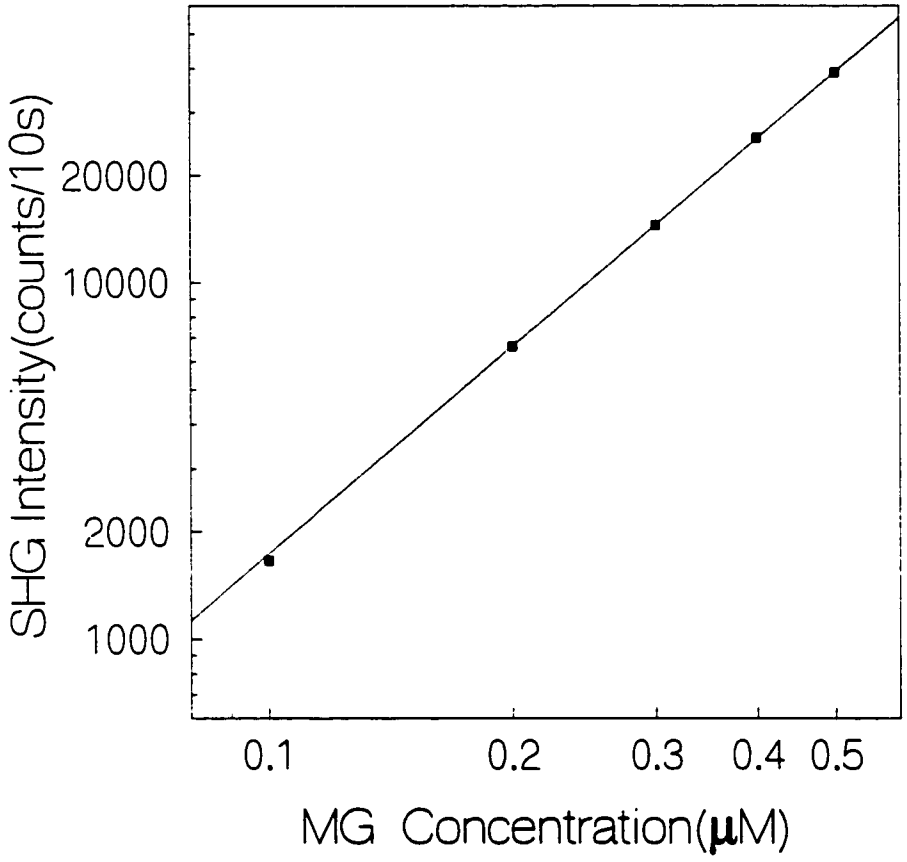

Figure 4.4: SHG intensity versus Malachite Green concentration when MG concentration is low. The solid line is fitting to equation (4.3). The fitting slope is 1.9 suggesting the linear adsorption of MG on PS particles when MG concentration is low. The particle concentration is $6.3 \times 10^8/cm^3$ and of size of $0.98\mu m$ in diameter.

4.5 SHG Dependence on Particle Concentration

We have also characterized our samples by measuring the SHG signal versus the particle concentration in the saturated MG adsorption regime. The result is shown in Fig. 4.5. A slope of 0.91 from fitting suggests that the SHG is linearly dependent upon the particle concentration, i.e. the signal is due to an incoherent sum of each particle. Note also that the average interparticle distance in our samples is $> 15\mu m$, much larger than any coherence length associated with the process. This result will be important when we try to understand the angle-resolved SHG scattering from particles in chapter 5.

4.6 Effect of Electrolyte on SH Generation

We have described the simple SHG theory in Chapter 2. However, for charged surface, there is another possible SHG source, due to static electric field in the bulk solution just outside the charged particle surfaces [86, 87, 35]. We next consider the contributions to SHG from this source.

The SH Generation from solvent molecules polarized by the charged interface is decided by third-order nonlinear polarization

$$P^{(3)}_{2\omega_0}(z) = \chi^{(3)} E_{\omega_0} E_{\omega_0} E_i(z). \tag{4.4}$$

where $\chi^{(3)}$ is the third-order nonlinear susceptibility and E_i is the static field near

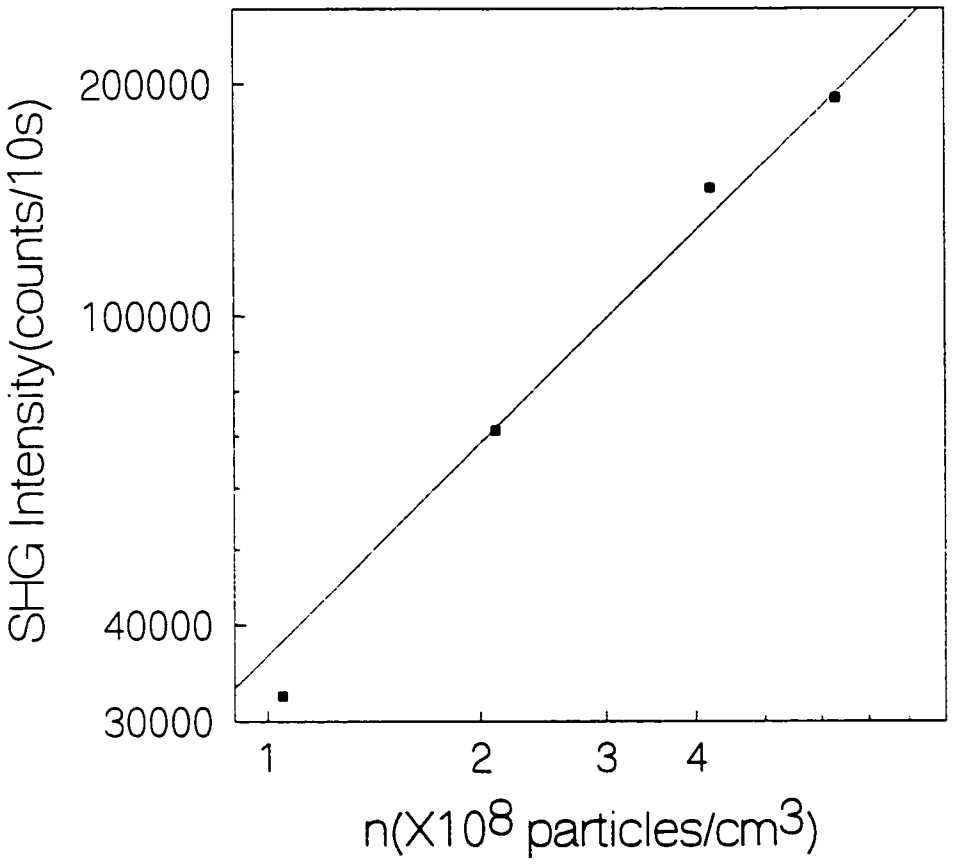

Figure 4.5: SHG Intensity versus particle density. The Malachite Green concentration is $7\mu M$, which is enough to saturate PS particles. The solid line is linear fitting with a slope of 0.91 which suggests that particles contribute to SHG incoherently.

the particle surface. We choose z as the distance from the interface. $\hat{z}$ is normal to interface.

The total induced third-order polarization is obtained by integrating from the interface, z=0, to z=∞ where the electric field decays to zero, i.e.

$$P^{(3)}_{2\omega_0} = \int_0^\infty \chi^{(3)} E_{\omega_0} E_{\omega_0} E_i(z) dz. \tag{4.5}$$

Assuming that the water density doesn't change much, such that $\chi^{(3)}$ can be viewed as z-independent, carrying out the integration we get

$$P^{(3)}_{2\omega_0} = \chi^{(3)} E_{\omega_0} E_{\omega_0} \Phi(0), \tag{4.6}$$

where $\Phi(0)$ is the surface potential. $\Phi(\infty)$ is the potential in the bulk and is set to zero. $\Phi(0)$ can be calculated (Appendix B) and obtained as following

$$\Phi(0) = \frac{2kT}{Ze} sinh^{-1}(\sigma\sqrt{\frac{\pi}{2\epsilon kTC}}), \tag{4.7}$$

where C is the total bulk electrolyte concentration, k is the Boltzmann constant, T is the temperature, Z is the valency of electrolyte ions, σ is the surface charge density and ϵ is the dielectric constant of the bulk solution.

Plugging equation (4.7) into equation (4.6) and also including the contributions from 2nd-order polarization, we write the measured SHG intensity as:

$$I_{SHG} = |\chi^{(2)} E_{\omega_0} E_{\omega_0} + \frac{2kT}{Ze} \chi^{(3)} E_{\omega_0} E_{\omega_0} sinh^{-1}(\sigma\sqrt{\frac{\pi}{2\epsilon kTC}})|^2. \tag{4.8}$$

Using the fact that $sinh^{-1}x = ln(x + \sqrt{x^2+1})$, we can rewrite equation (4.8) as

$$I_{SHG} = |a_1 + a_2 ln(\frac{a_3}{\sqrt{C}} + \sqrt{1 + \frac{a_3^2}{C}}\ )|^2, \tag{4.9}$$

where a_1,a_2,a_3 are fitting parameters and C is the electrolyte concentration. To examine this theory, we prepare two different samples. One is the pure PS microparticles suspension of D=0.98μm with a density of $6.3 \times 10^8/cm^3$, another one is the PS+MG suspension with same PS as first sample but also with MG concentration of $7\mu M$. We add the electrolyte KCl into these two samples to make a range of solutions with salt concentrations from 0.01M to 0.5M. We measure the SHG response. The results are shown in Fig. 4.6 and Fig. 4.7. The solid line in Fig. 4.6 is the fitting using equation (4.9). It is clear that for the PS only suspension, the electrolyte ions induce a third-order polarization and the measured SHG does indeed follow equation (4.8). The fitting results are a_1=23.40, a_2=-2.86 and a_3=276940.7. However, for PS+MG suspension, we didn't observe the SHG dependence on C. Therefore, it is concluded that in PS+MG suspension (the sample we use to do angle-resolved SHG light scattering), the $\chi^{(3)}$ contribution to SHG is negligible (the $\chi^{(3)}$ contribution is less than 10^{-3} of the signal size from PS+MG).

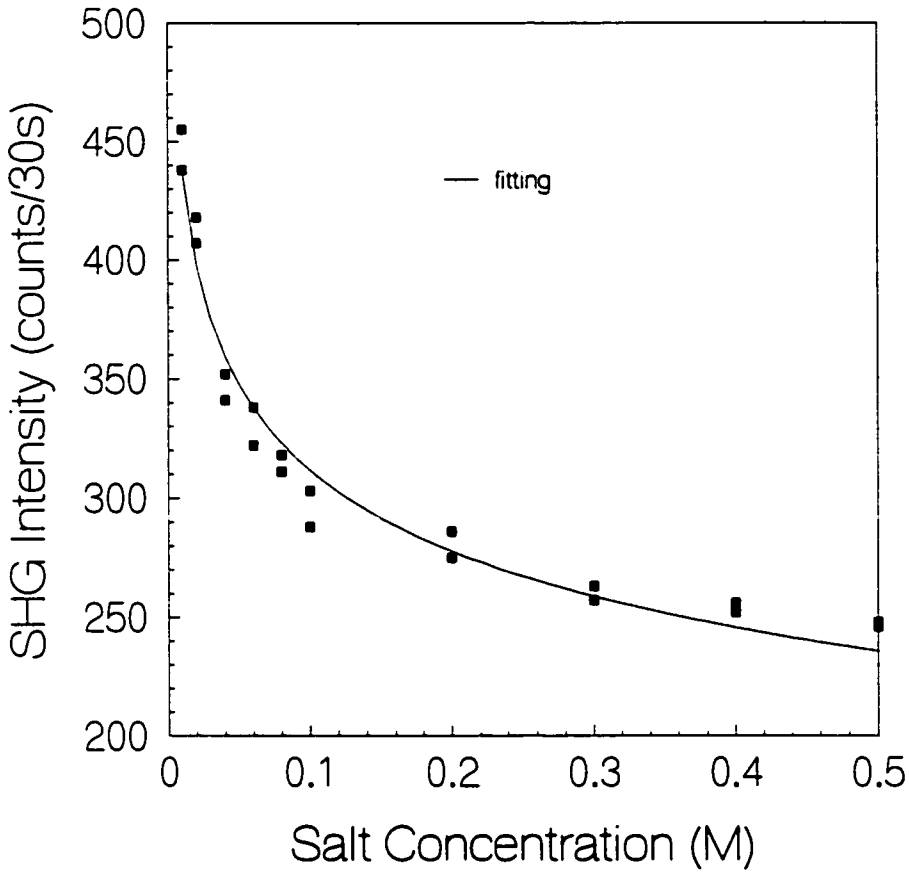

Figure 4.6: SHG dependence on electrolyte concentration for PS only suspension. The solid line is fitting to equation (4.9).

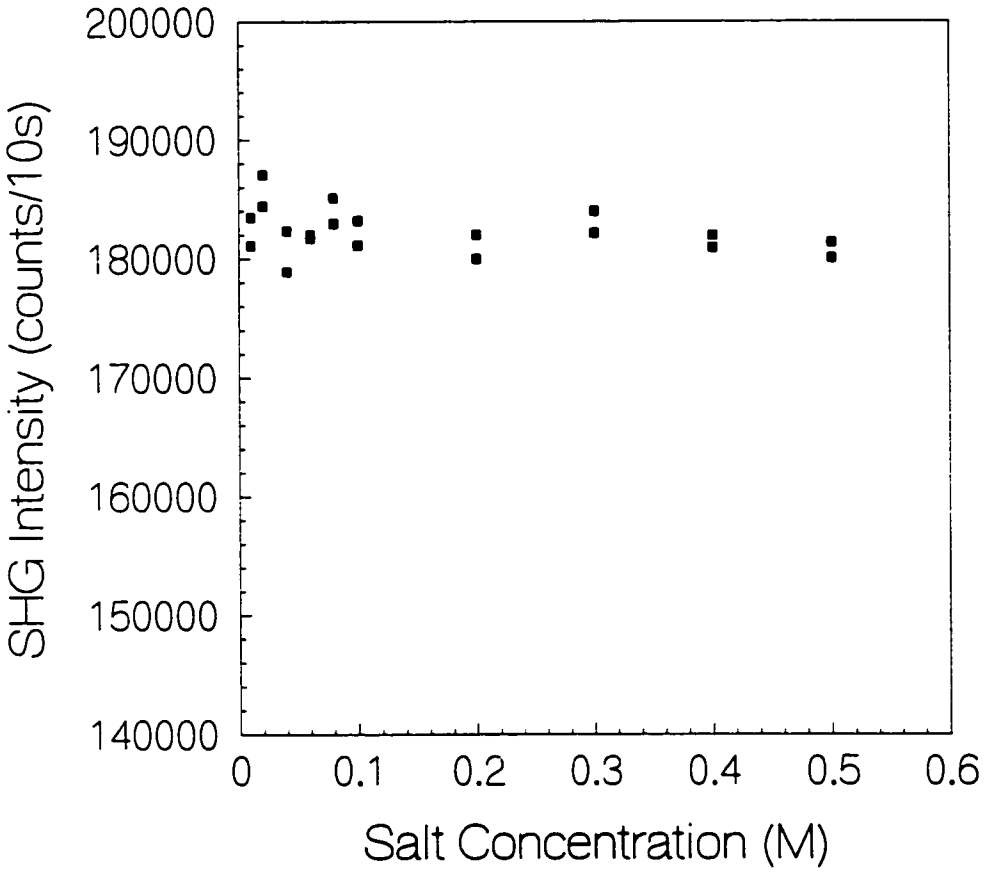

Figure 4.7: SHG dependence on electrolyte concentration for PS+MG suspension. The SHG doesn't obey equation (4.9).

Chapter 5

Angle-resolved SHG Scattering From Colloid Suspension: Data and Analysis

We discussed the experimental setup and the samples in Chapter 3 and chapter 4 respectively. In this Chapter, we will present our data from the measurements of SHG scattering from colloidal suspensions. We also provide a corresponding data analysis.

5.1 Two-photon Angular Profile for Malachite Green Solution Only

We first present the two-photon angular profile for MG solution only. There are some subtle concerns we need to address first. First of all, in our previous discussion of the MG adsorption isotherm on PS, the SHG signal dominated over the background two-photon signal from the MG molecules in solution because we collected the signal over a large solid angle. In our SHG angular scan experiments, however, we use an optical fiber to collect the signal. The very small collection solid angle of the fiber greatly reduces the overall signal intensity. Secondly, the two-photon signal from the

bulk MG molecules has its biggest contribution in the forward scattering direction, while the SHG scattering at forward direction is zero (discussed later). Meaningful angle-resolved scattering results require that we take these background contributions into account, especially in the forward direction.

In light of above-mentioned factors, we first report the angular scan for pure MG solutions of the same $7\mu M$ MG concentration. Throughout this chapter, we maintain the same excitation power and geometry for all measurements to insure consistency of comparison (variation in peak intensity was held within 2% fluctuations). To better illustrate the experimental geometry, we show in Fig. 5.1 the s-polarized and p-polarized directions and the input beam and detection beam geometry. We also show the scattering angle θ. The scattering plane is the xz plane. Note that we also show $\mathbf{r}$ as the coordinates related to detector, and $\mathbf{r}'$ as the coordinates related to nonlinear source (MG molecules on the particle surface). The origin is at the particle center.

Fig. 5.2 shows the angular profile for two-photon signal from MG solution for the polarization configuration of p-in/p-out and s-in/p-out. In Fig. 5.3, we show the angular profile for the polarization configurations of p-in/s-out and s-in/s-out. The most important feature is that in the forward direction ($\theta = 0^0$), the signal is strong and then quickly drops as the scattering angle increases. This big forward scattering arises because the largest scattering volume is in the forward direction, analogous to linear light scattering case [88]. For pure MG solution, the two-photon

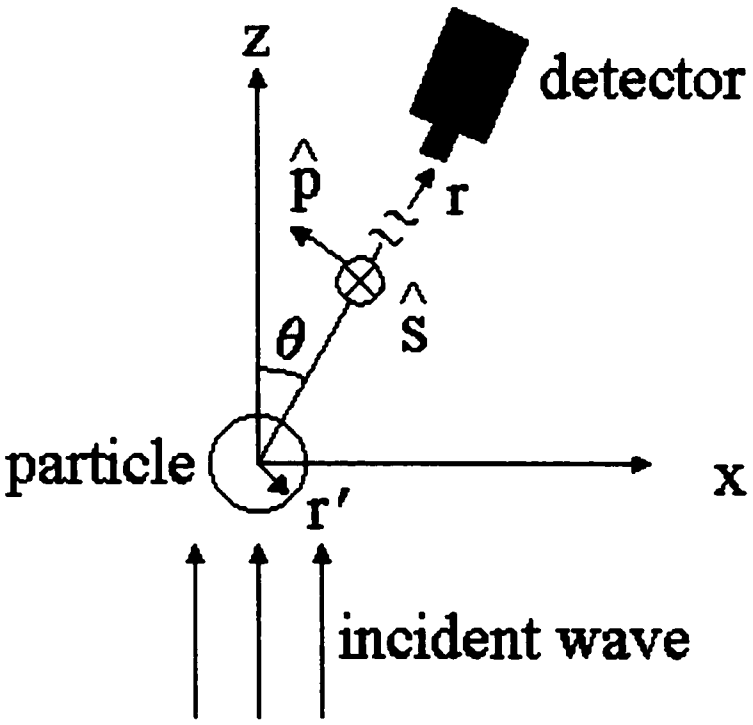

Figure 5.1: Schematic of experimental geometry for SHG scattering from colloidal suspensions. The origin is at the particle center. θ is scattering angle. $\mathbf{r}$ and $\mathbf{r}'$ are coordinates related to detector and source respectively.

signal has similar angular profiles for all four polarization configurations. Only the magnitudes are different. Most notably, the forward scattering direction for s-in/s-out configuration is largest and it is smallest for p-in/p-out configuration.

The origin for the two-photon signal from the MG solution is two-photon excited fluorescence from second electronic excited state S_2 to ground state S_0 [89, 32, 90]. The schematic of electronic states for Malachite Green is shown in Fig. 5.4 with the arrow showing the S_2 to S_0 emission [82]. It is desirable to reduce this 2-photon fluorescence background while still maintaining decent SHG signal-to-noise ratio. We therefore measured the Malachite Green two-photon excited fluorescence spectrum as shown in Fig. 5.5. Our SHG wavelength (420nm) sits at the tail end of this fluorescence spectrum. Our angular scan used the fundamental beam wavelength of 840nm. Lower wavelengths did not achieve better signal-to-noise; this is because the nonlinear response for Malachite Green is peaked at 420nm [32]. Also, we attempted to perform experiments reducing the MG concentration. We didn't achieve much better signal-to-noise in this case either. This is because the SHG signal from the particles depends quadratically on the MG surface coverage (chapter 4). Attempts to lower the MG concentration reduced the SHG signal, especially when the MG concentration went below the adsorption saturation threshold. Therefore, we set our MG concentration to $7\mu M$ in our angular experiments for SHG from PS+MG. At this concentration, particle surface is completely saturated with MG molecules.

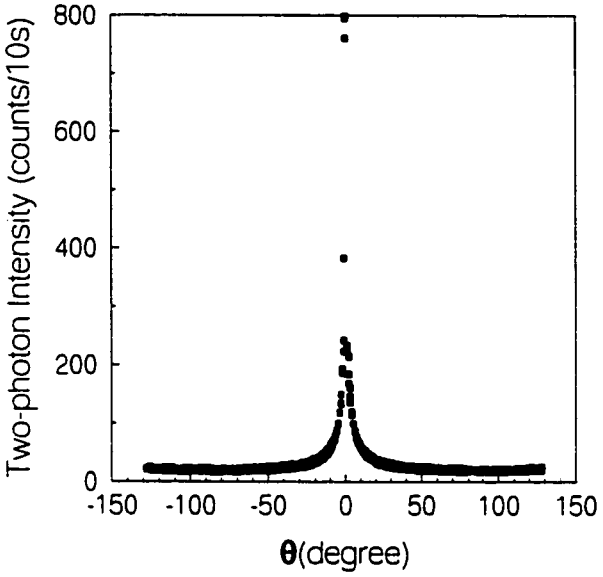

(a)

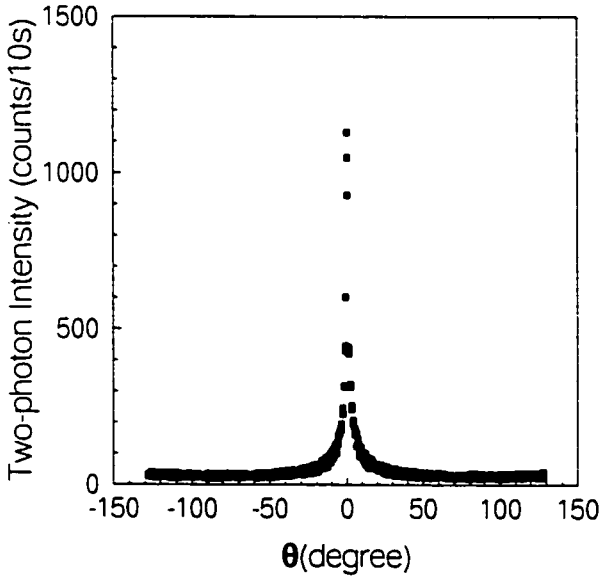

(b)

Figure 5.2: Angular profile for two-photon fluorescence signal for pure MG solution. (a)p-in/p-out (b)s-in/p-out

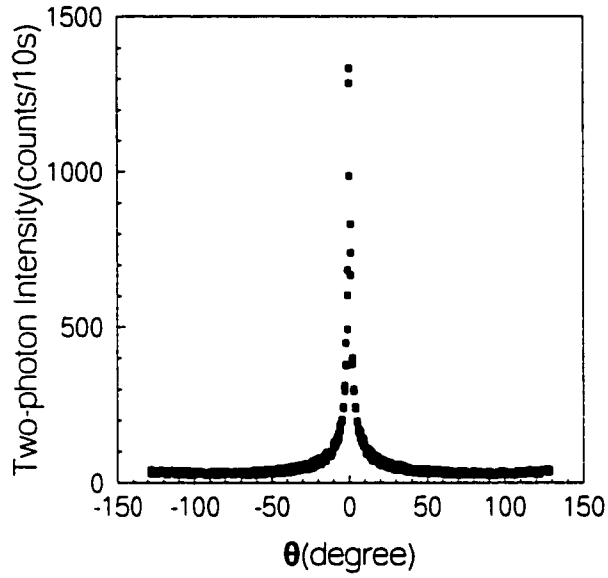

(a)

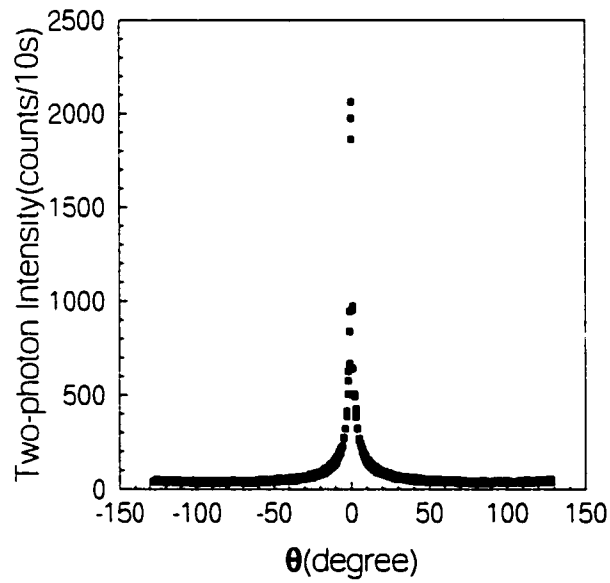

(b)

Figure 5.3: Angular profile for two-photon fluorescence signal for pure MG solution. (a)p-in/s-out (b)s-in/s-out

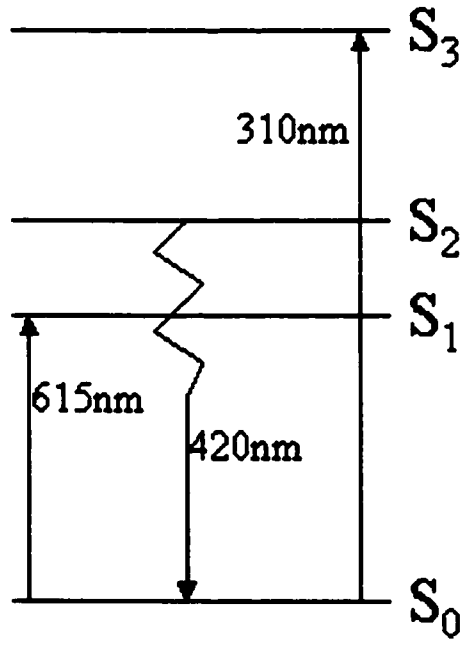

Figure 5.4: Schematic of Malachite Green electronic states. The two-photon excited fluorescence is from S_2 to S_0. Remember, these spectral profiles are much broader than indicated because they are fluorescence emission.

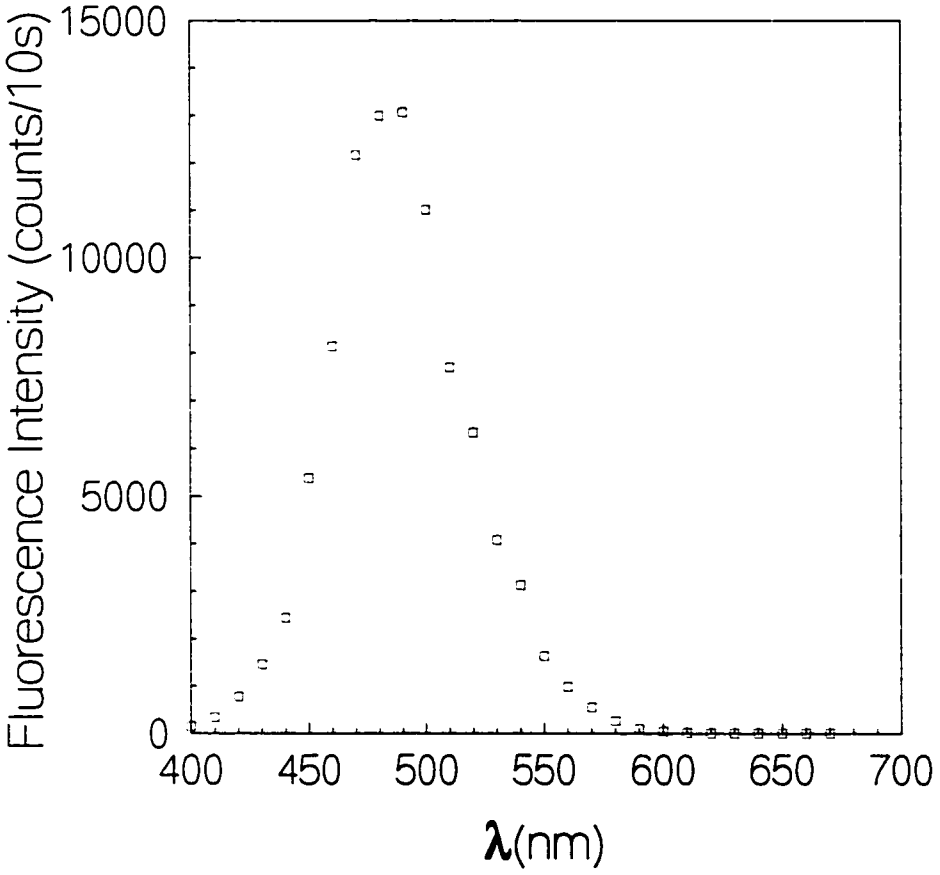

Figure 5.5: Malachite Green two-photon excited fluorescence spectrum. Our SHG wavelength 420nm is sitting at the tail end of this spectrum.

5.2 SHG Scattering Angular Profile From Colloidal Suspension: Raw Measurements

The raw measurements for SHG scattering angular profile from colloidal suspensions are shown in Fig. 5.6, 5.7, 5.8, 5.9, 5.10 and 5.11 for the p-in/p-out and s-in/p-out configurations for all three particle diameters. The SHG scattering for s-out case will be discussed later.

From all the figures, it is clear there is some forward scattering in all cases. Depending upon the particle size and polarization configuration, there is also a distinct peak at some small but non-zero angle. The p-in/p-out configuration gives bigger signals compared to s-in/p-out for the same particles. Also, it is clear that the SHG signal is smallest for the smallest diameter $D = 0.51\mu m$ particle. The signal increases with increasing particle diameter. For $D = 0.98\mu m$ particle, we can also see a second peak.

5.3 SHG Scattering Angular Profile From Colloidal Suspension: Background Substraction

As we described before, the SHG signals from suspensions of colloidal particles in MG solution, contain primary contributions from two sources: bulk MG in solution and adsorbed MG on the particle surfaces. We can write the total electric field at $2\omega_0$,

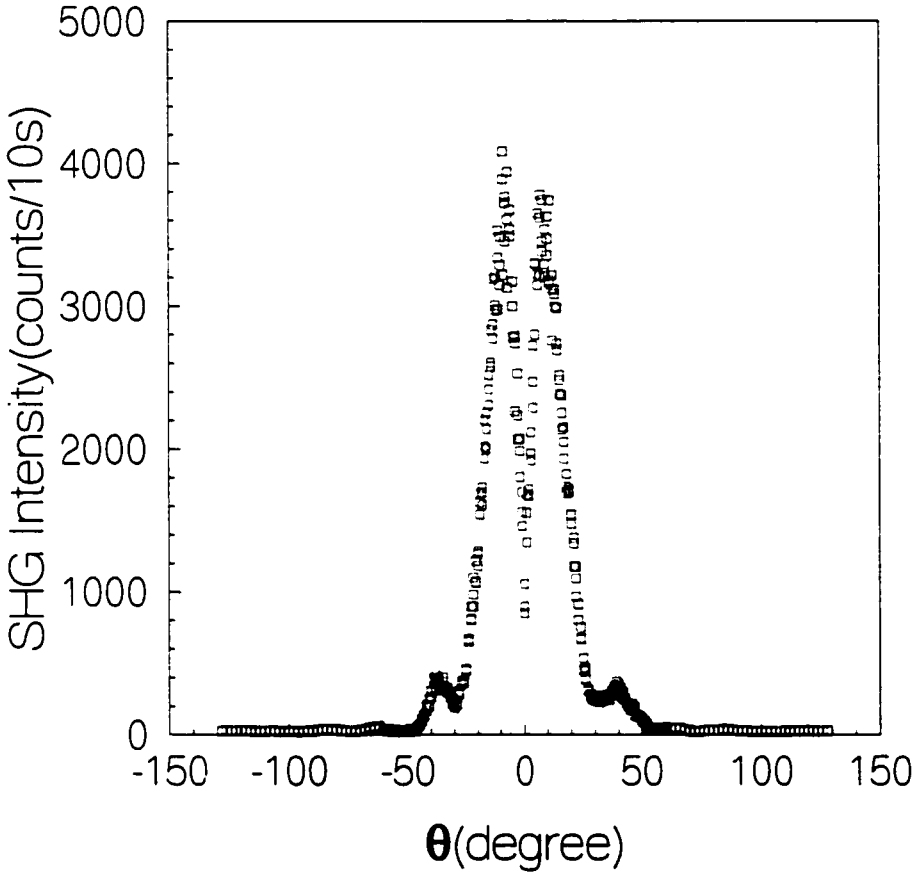

Figure 5.6: Raw measurement for SHG scattering from colloidal suspension. The particle size is 980nm in diameter, the polarization configuration is p-in/p-out.

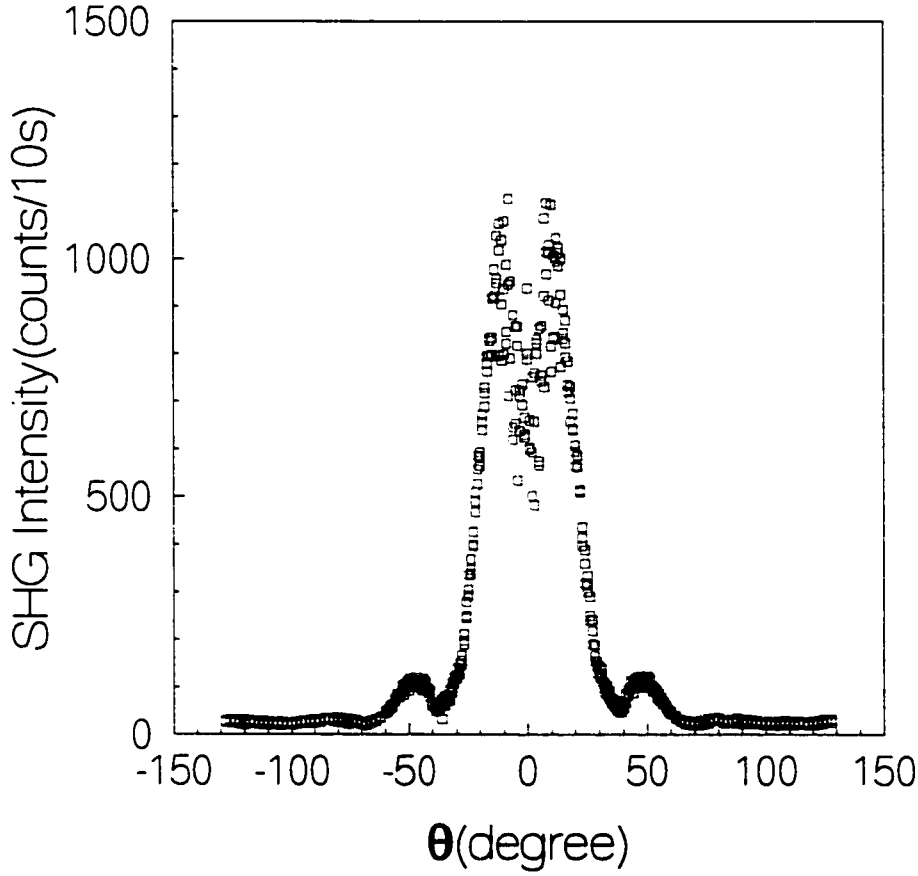

Figure 5.7: Raw measurement for SHG scattering from colloidal suspension. The particle size is 700nm in diameter, the polarization configuration is p-in/p-out.

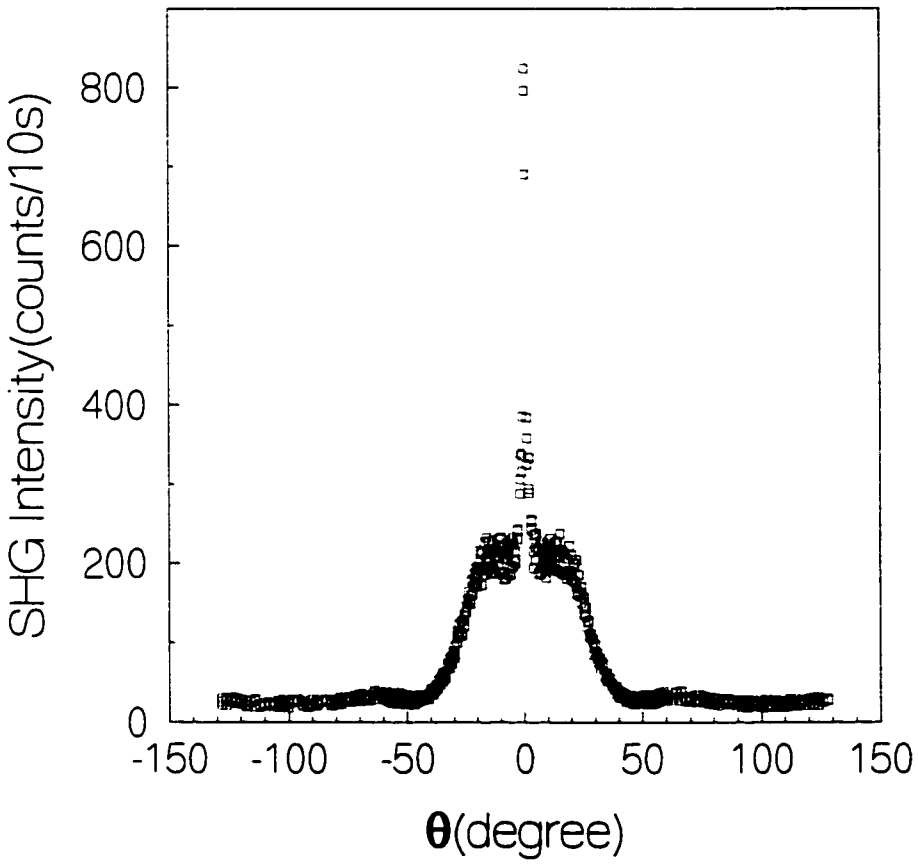

Figure 5.8: Raw measurement for SHG scattering from colloidal suspension. The particle size is 510nm in diameter, the polarization configuration is p-in/p-out.

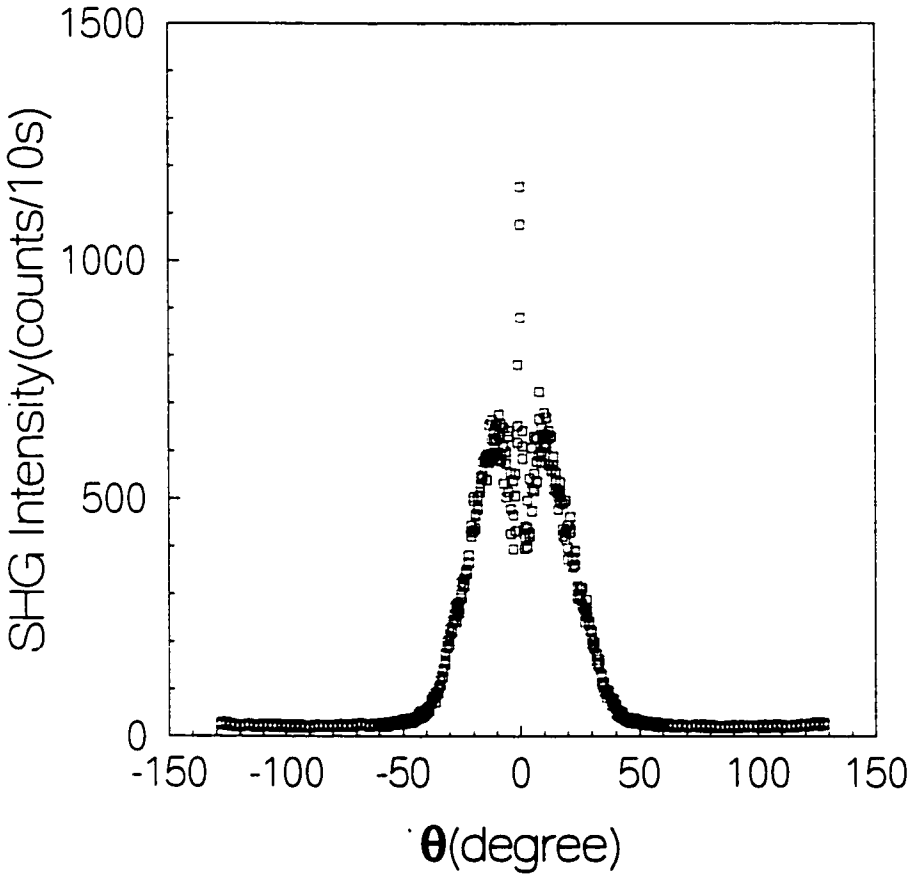

Figure 5.9: Raw measurement for SHG scattering from colloidal suspension. The particle size is 980nm in diameter, the polarization configuration is s-in/p-out.

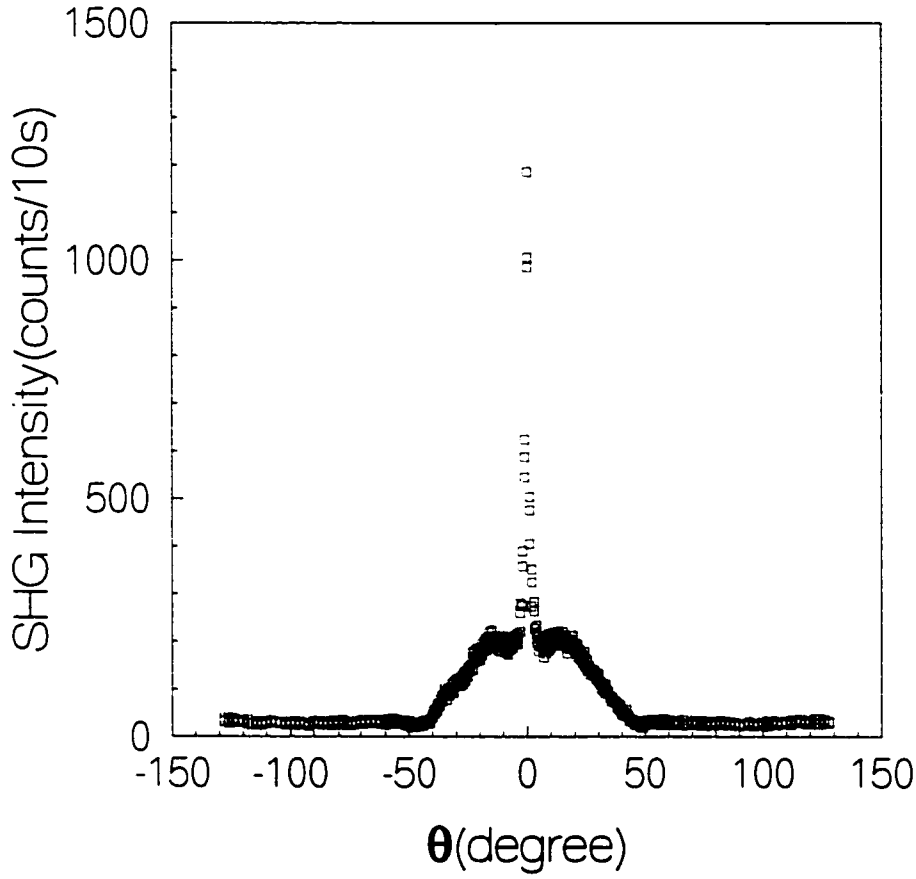

Figure 5.10: Raw measurement for SHG scattering from colloidal suspension. The particle size is 700nm in diameter, the polarization configuration is s-in/p-out.

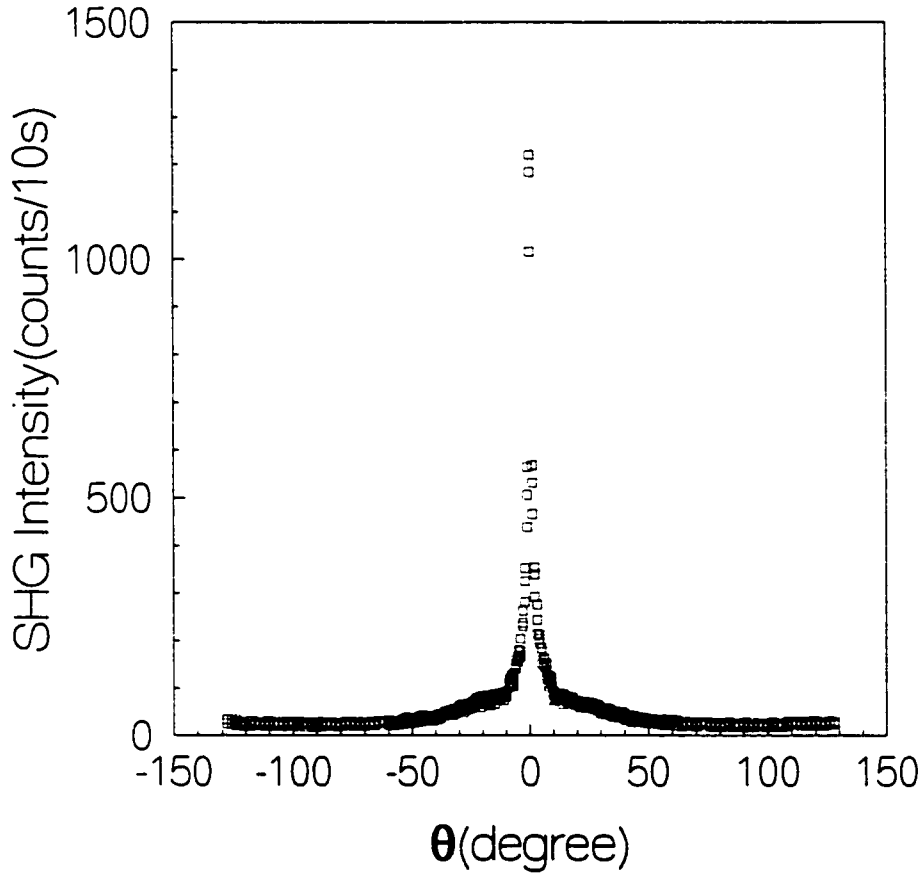

Figure 5.11: Raw measurement for SHG scattering from colloidal suspension. The particle size is 510nm in diameter, the polarization configuration is s-in/p-out.

$\mathbf{E}_{tot}(\mathbf{r}, 2\omega_0)$, as a sum of the fields from these sources, i.e.

$$\mathbf{E}_{tot}(\mathbf{r}, 2\omega_0) = \mathbf{E}_s(\mathbf{r}, 2\omega_0) + \mathbf{E}_{bulk}(\mathbf{r}, 2\omega_0). \tag{5.1}$$

Here $\mathbf{E}_s$ represents the electric field contribution from MG on the particle surfaces. $\mathbf{E}_{bulk}$ represents the electric field contribution from MG in bulk solution. These two contributions are uncorrelated. For example, the particle-induced electric field depends on the positions of all of the particles, and these positions vary randomly in time and in space. In this case, the particle-induced signal intensity, also denoted as $I_s(\mathbf{r}, 2\omega_0)$, may be obtained from the total signal intensity $I_{tot}(\mathbf{r}, 2\omega_0)$ less the background fluorescence intensity, $I_{bulk}(\mathbf{r}, 2\omega_0)$, i.e.

$$I_s(\mathbf{r}, 2\omega_0) = I_{tot}(\mathbf{r}, 2\omega_0) - I_{bulk}(\mathbf{r}, 2\omega_0). \tag{5.2}$$

Therefore, by subtracting the background fluorescence signal from the raw measurements, we effectively obtain the SHG signal from those MG molecules adsorbed on the particle surface. This SHG signal I_s can be described by RGD approximation that we will discuss next.

5.4 Rayleigh-Gans-Debye Approximation For SHG Light Scattering

In this section, we will present the theory of Rayleigh-Gans-Debye approximation for SHG light scattering. We will use this approximation to analyze our data.

The Rayleigh-Gans-Debye (RGD) theory is a widely used approximation in linear light scattering when dealing with the light scattering form factor [1, 2]. It sets the

electric field inside the particle to be the same as that of the incident field. The approximation in RGD theory is valid when [2]

$$|m-1| \ll 1, \tag{5.3}$$

and

$$kL|m-1| \ll 1. \tag{5.4}$$

Here $m = \frac{n_p}{n_0}$ is the ratio of particle index of refraction to that of the medium. L is the largest dimension of the particle. k is the wavevector. The first approximation insures that the incident wave is not appreciably reflected at the particle-medium interface. The second approximation insures that the incident wave does not undergo appreciable phase or amplitude change in the particle. RGD theory is an approximation that works very well for light scattering at small angles region (i.e. in the near forward direction) [1]. For example, Kerker [1] showed that for a particle with radius $R \sim 0.5\mu m$, scattering light at 10^0 angle, and having an index of refraction of ~ 1.57, the linear scattering error is only about 10% if the background medium is water. At larger angles (e.g. $> 45^0$) however, this error can increase to 100%. RGD theory for linear light scattering predicts the following form factor

$$I(\theta) = \frac{9}{(QR)^6}(sinQR - QRcosQR)^2. \tag{5.5}$$

Where $I(\theta)$ is the scattering form factor, R is the particle radius, and Q is the scat-

tering vector defined as

$$Q = \frac{4\pi}{\lambda} n_p sin\frac{\theta}{2}. \tag{5.6}$$

Again, n_p is the particle index of refraction. λ is the wavelength of incident beam and θ is the scattering angle. A derivation of equation (5.5) is given in Appendix E.

For our SHG light scattering, the dominant features occur at angles less than 10^0. We have performed a rigorous Mie theory calculation for linear light scattering (see Appendix F), and compared its form factor result with the RGD form factor as shown in Fig. 5.12. The closeness of these two calculations validate our use of RGD theory in the analysis of our SHG signals. As expected, at small angle, the RGD theory gives a very good representation of the data.

Therefore, instead of rigorously solving the nonlinear light scattering wave equation, which is a very complicated challenge (there are no publications in this regard so far), we develop a nonlinear RGD theory for SHG light scattering which we expect to provide a good approximation of our measured angular profiles.

5.4.1 Calculations of Surface Nonlinear Polarizations

In this section, we calculate the nonlinear source polarizations on the particle surface induced by the incident wave. We use a coordinate system as shown in Fig. 5.13. The fundamental light propagates along the $\hat{z}$ direction, and the xz plane is the scattering plane (see Fig. 5.1). On the polarization terminology, s-polarization means that

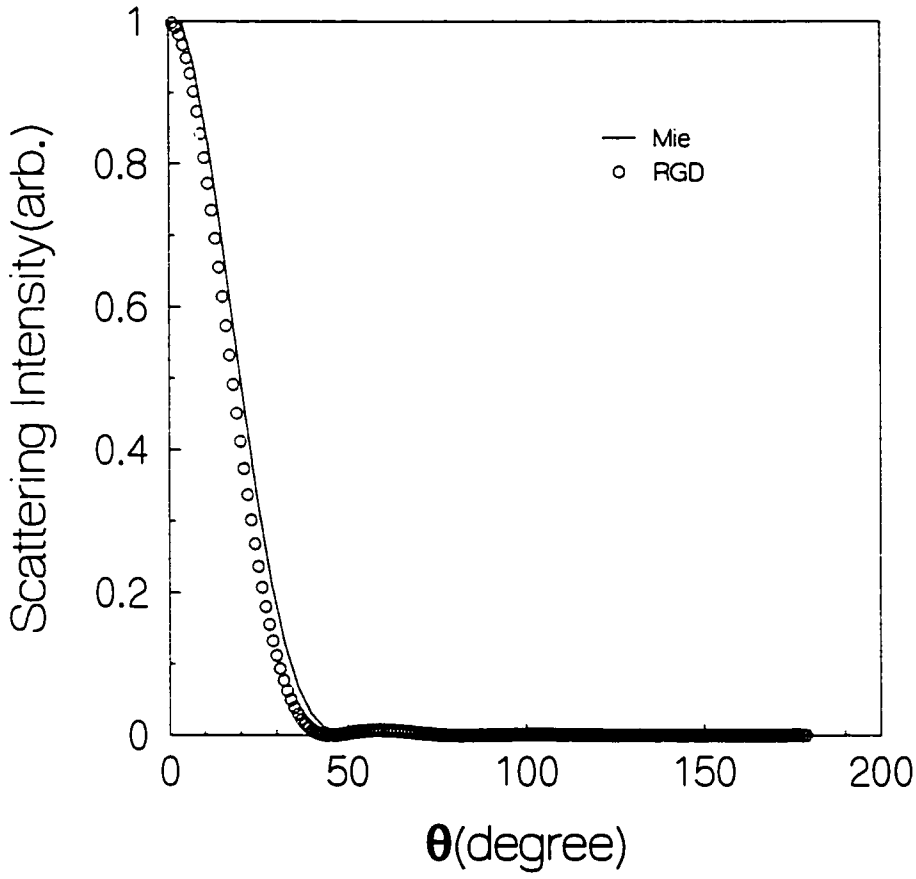

Figure 5.12: The linear form factor comparison between rigorous Mie theory and that of Rayleigh-Gans-Debye approximation. It is remarkable that these two calculations give very close result. The model particle is Polystyrene of D$\sim$ 1μm. Incident wavelength is 840nm, the surrounding medium is water.

polarization direction is normal to the scattering plane while p-polarization means that polarization direction lies parallel to the scattering plane. Thus the s-polarization electric field has only a y-component, while p-polarization field can have both x- and z-components.

Malachite Green molecules are radially oriented on the PS surface. Therefore, we assume that MG molecule has only non-zero hyperpolarizability along radial direction. We denote this non-zero hyperpolarizability as $\alpha^{(2)} = \alpha^{(2)}_{rrr} \neq 0$, with all other elements of $\alpha^{(2)}$ set to zero.

We divide the discussion into two cases according to whether the fundamental beam is s-polarized or p-polarized.

(1) Fundamental Beam s-polarized

The incident field can be written as

$$\mathbf{E}_i = E_0 \hat{e_y} e^{i(kz-\omega_0 t)}. \tag{5.7}$$

Here $\hat{e_y}$ is the unit vector along y-direction. This incident field on the sphere surface can be written in the spherical coordinates as

$$\mathbf{E}_i = E_0(sin\phi sin\theta \hat{e_r} + sin\phi cos\theta \hat{e_\theta} + cos\phi \hat{e_\phi}) e^{i(kz-\omega_0 t)}. \tag{5.8}$$

Here $\hat{e_r}$, $\hat{e_\theta}$ and $\hat{e_\phi}$ are unit vectors along r, θ and ϕ direction. Now, the nonlinear

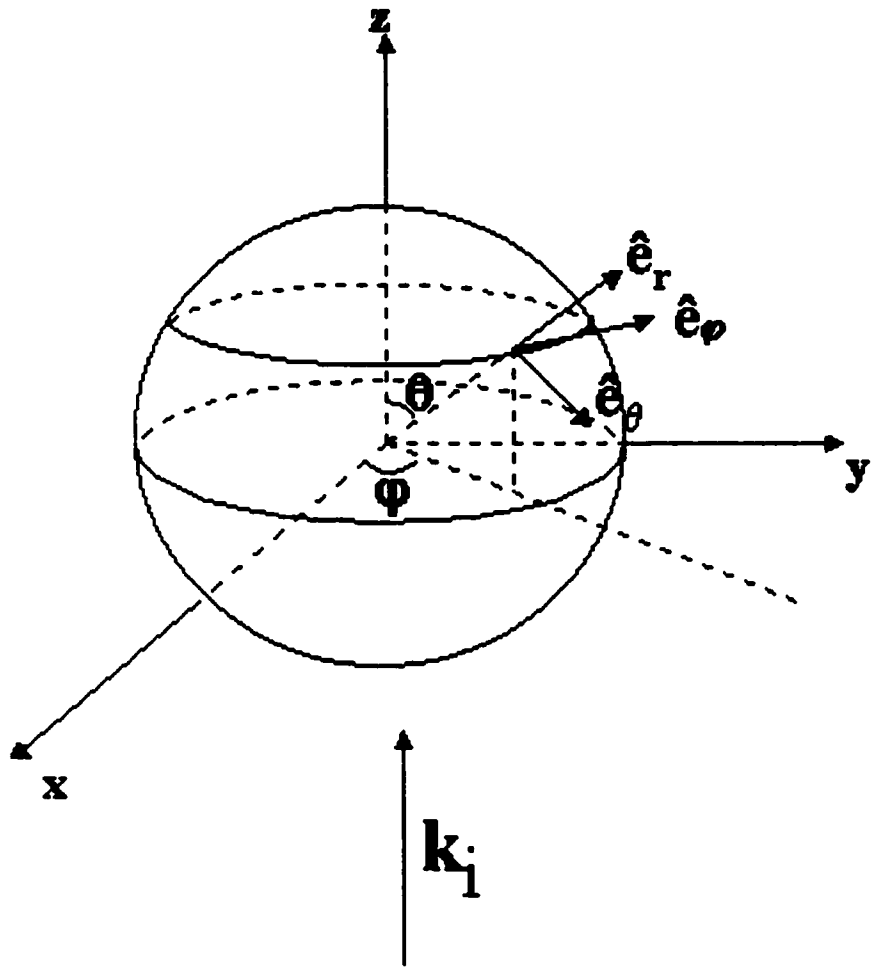

Figure 5.13: The coordinate system for SHG RGD Model. $\mathbf{k}_i$ is the wave vector of the incident wave. xy is scattering plane.

polarization can be calculated

$$\begin{aligned} P_r(2\omega_0) &= \alpha^{(2)}_{rij} E_i E_j \\ &= \alpha^{(2)}_{rrr} E_r E_r \\ &= \alpha^{(2)}_{rrr} E_0^2 sin^2\phi sin^2\theta e^{i(2kz-2\omega_0 t)}. \end{aligned}$$

Similarly, we obtain $P_\theta = 0$, P_ϕ=0. Finally, we find

$$\mathbf{P}(2\omega_0) = \alpha^{(2)} E_0^2 sin^2\phi sin^2\theta e^{i(2kz-2\omega_0 t)} \hat{e}_r. \tag{5.9}$$

One thing to note is that the polarization magnitude is position dependent even though it always points in radial direction.

(2)Fundamental Beam p-polarized

The incident field can be written as

$$\mathbf{E}_i = E_0 \hat{e}_x e^{i(kz-\omega_0 t)}. \tag{5.10}$$

Following the same procedures as in (1), we find

$$\mathbf{P}(2\omega_0) = \alpha^{(2)} E_0^2 cos^2\phi sin^2\theta e^{i(2kz-2\omega_0 t)} \hat{e}_r. \tag{5.11}$$

5.4.2 Complete Solution of Nonlinear Wave Equation

The general solution for nonlinear wave equation (2.8) in chapter 2 is

$$\mathbf{E}_{2\omega_0}(\mathbf{r}) = \frac{(2\omega_0)^2}{c^2} \int d^3\mathbf{r}' \frac{e^{ik_{2\omega_0}|\mathbf{r}-\mathbf{r}'|}}{|\mathbf{r}-\mathbf{r}'|} \mathbf{P}^{NL}_{2\omega_0}(\mathbf{r}'). \tag{5.12}$$

Note that $\mathbf{r}$ corresponds to the detector coordinate, and $\mathbf{r}'$ corresponds to the nonlinear source coordinate which has to be integrated. Now we again divide the discussion into two cases, for fundamental beam is s-polarized and p-polarized.

(1)Fundamental Beam s-polarized

We substitute equation (5.9) into equation (5.12), using the far field approximation $|\mathbf{r}-\mathbf{r}'| \approx r - \hat{n}\cdot\mathbf{r}'$ and $\frac{1}{|\mathbf{r}-\mathbf{r}'|} \sim \frac{1}{r}$ (leading term), where $\hat{n} = \frac{\mathbf{r}}{r}$, then we get

$$\mathbf{E}_{2\omega_0}(\mathbf{r}) = \frac{2\omega_0}{c^2}\frac{e^{ik_{2\omega_0}r}}{r}\alpha^{(2)}E_0^2\int d^3\mathbf{r}'(\hat{e_y}\cdot\hat{e_{r'}})^2 e^{i\mathbf{q}\cdot\mathbf{r}'}\hat{e_{r'}}. \tag{5.13}$$

where we use the relationship $(\hat{e_y}\cdot\hat{e_r})^2 = sin^2\phi sin^2\theta$. $\mathbf{q}$ is called nonlinear wave scattering vector and is defined as

$$\mathbf{q} = 2\mathbf{k}_{\omega_0} - \mathbf{k}_{2\omega_0}. \tag{5.14}$$

The directional relationship between $\mathbf{q}$, $\hat{x}$, $\hat{z}$, $\mathbf{k}_{\omega_0}$, $\mathbf{k}_{2\omega_0}$ and scattering angle θ are depicted in Fig. 5.14. Where we also introduce another set of coordinates $(\hat{i}\hat{j}\hat{k})$. $\hat{j}$ is parallel to $\hat{y}$, $\hat{k}$ is the unit vector parallel to $\mathbf{q}$. We also introduce the unit vector $\hat{o}_\perp$ which is perpendicular to $\mathbf{k}_{2\omega_0}$. $\hat{o}_\perp$ is the transverse direction in the scattering plane. The magnitude of $\mathbf{q}$ is obtained from the simple geometric relationship with assumption $n_{\omega_0} = n_{2\omega_0}$, i.e.

$$|\mathbf{q}| = 2k_{2\omega_0}sin\frac{\theta}{2}. \tag{5.15}$$

The integral in equation (5.13) can be calculated to get (Appendix C)

$$\int d^3\mathbf{r}'(\hat{e_y}\cdot\hat{e_{r'}})^2 e^{i\mathbf{q}\cdot\mathbf{r}'}\hat{e_{r'}} = -\frac{4\pi R}{iq}F_s(\theta)(-cos\frac{\theta}{2}\hat{x} + sin\frac{\theta}{2}\hat{z}). \tag{5.16}$$

where $F_s(\theta)$ is the nonlinear light scattering form factor

$$F_s(\theta) = \frac{3}{q^3R^3}[(1-\frac{q^2R^2}{3})sinqR - qRcosqR]. \tag{5.17}$$

Finally, we obtain the complete SHG field solution for s-polarized excitation as

$$\mathbf{E}_{2\omega_0}(\mathbf{r}) = \frac{(2\omega_0)^2}{c^2}\frac{e^{ik_{2\omega_0}}}{r}\alpha^{(2)}E_0^2\frac{-4\pi R}{iq}F_s(\theta)(-cos\frac{\theta}{2}\hat{x} + sin\frac{\theta}{2}\hat{z}). \tag{5.18}$$

(2)Fundamental Beam p-polarized

Similarly, the SHG electric field for p-polarized excitation can be written in a form as in equation (5.13), except the integral is replaced by following

$$\int d^3\mathbf{r}'(\hat{e_x}\cdot\hat{e_{r'}})^2 e^{i\mathbf{q}\cdot\mathbf{r}'}\hat{e_r'}$$

this integral is calculated to obtain (Appendix D)

$$\int d^3\mathbf{r}'(\hat{e_x}\cdot\hat{e_{r'}})^2 e^{i\mathbf{q}\cdot\mathbf{r}'}\hat{e_r'} = -\frac{4\pi R}{iq}F_s(\theta)(-sin\theta\hat{i} + sin^2\frac{\theta}{2}\hat{k}) + \frac{8\pi R}{iq}F_p(\theta)cos^2\frac{\theta}{2}\hat{k}. \tag{5.19}$$

where $F_p(\theta)$ is another nonlinear light scattering form factor defined as

$$F_p(\theta) = \frac{3}{q^3R^3}[(1-\frac{1}{2}q^2R^2)sinqR - (qR - \frac{1}{6}q^3R^3)cosqR]. \tag{5.20}$$

Finally, we obtain the complete SHG field solution for p-polarized excitation as

$$\begin{aligned}\mathbf{E}_{2\omega_0}(\mathbf{r}) &= \frac{(2\omega_0)^2}{c^2}\frac{e^{ik_{2\omega_0}r}}{r}\alpha^{(2)}E_0^2\frac{4\pi R}{iq}\{cos\frac{\theta}{2}(3F_s(\theta)sin^2\frac{\theta}{2} - 2F_p(\theta)cos^2\frac{\theta}{2})\hat{e_x} \\ &\quad + sin\frac{\theta}{2}[F_s(\theta)(cos\theta + cos\frac{\theta}{2}) + 2F_p(\theta)cos^2\frac{\theta}{2}]\hat{e_z}\}. \end{aligned} \tag{5.21}$$

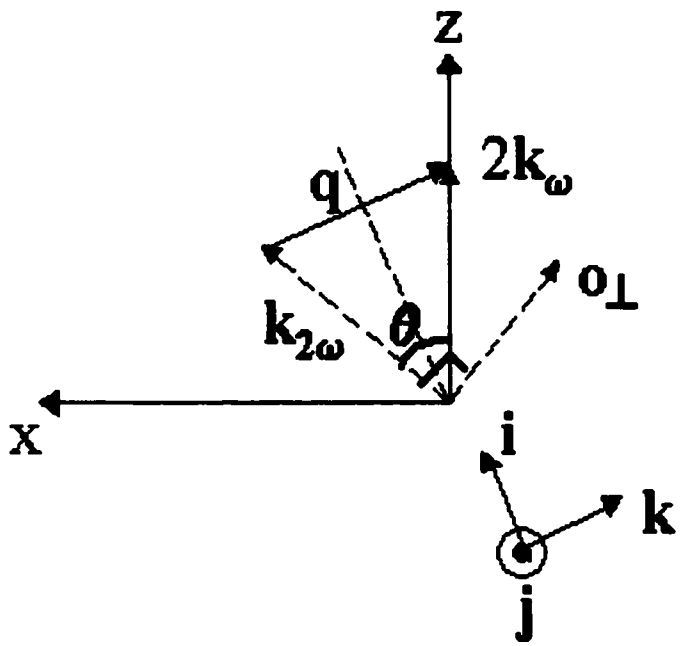

Figure 5.14: The directional relationship between various vectors in SHG RGD theory. xz is scattering plane. **q** is scattering vector. $\mathbf{o}_\perp$ is the transverse unit vector relative to $\mathbf{k}_{2\omega}$.

5.4.3 Experimentally Detected SHG field

The complete SHG field in equation (5.18) and (5.21) contain both the transverse and longitudinal components relative to the radiation direction (outgoing $\mathbf{k}_{2\omega_0}$ direction) in the scattering plane. In our experimental situation, we detect the transverse part. Therefore, we need to "filter" out these transverse fields. We use the subscript "rad" to denote the transverse radiated field in the following treatment.

Using the geometrical relationship between different directions from Fig. 5.14, specifically,

$$\mathbf{k} = -cos\frac{\theta}{2}\hat{x} + sin\frac{\theta}{2}\hat{z}, \qquad \hat{i}\cdot\hat{o}_\perp = sin\frac{\theta}{2}, \qquad \hat{k}\cdot\hat{o}_\perp = cos\frac{\theta}{2}$$

we obtain the radiated SHG electric field for s-polarized excitation:

$$\mathbf{E}_{2\omega_0}(\mathbf{r})_{rad} = \frac{(2\omega_0)^2}{c^2}\frac{e^{ik_{2\omega_0}r}}{r}\alpha^{(2)}E_0^2\frac{-4\pi R}{iq}F_s(\theta)cos\frac{\theta}{2}\hat{o}_\perp. \tag{5.22}$$

And for p-polarized excitation:

$$\mathbf{E}_{2\omega_0}(\mathbf{r})_{rad} = \frac{(2\omega_0)^2}{c^2}\frac{e^{ik_{2\omega_0}r}}{r}\alpha^{(2)}E_0^2\frac{4\pi R}{iq}[F_s(\theta)cos\frac{\theta}{2} + (2F_p(\theta) - F_s(\theta))cos^3\frac{\theta}{2}]\hat{o}_\perp. \tag{5.23}$$

5.5 Data Analysis Using the RGD Approximation

We are ready to interpret our data with the RGD approximation. From equation (5.22) and (5.23), we derive the following expression to fit our extracted $I_s(\mathbf{r}, 2\omega_0)$, for the s-in/p-out configuration:

$$I_{sp}(\theta) = A_{sp}\frac{|F_s(\theta)cos\frac{\theta}{2}|^2}{sin^2\frac{\theta}{2}sin\theta}. \tag{5.24}$$

Similarly we derive the following expression to fit our extracted $I_s(\mathbf{r}, 2\omega_0)$ for the p-in/p-out configuration:

$$I_{pp}(\theta) = A_{pp}\frac{|F_s(\theta)cos\frac{\theta}{2}sin^2\frac{\theta}{2} + 2F_p(\theta)cos^3\frac{\theta}{2}|^2}{sin^2\frac{\theta}{2}sin\theta}. \tag{5.25}$$

Here A_{sp} and A_{pp} are fitting parameters. Note that we include factor $\frac{1}{sin\theta}$ in our fitting which takes into account the scattering volume effect [88].

The results of our angular profile fitting using RGD approximation are shown in Fig. 5.15, 5.16, 5.17, 5.18, 5.19 and 5.20 for various polarization configurations and various particle sizes. The lines are fits using RGD approximations. It is seen that, except some deviations at the larger scattering angles, the RGD model fits fairly well. Most importantly, the SHG forward scattering is indeed depressed as also predicted by others for the SHG Rayleigh scattering case [38]. Comparing these figures, we clearly see that the p-in/p-out configurations have bigger signal compared to the s-in/p-out configurations. The larger particle (e.g. 980nm) also has a bigger signal compared to smaller ones (e.g. 510nm). Also, we observed that the scattering peak is small at non-zero angles ($\theta \sim 10^0$ for D=980nm) and this peak position shifts to larger angle as the particle size decreases. Another important suggestion from our experiment is that one can isolate the particle contributions to the signal by detecting the scattered SH light off-axis.

5.5.1 Discussion On s-polarized SHG Radiation

So far we have discussed the SHG radiation for both p-in/p-out and s-in/p-out configurations in detail. We will discuss the case when SHG radiation is s-polarized now.

It turns out that s-polarized radiation is forbidden. This can be seen from equation (5.18) and (5.21) corresponding to s-polarized and p-polarized excitation respectively. There is no y-component SHG field in equation (5.18) and (5.21). Therefore, there is no s-polarized SHG radiation. The physical origin of this effect is that for every nonlinear source polarization at azimuthal angle ϕ, there is another oppositely oriented nonlinear source polarization at angle $\phi+\pi$. For s-polarized SHG output, these polarizations add up to cancel each other when integrate with respect to azimuthal angle ϕ. However, for p-polarized SHG radiation, this isn't the case because p-polarized radiation can include both x and z components. The z-component of the polarization doesn't have the same *azimuthal* dependence as the y-component. When integrating over the azimuthal angles, the z-component will generally give non-zero results, thus generating non-zero p-polarized SHG radiation.

Our measurements for s-polarized SHG radiation indeed confirm this expectation. In Fig. 5.21 and Fig. 5.22 we show the s-polarized SHG radiation in raw measurement and extracted signal respectively. Barring the big error bar at $\theta = 0$ direction, which is reasonably expected when background fluorescence is strongest while the signal

is smallest in this direction, the s-polarized SHG radiation basically looks flat as expected.

5.6 General Comparision with SHG Rayleigh scattering

As we note in Chapter 1, Heinz's group developed and published the SH light scattering theory in the Rayleigh approximation [38]. In this section, we compare their model with our current model and discuss the differences. Fig. 5.23 shows the schematic view of their model and our model.

First of all, the two models deal with different experimental situations. For SH Rayleigh scattering, it considers the SH scattering from an isotropic sphere. While in our case, we consider the SH scattering from sphere coated with nonlinear dyes. This difference in experimental situation has a significant impact on the way to treat this problem.

Secondly, SH Rayleigh scattering deals with particles with diameter much less than the optical wavelength, while our current condition deals with particles with diameter comparable with optical wavelength. One important result of this is that in dipole approximation, SH Rayleigh scattering will incur cancellation of radiation from diferent parts of the sphere while our model will not (see section 2.3).

Thirdly, the SH scattering signal has completely different origin. The radiation cancellation noted above dictates that in SH Rayleigh scattering, the leading contri-

bution to SH signal is *quadrupole* in nature and the signals are generated from the *bulk*. While in our model, due to the presence of surface adsorbed nonlinear dyes, the leading contribution to the SH signal is *dipole* in nature and the signals are generated from the *surface* of the particle. In our model, we *only* consider this leading contribution which is much larger than the higher-order contributions.

One consequence of the two SH signal origins is the difference in signal magnitude. Our experimental situation is dipole-allowed and has a much larger signal magnitude than the SH Rayleigh scattering case. In fact, the signal from SH Rayleigh scattering is so small that there is no any reported experimental observation of SH Rayleigh scattering so far.

Despite the major differences, SH Rayleigh scattering and our model do share one general feature, i.e. the forward and backward SH scattering are forbidden. This is the direct result of radiation cancellation in forward and backward direction and is unique to SH scattering. This is also the biggest difference on nonlinear scattering compared with linear light scattering.

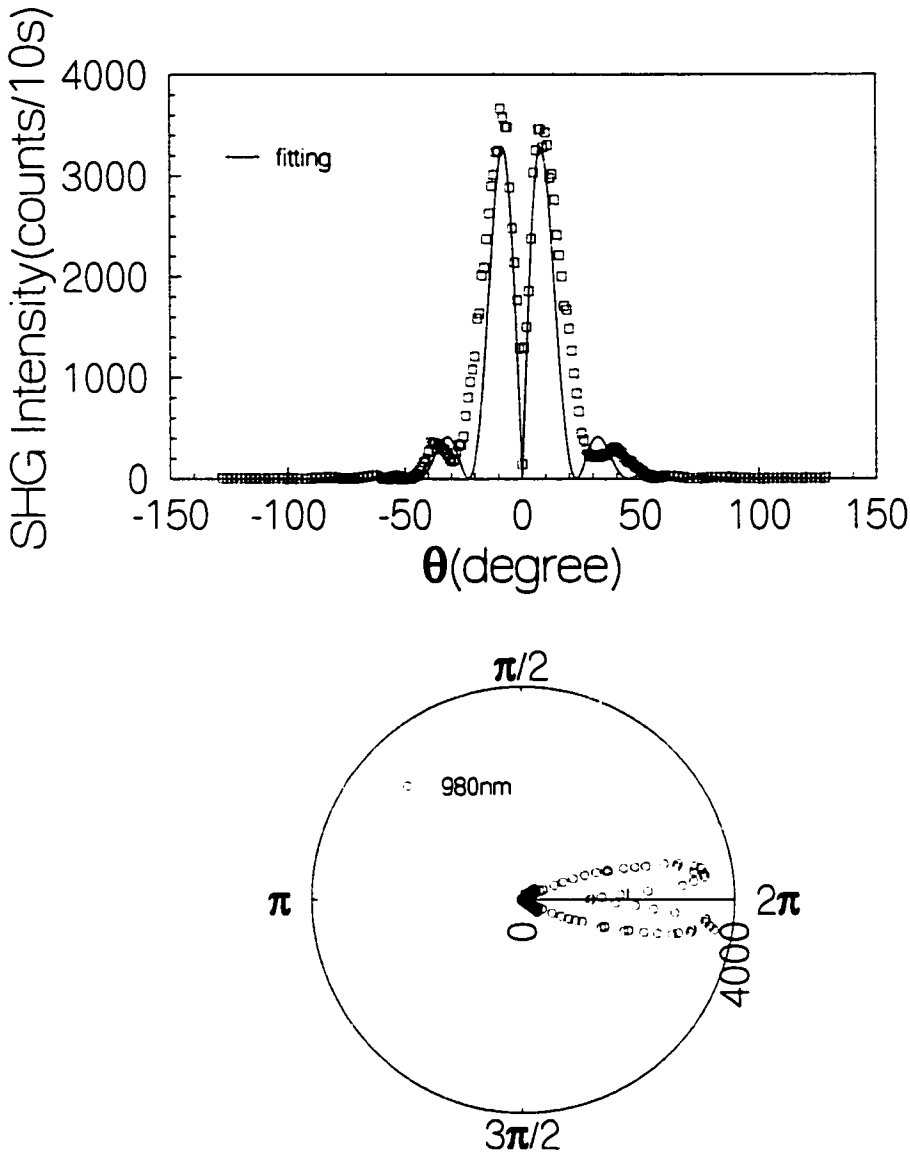

Figure 5.15: SHG scattering from colloidal suspension. Top: x-y plot. Bottom: polar plot. The particle is 980nm in diameter. The polarization configuration is p-in/p-out. Solid line is fitting to RGD model.

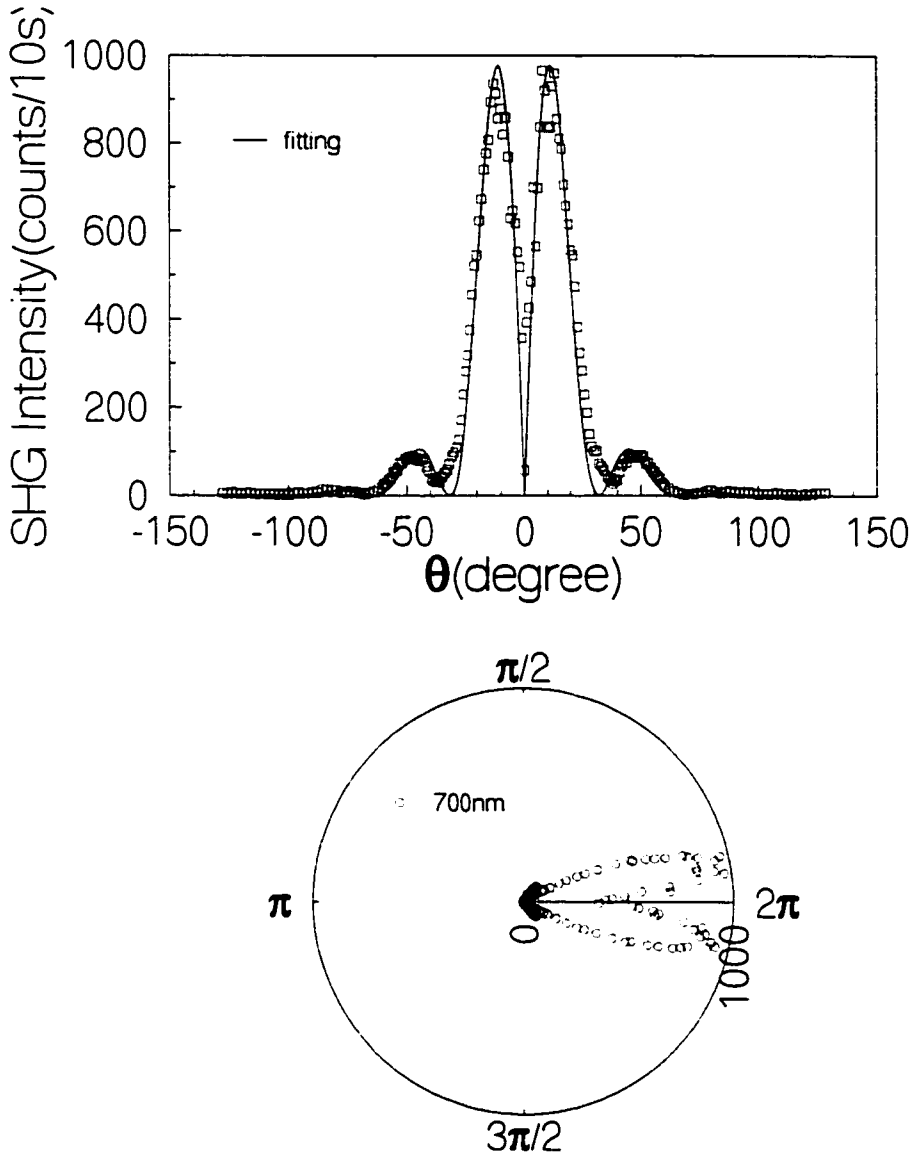

Figure 5.16: SHG scattering from colloidal suspension. Top: x-y plot. Bottom: polar plot. The particle is 700nm in diameter. The polarization configuration is p-in/p-out. Solid line is fitting to RGD model.

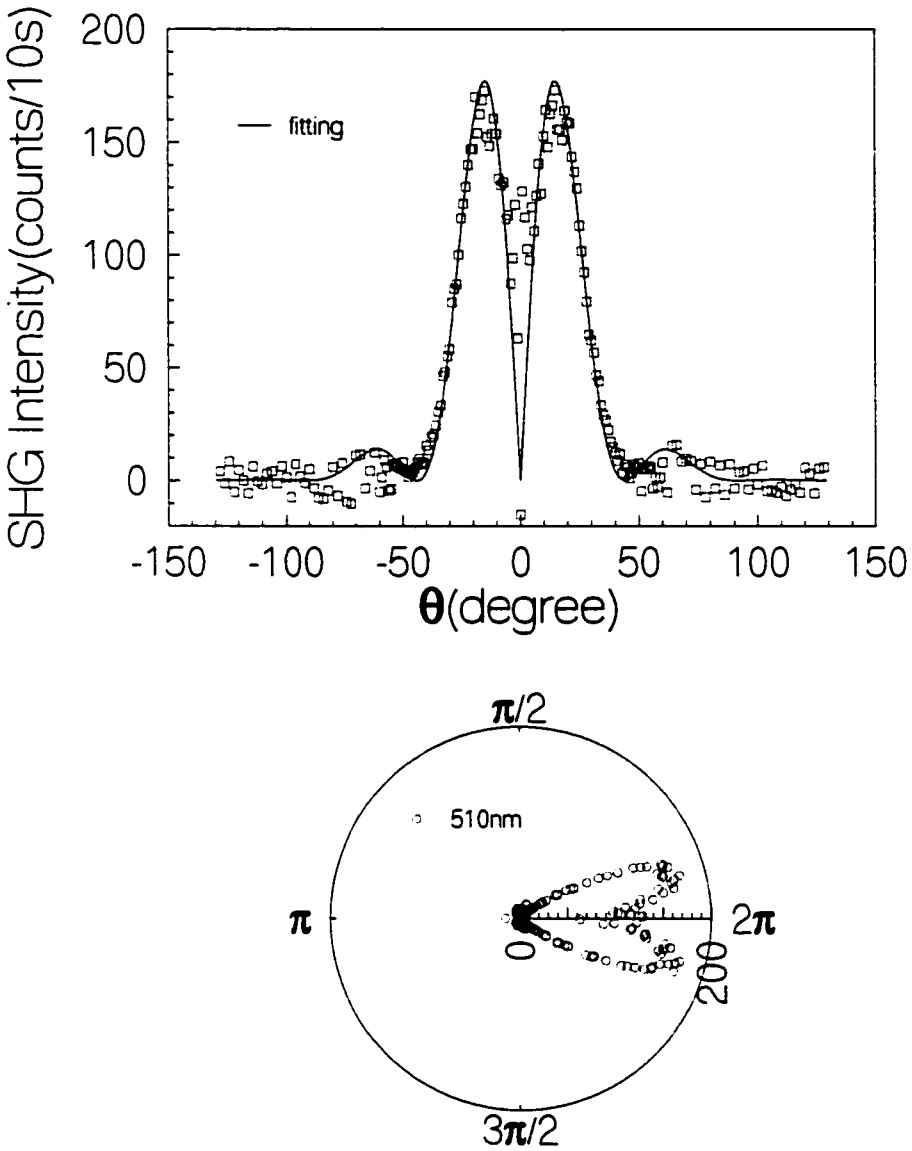

Figure 5.17: SHG scattering from colloidal suspension. Top: x-y plot. Bottom: polar plot. The particle is 510nm in diameter. The polarization configuration is p-in/p-out. Solid line is fitting to RGD model.

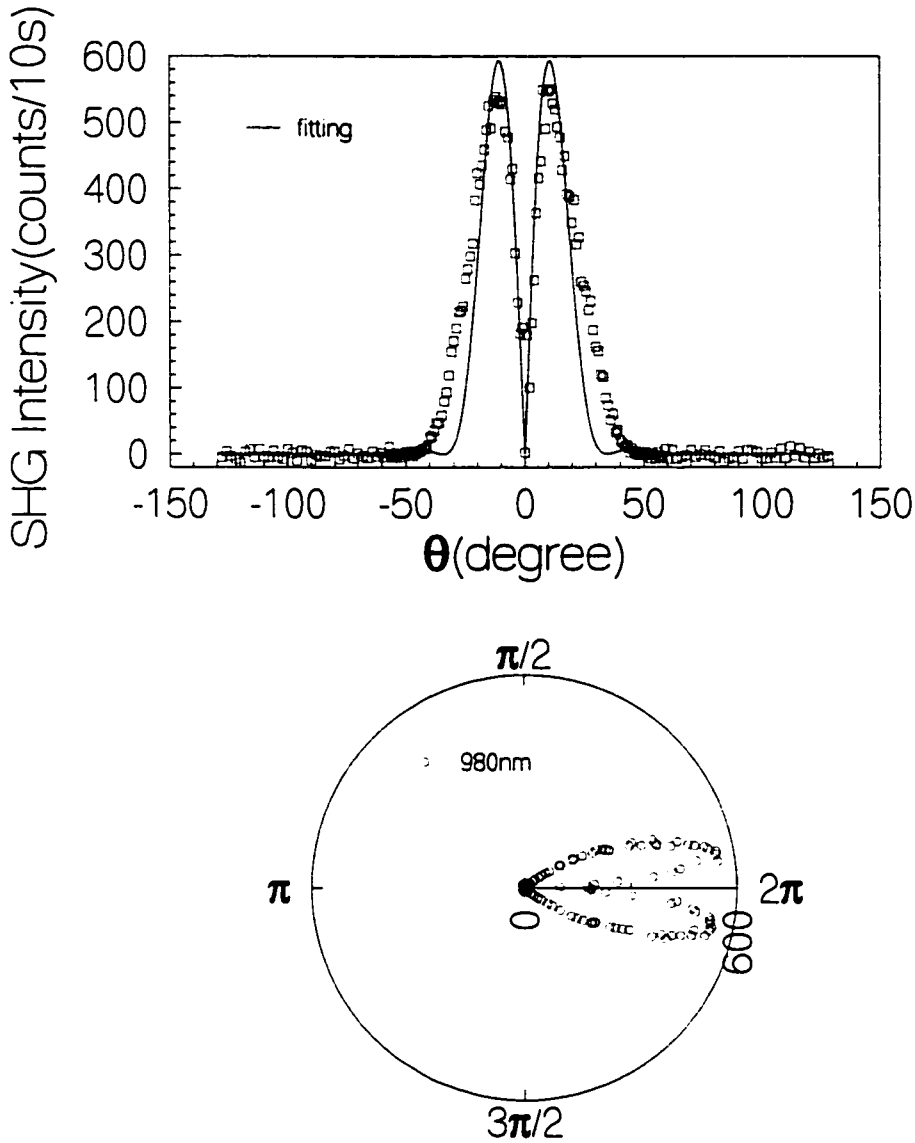

Figure 5.18: SHG scattering from colloidal suspension. Top: x-y plot, Bottom: polar plot. The particle is 980nm in diameter. The polarization configuration is s-in/p-out. Solid line is fitting to RGD model.

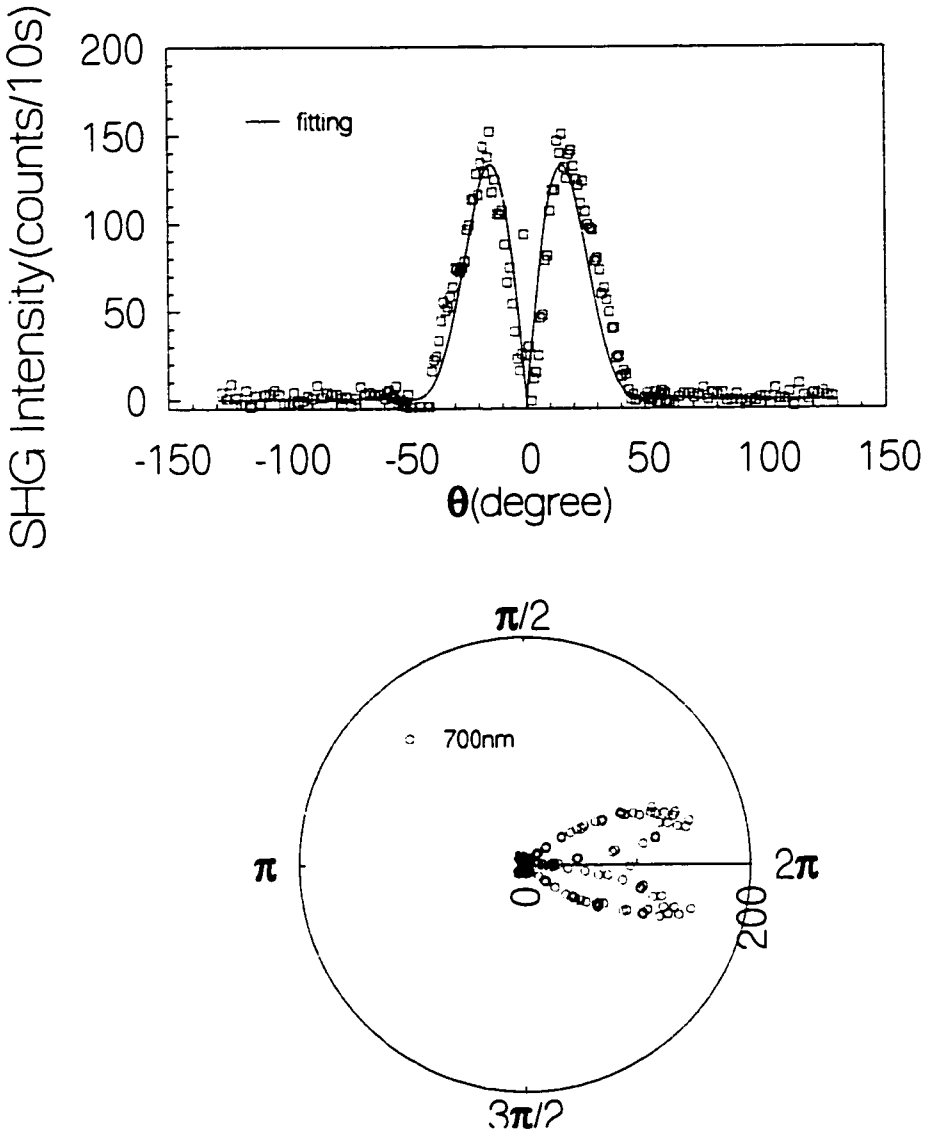

Figure 5.19: SHG scattering from colloidal suspension. Top: x-y plot. Bottom: polar plot. The particle is 700nm in diameter. The polarization configuration is s-in/p-out. Solid line is fitting to RGD model.

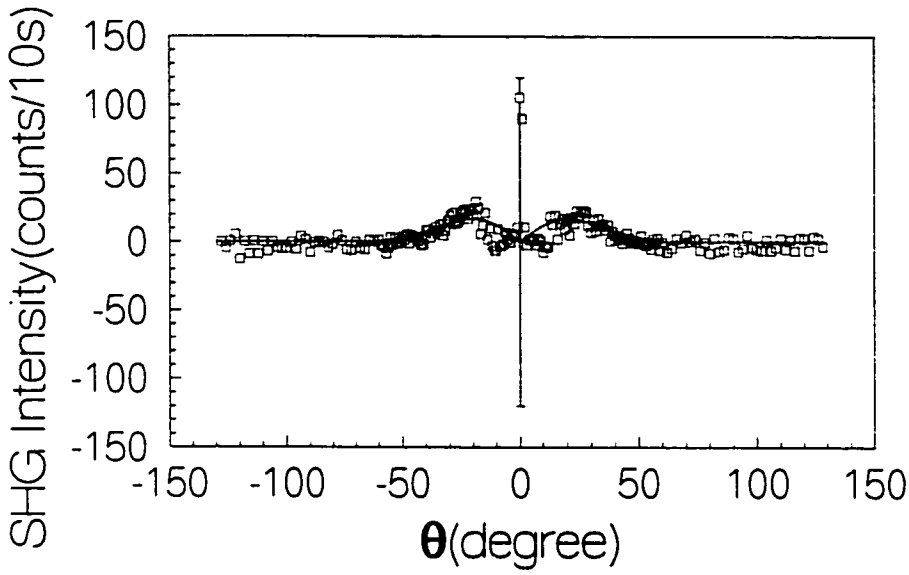

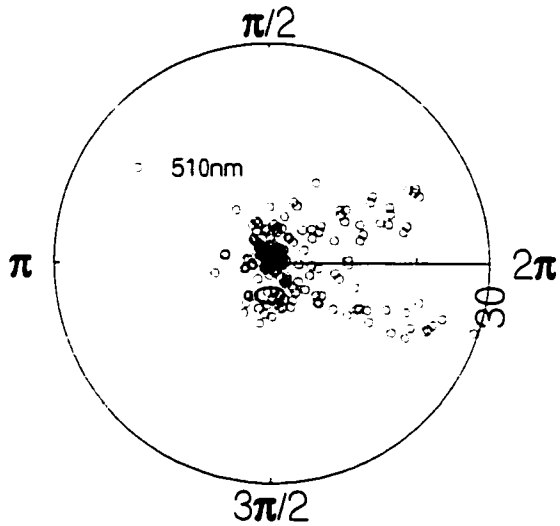

Figure 5.20: SHG scattering from colloidal suspension. Top: x-y plot. Bottom: polar plot. The particle is 510nm in diameter. The polarization configuration is s-in/p-out. Solid line is fitting to RGD model. Also shown is the error bar at forward scattering. At this position, the error bar is the biggest. When angle increases, the error bar drops immediately and significantly

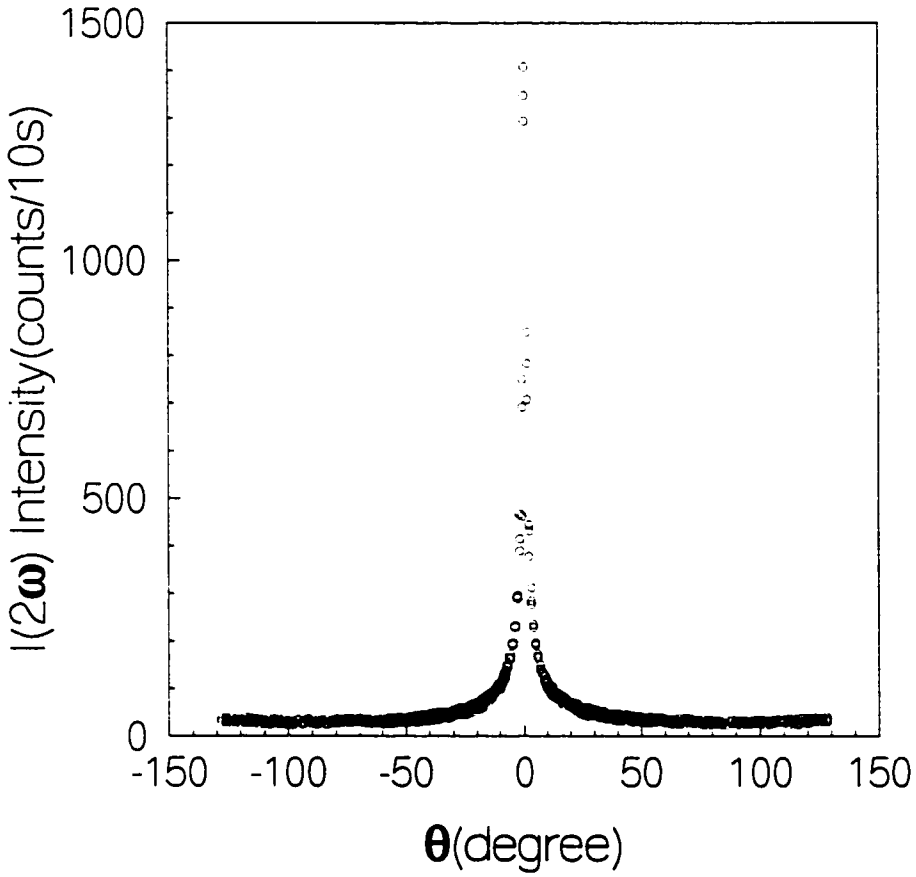

Figure 5.21: Raw measurement for SHG scattering from colloidal suspension. The particle is 980nm in diameter. The polarization configuration is p-in/s-out.

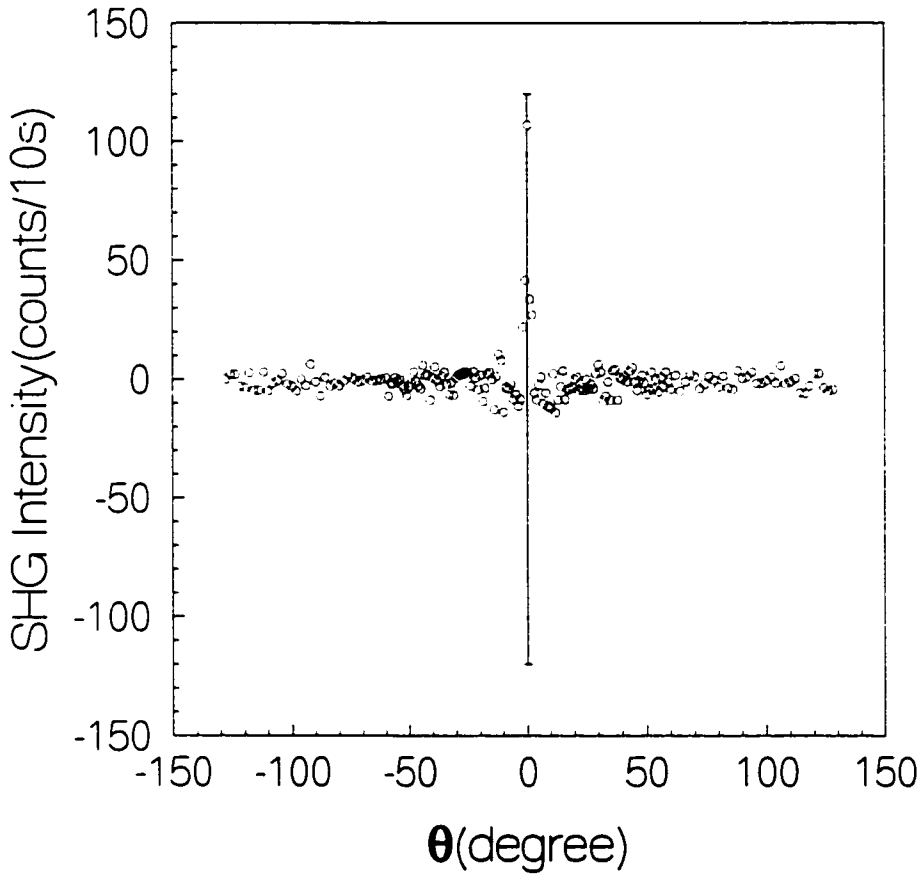

Figure 5.22: Extracted signal for SHG scattering from colloidal particle. The particle is 980nm in diameter. The polarization configuration is p-in/s-out. Also shown is the error bar at forward scattering. At this position, the error bar is the biggest. When angle increases, the error bar drops immediately and significantly. The basically flat feature is typical of s-polarized SHG radiation.

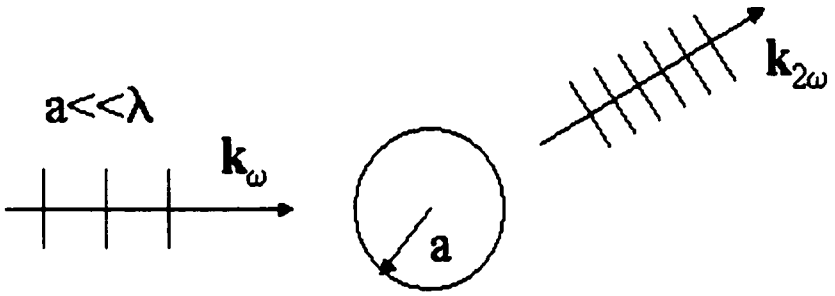

(a)

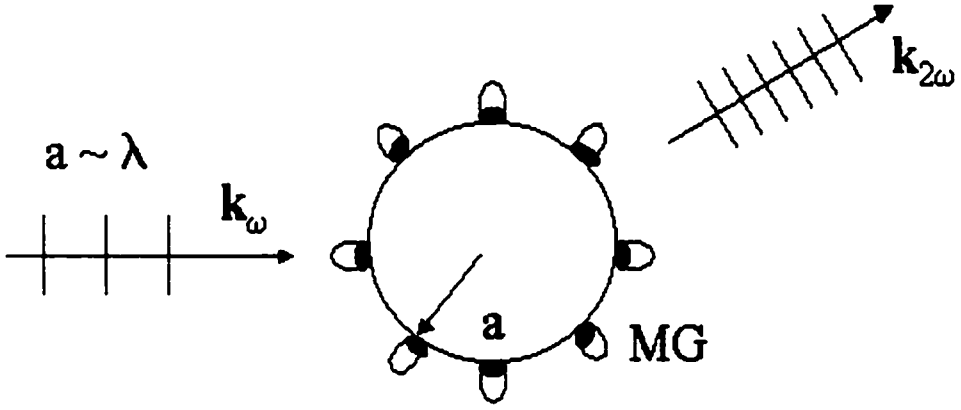

(b)

Figure 5.23: Schematic view of SH Rayleigh scattering model and our model. (a) SH Rayleigh scattering. The particle size is much smaller than wavelength. Particle has no surface nonlinear source coverage. (b) SH light scattering of our model. Particle size is comparable with the wavelength. There is surface nonlinear source coverage.

Chapter 6

SHG Microscopy of Single Micron-size Particle On a Substrate

In this chapter, we discuss the SHG microscope we developed. We discuss the experimental setup we use to detect SHG from single particles and our measurements on three different particles and various sizes.

The linear optical properties of micron-size spherical particles have been understood for many years [1, 2] and currently provide the basis for characterization of a wide variety of particle dispersions ranging from colloids and emulsions to cells. More recently, the nonlinear optical and lasing properties of spheres have commanded attention [91]. The spherical shape of particle affects the local field in two ways. First, particle can act as a lens (to some degree, depending on particle diameter). Input beam rays are refracted by its spherical boundary. This effect can create a strong field locally inside particle, or somewhere outside (but close)to the particle. Second, the particle can act as a cavity. If incident beam parameter matches the particle properties (size, refractive index, etc), then the laser beam will excite resonances inside the

particle. The result is that the elastic scattering spectrum at a fixed observation angle exhibits peaks at specific wavelengths. These effects have been called Morphology Dependent Resonances (MDRs) or "Whispering Gallery Modes" in some literature [92, 93, 94].

Both the focusing effect and the MDRs can introduce interesting nonlinear optical effects unique to particles. Lasing from particles has been observed [95, 96]. Nonlinear optical effects such as phase-modulation [97], Sum-Frequency Generation [98, 99], Stimulated Brillouin Scattering [100] and Raman Scattering [101, 102, 103, 104] were all observed. As far as theoretical aspects, the MDRs and lasing cavities in microspheres were calculated by various groups [105, 106, 107, 108]. The electrical field distribution inside a particle was also calculated to show the spatially enhanced local field [109, 110, 111, 112]. All these studies demonstrate the novel effects associated with the particles.

In this chapter, we report observations of SHG from single micron-size particle and we will discuss the observations accordingly.

6.1 SHG Microscopy for Single Particle: Apparatus

The scanning SHG microscope we built is shown in Fig. 6.1 [113, 114]. A mode-locked Ti:Al_2O_3 laser (see section 3.2) generates a 76Mhz train of ultrashort light pulses (pulsewidth ~100fs) and the laser beam was directed to an optical microscope

objective. The objective focuses the laser beam to a very tight spot on the sample. The sample sits on the xyz translational stages. The translation stages are controlled automatically by 3 stepper motors so that this setup is capable of allowing us to carry out the 3 dimensional scans. The highly focused beam induced the emission of SH photons from the sample, this signal was in the meantime reflected back and collected by the same objective.

A beamsplitter (BS1 in Fig. 6.1) transmits the fundamental 840nm light and reflects the 420nm SH photons into detection path to be filtered and picked up by the Monochromator and PMT and then collected by the single photon counter. One part of the incident fundamental beam is directed into an autocorrelator (section 3.8) which monitors the pulse width for each experiment. The chopper is used to chop the fundamental beam to provide the trigger signal for our photon counter. The CCD and monitor arm is used to monitor the initial optical alignment for expeditious sample registration. The corresponding beamsplitter (BS2 in Fig. 6.1) in CCD and monitor arm is mounted on a rack which is movable and is only used during the sample initial alignment and is moved after the sample registration is done. The fundamental beam passes through a long pass filter F1 in order to filter out SHG noise from the light source before being sent to the objective. The reflected SHG signal is then passed through two BG39 short pass filters to effectively block the fundamental beam. The functions of these filters are exactly like that depicted in Fig. 3.1.

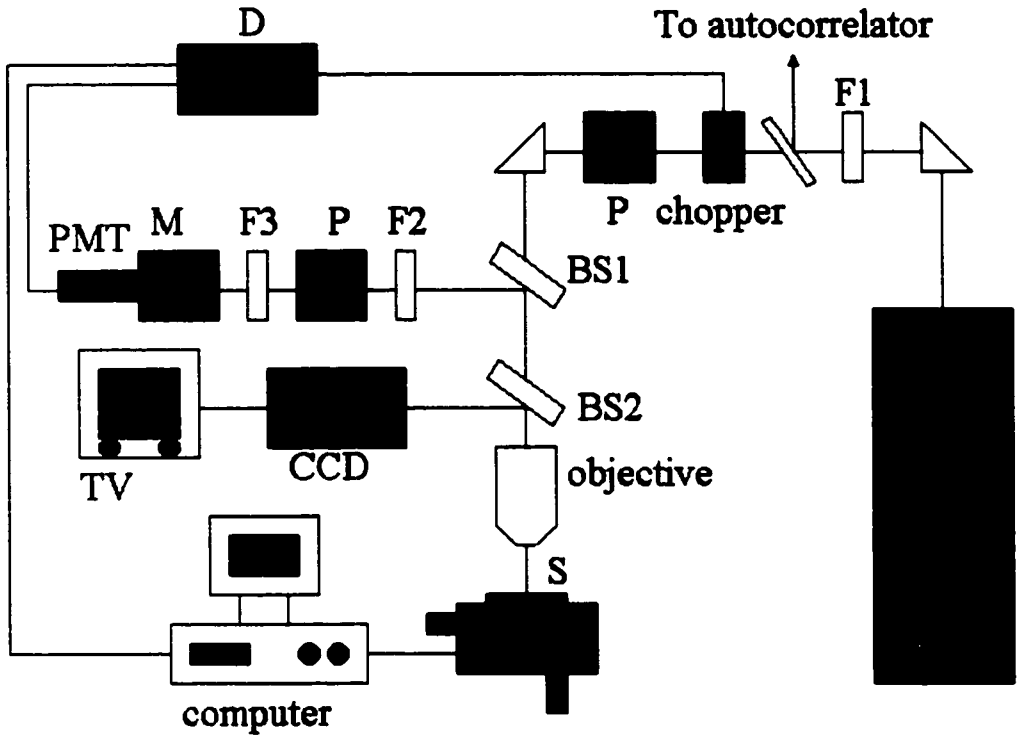

Figure 6.1: Apparatus for SHG microscope. Notations: F:filter; P:polarizer; BS:beamsplitter. BS2 is used for initial alignment only and will be removed when in experiment. D:photon counter; PMT:photomultiplier tube; S:sample; M:monochromator; CCD:camera; TV:monitor.

The motors we used have resolution of 1.8 degree/step, or 200 steps/cycle. The corresponding micrometer has a resolution of 0.5mm/cycle. This gives a spatial resolution of $2.5\mu m$. We operate the motor in half-step mode, therefore our apparatus has a final spatial resolution of $1.5\mu m$. All the data-taking and motor-control are automatically done through the computer in which we implement a QuickBasic code to do the job [51].

The beam focus spot size is a very important parameter. It determines the light intensity on the sample. We carefully measured this parameter and for our experimental air objective, the numerical aperture (N.A.) of 0.85, the focus spot size was $1.8\mu m$ in diameter. Here diameter is defined as the full-width at e^{-2} of the intensity maximum, I_{max} (see chapter 7).

6.2 Synchronous Photon Counting

The monochromator and PMT have been described in chapter 3. We also described the photon counter briefly in chapter 3. In this section, we discuss the synchronous photon counting mode we used to collect the signal. In synchronous detection, an optical chopper modulates the fundamental light source. The reference output from the optical chopper acts as the trigger signal for the photon counter. Our photon counter SR400 has two gated counters, A and B. We use both counters in the signal detection. A gate of counter A was positioned to coincide with the open phase of the

chopper, B gate of counter B was delay-adjusted to position to the closed phase of the chopper. Both A and B gates have same width. In the experiment, both A and B counters counted the number of photons N_A and N_B in the gates respectively. The difference between the two gates, $N_A - N_B$ was reported.

The timing between chopper, A gate, and B gate is shown in Fig. 6.2. When timed at this setting, counter A effectively detects the photons when chopper is open, i.e. counter A counts the total number of photons including both signal plus the background noise. Counter B, on the other hand, only counts the number of photons when chopper is closed. Thus counter B only counts the background noise photons. By subtracting N_B from N_A, we effectively subtract background noise from our measurement. This synchronous photon counting mode is especially useful in noisy environment or when the signal count rate is very low. For SHG from single particle, the signal rate has only several tens of counts per second in the quadratic region, it is therefore very important to use synchronous photon counting mode to account for uncontrolled variation in background noise. Also, in all the experiments, we cover the whole setup with a black cloth and block scattered light as much as possible. The data-taking are all in dark room. Our apparatus thus built has a background noise about 1 count per second.

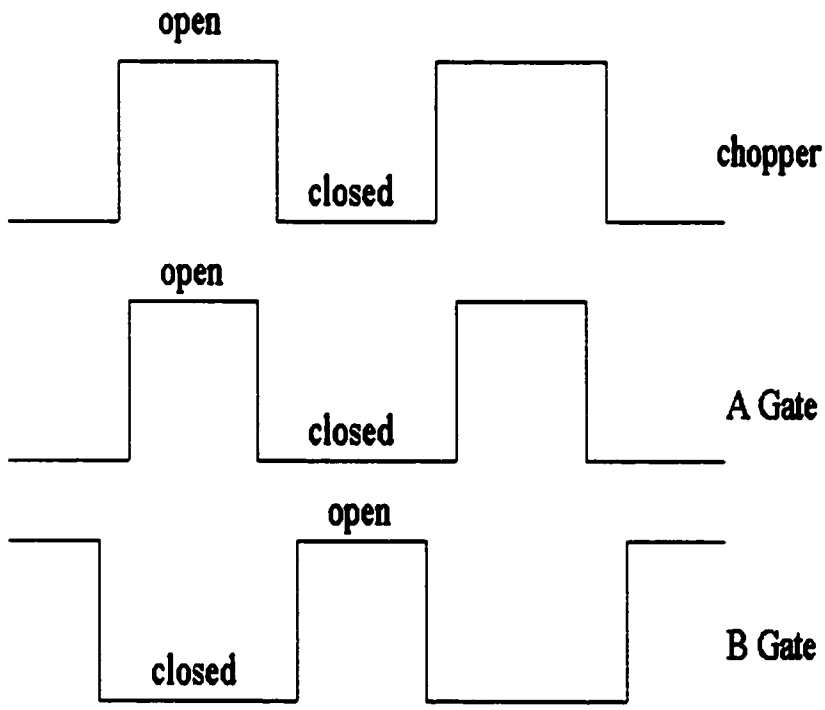

Figure 6.2: The timing relationship between chopper and photoncounter gates. A gate corresponds to chopper open state, B gate corresponds to chopper close state.

6.3 Sample Registering

Sample registering is a very important issue. A poorly aligned system will usually fail to scan the desired sample region and therefore will usually obtain false information. In our system, we use a specially manufactured sample mask for ease of sample registering. The sample mask is shown in Fig. 6.3(a). A thin metal film is etched out of an area of $25\mu m \times 25\ \mu m$ shown as in the white square in Fig. 6.3(a). This exposed part is a glass substrate. We drop-coated this mask with an extremely dilute particle water solution. A typical sample as-deposited is shown in Fig. 6.3(a) where the dark spot is a $2.19\mu m$ diameter Polystyrene microparticle. To correctly align our microscope objective and scan over the area with the particle, we first use a small N.A. objective such as N.A. = 0.40, 20X objective. Through the monitoring CCD camera and TV screen, it is usually easy to locate this $25\mu m \times 25\mu m$ area. After this, we change the objective to our experimental objective, the N.A. = 0.85, 60X objective and after some fine alignment, we are able to exactly scan the region we want. We show one typical SHG scan as a function of laser spot on the sample in Fig. 6.3(b). The $12\mu m \times\ 12\mu m$ scanning region corresponds to the outlined square in Fig. 6.3(a). The laser beam intensity is $\sim$7.5 GW/cm^2 for this scan. A sharp peak at the particle position is $\sim 10^3$ times larger than the signal from the glass substrate under these illumination conditions. This enormous enhancement suggests that the technique may have applications in the context of nonlinear optical microscopy.

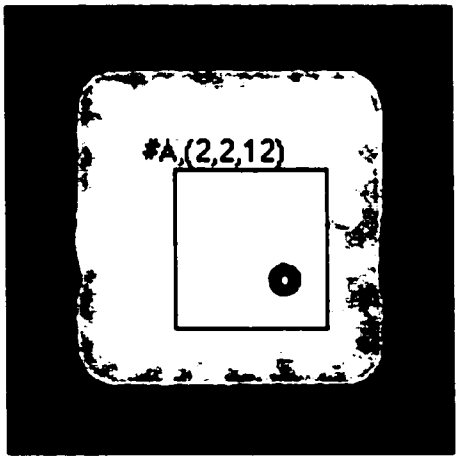

(a)

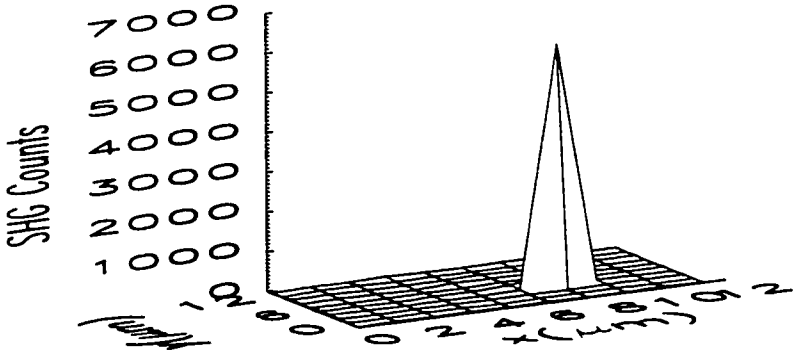

(b)

Figure 6.3: (a) Sample mask used for SHG microscope. The $25mum\times$ $25\mu m$ white area is the glass substrate which is surrounded by metal (the surrounding black image). The dark spot is a $2.19\mu m$ PS particle. The outlined square region corresponds to the SHG scanning region in (b). (b) SHG scan versus function of laser spot on sample of (a). The sharp peak corresponds to particle position. The integration time is 5 seconds.

In this experiment, we use three kinds of particle samples: polystyrene (PS), PolyMethylMethAcrylate (PMMA) and silica. The size of the particles ranged from 1.1 μm to $4.3\mu m$.

6.4 SHG From Single Micron-size Particle

We measured the SHG from single micron-size particle versus the input laser peak power intensity. In Fig. 6.4 we show the result on a log-log graph for polystyrene particles of diameter of $1.1\mu m, 2.2\mu m$ and $4.3\mu m$. This is the major and most interesting observation of our experiment. The data divide naturally into three regimes. At low peak intensity all particles respond quadratically as is expected from the general SH Generation theory. Then, as the input peak intensity is increased, a threshold is reached. At this point, the SH signals increase exponentially and finally saturate. The measurements were reversible up to and even slightly beyond the saturation point (e.g. $\sim 8GW/cm^3$). Permanent bead damage is found to occur at higher peak powers. This detection of SHG from a single micron-size particle has never been reported before. Also, the exponential increase of signal was never reported before. It is an interesting observation. In Fig. 6.4, the solid lines are quadratic fitting. The fitted slopes are 1.83, 1.90 and 2.18 for $1.1\mu m$, $2.2\mu m$ and $4.3\mu m$ respectively. These ~ 2 slopes agree with the expected quadratic response.

In Fig. 6.5 and Fig. 6.6 we show the similar measurements performed on PMMA

and silica (SiO_2) particles respectively. Notice that signal saturation was observed for all particles, but exponential signal variation was not exhibited by the smaller spheres, i.e. by the $1.1\mu m$ ($1.4\mu m$) diameter PMMA (silica) particles. The exponential increase was observed for PMMA particle of $3.1\mu m$ and $4.3\mu m$, for silica bead of $3.5\mu m$.

6.5 Discussion

As we discussed in chapter 2, it is very difficult to attempt a rigorous quantitative theoretical analysis on the SHG measurements from single particle. The difficulty arises due to the fact that it is not easy to accurately characterize the focused laser beam and it is not obviously clear how the single particle will respond to the high intensity excitation. Furthermore, the invalidity of plane wave approximation and the failure of paraxial approximation make calculation of the true electric field distribution even more complicated. Therefore, in this section, we will crudely parameterize our observations so that certain general features are made evident.

We first consider the results in the low input intensity region. We adopted a very simple model for our analysis. We fit the data assuming:

$$I(2\omega_0) \propto |\chi^{(2)}_{eff}|^2 [I(\omega_0)]^m \tag{6.1}$$

Here $I(2\omega_0)$ is the SHG intensity, and $I(\omega_0)$ is the intensity of the input beam. We allow for the possibility that the exponent, m, can differ from 2 in our fits. $\chi^{(2)}_{eff}$

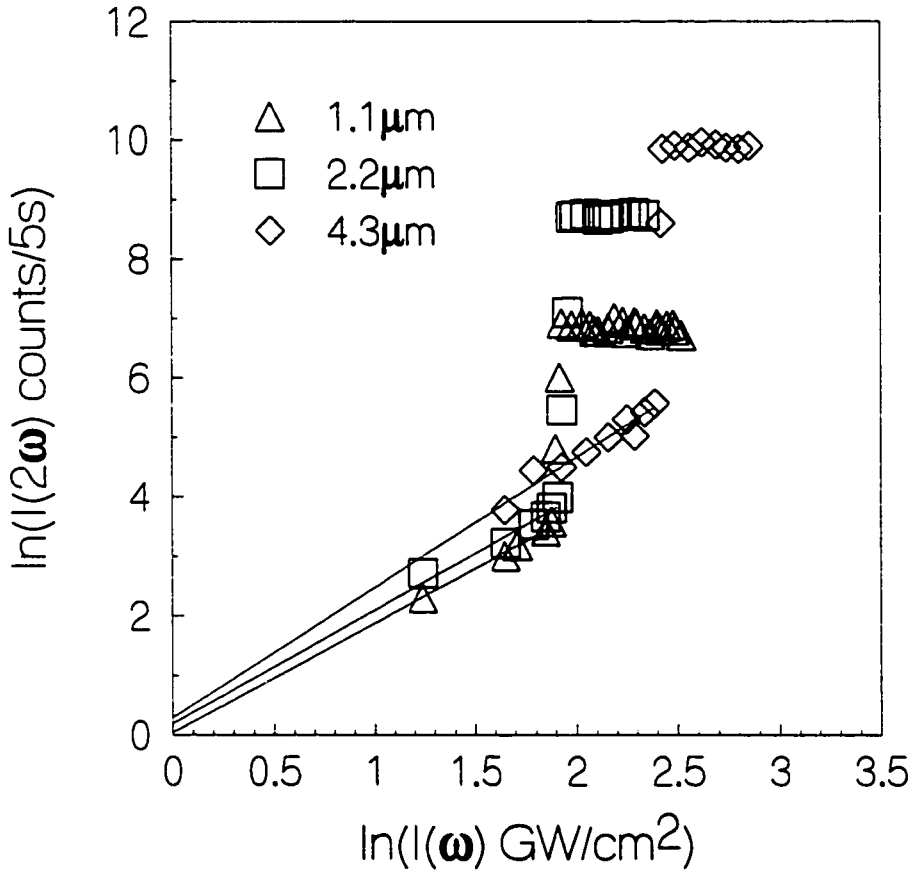

Figure 6.4: SHG from PS beads versus input peak intensity for three different sized particles. The solid lines are quadratic fits. The coefficients for $1.1\mu m$, $2.2\mu m$ and $4.3\mu m$ are 1.83, 1.90 and 2.18 respectively.

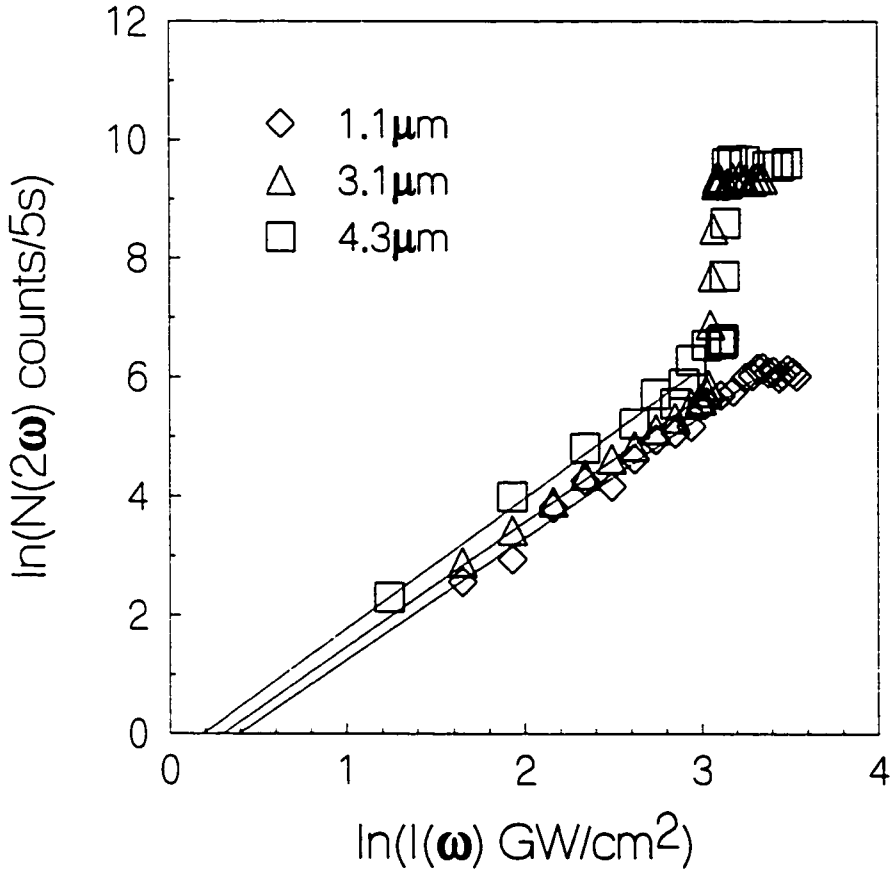

Figure 6.5: SHG from PMMA beads versus input peak intensity for three different sized particles. The solid lines are quadratic fittings. The coefficients for $1.1\mu m$, $3.1\mu m$ and $4.3\mu m$ are 2.05, 2.10 and 2.19 respectively.

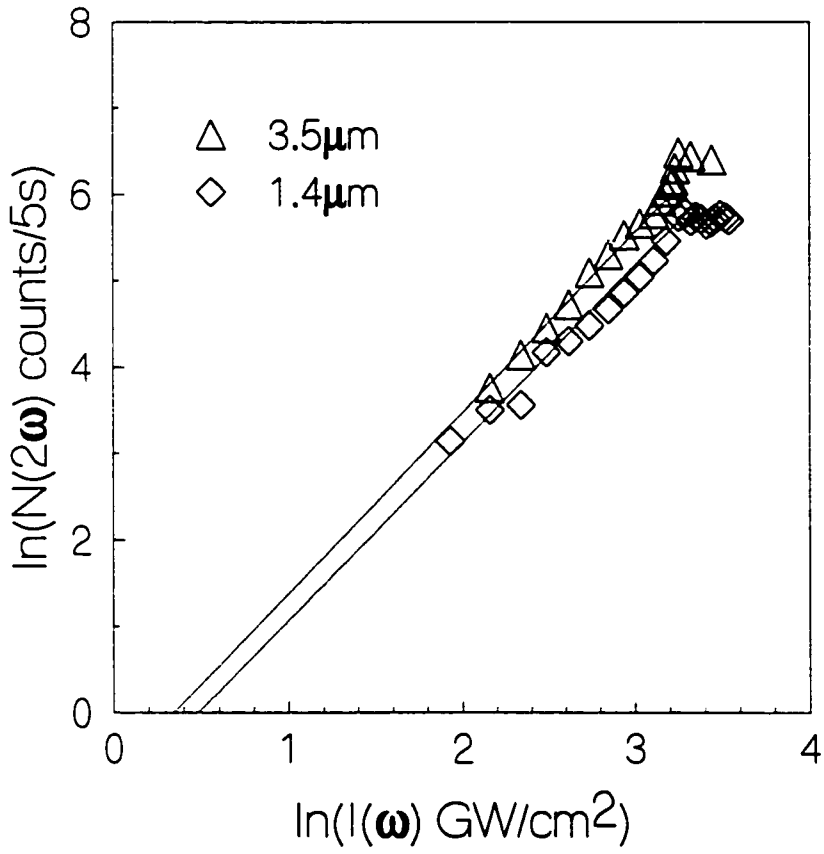

Figure 6.6: SHG from silica beads versus input peak intensity for two different sized particles. The solid lines are quadratic fittings. The coefficients for $1.4\mu m$ and $3.5\mu m$ are 2.05 and 2.09 respectively.

is an effective second-order nonlinear susceptibility of the particle. Generally, $\chi^{(2)}_{eff}$ will depend in a complicated way on particle optical properties and size, on input beam excitation geometry, and on excitation and emission wavelengths. We assume the effective susceptibility depends on the product of three factors: (1) An intrinsic material-dependent second order susceptibility $\alpha^{(2)}_j (j = PS, PMMA, SiO_2)$. (2) An effective light excitation overlap area, S, equal to the particle diameter divided by the excitation beam diameter, and (3) a complex geometrical/Fresnel factor, G_{jkl}(j= PS, PMMA, SiO_2; k= particle diameter, l=light beam geometry), which depends on light beam and sample geometry, and particle properties. We have written G with three subscripts to emphasize that G will depend on many factors, for example, the particle dielectric constant and size, light polarization, the particle cavity modes that are excited by the input beam, the excitation geometry, and the collection angle (see for example reference [38]).

The solid lines in Figure 6.4, Figure 6.5, and Figure 6.6 represent our best fits to the low intensity data. From these lines we deduce m, and $\chi^{(2)}_{eff}$ for particles of different size and type. The results for each particle type and size are given in Table 6.1. We see that m $\approx$ 2 in all cases. The measurements did not enable us to distinguish the contributions of the surface dipole and bulk quadrupole moments.

From Table 6.1 we see that the effective nonlinear susceptibility, $\chi^{(2)}_{eff}$, depends on particle type, but not so much on particle size. For example for $\sim 1\mu m$ diameter

Table 6.1: Fitting parameters for quadratic region

type	diameter(μm)	m	$\lvert\chi^{(2)}_{eff}\rvert^2$	$G/G_{silica,3.5}$
PS	1.1	1.83±0.12	1.05±0.08	2.40±0.17
	2.2	1.90±0.23	1.22±0.34	1.58±0.24
	4.3	2.18±0.21	1.35±0.58	1.66±0.37
PMMA	1.1	2.05±0.06	0.45±0.07	1.57±0.16
	3.1	2.10±0.03	0.53±0.04	1.04±0.08
	4.3	2.19±0.09	0.66±0.17	1.16±0.17
silica	1.4	2.05±0.08	0.38±0.09	1.13±0.15
	3.5	2.09±0.04	0.49±0.06	1±

particles, $\chi^{(2)}_{eff,PS} \sim (1.5\pm0.1)\chi^{(2)}_{eff,PMMA} \sim (1.6\pm0.2)\chi^{(2)}_{eff,SiO_2}$. Since S is the same for the same size particles, these differences may be a result of different intrinsic material nonlinearities (i.e. $\alpha^{(2)}_j$), or may be due to different local electric field strengths within each particle (i.e. via G). Our separate linear optical measurements at the same wavelengths (see chapter 7) give the index of refraction for these 3 particles at 1.57, 1.47 and 1.44 respectively. Using these refractive index values, our Mie calculations (Appendix F) show that at this size, PS has only about a 10% stronger local electric field than PMMA and Silica under plane wave excitation, while PMMA and silica has roughly the same local electric field. The differences in $\chi^{(2)}_{eff}$ are therefore probably due to intrinsic material nonlinearities. In last column of Table 6.1, We calculate the relative G value (relative to silica of $3.5\mu m$) after normalizing the effective illumination area. That is, we account for the fact that some particles are smaller than the excitation beam, others are larger than the excitation beam. For smaller particles, the effective illumination area particle experiences is different from the excitation beam size. For larger particle, even though all the excitation energy "hits" the particle, the effective illumination area is smaller than particle size. Therefore, we normalized for the effective area of excitation (i.e. S). For particles that are larger than excitation beam size, we take S=1. Otherwise, we take S as the ratio of particle size to excitation beam size. After carrying this procedure through, we get the values as shown in Table 6.1. From there, we can examine the effect of different particle sizes. For example, we

find $G_{1.1\mu m,PS} : G_{2.2\mu m,PS} : G_{4.3\mu m,PS} = (1.5 \pm 0.3) : 1 : (1.1 \pm 0.3)$. These differences in G are not significant given the measurement error.

We next consider the dramatic nonlinear enhancement occurring at higher input light intensities (e.g. $\sim 7.0GW/cm^2$ for $2.2\mu m$-diameter PS particles). This effect is seen clearly for all our PS particles, and for the two larger PMMA particles. There is also a hint of the effect in the large silica particle data. In Figure 6.7 we exhibit the PS data in this regime on a semi-log plot. The linear variation of the SH signal on this plot with respect to input intensity suggests that the enhancement is exponential in the threshold region, i.e.

$$I(2\omega_0) = Ae^{\alpha I(\omega_0)} \tag{6.2}$$

In Table 6.2 the values of lnA and α are given for the PS and PMMA particles exhibiting the effect. The silica particle data was too noisy to be analyzed meaningfully. Although there is a large scatter in the value of A, the exponential gain coefficient, α, is clearly material-dependent. It also appears that the threshold for turn-on of the nonlinear enhancements is material dependent and size-dependent.

The microscopic origin of these exponential enhancements is not readily apparent from the measurements. These exponential enhancements may involve higher-order nonlinear processes. As we know, the SHG intensity can generally be expressed as

$$I(2\omega_0) \propto E^2(\omega_0)$$

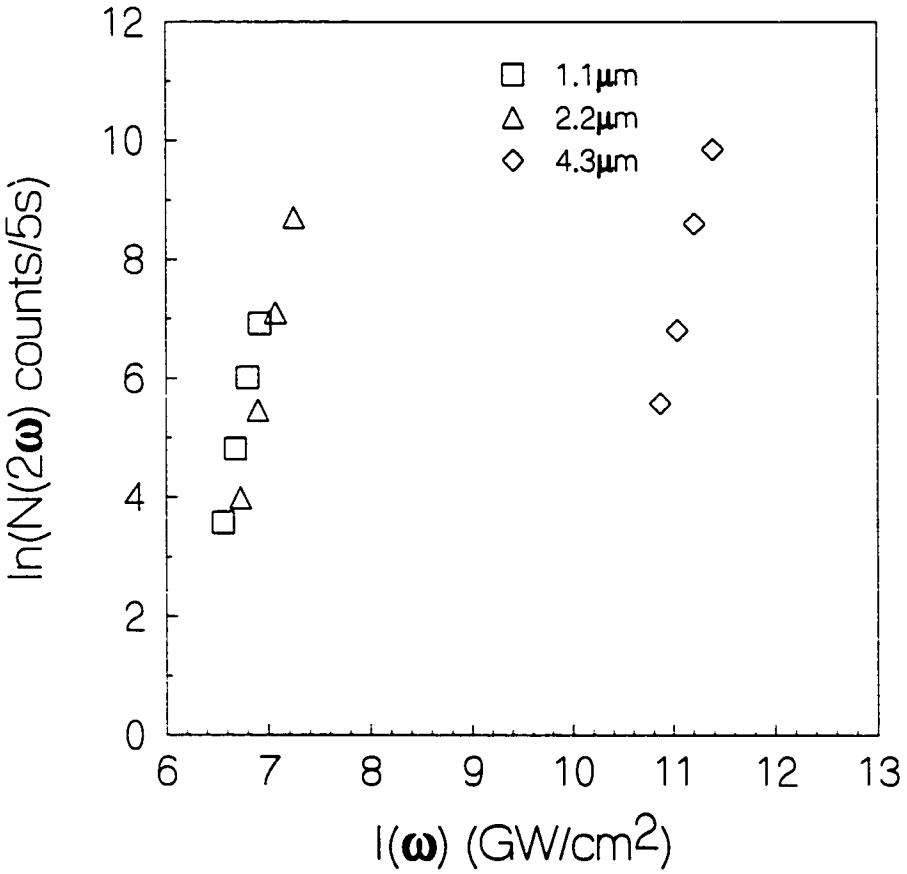

Figure 6.7: $ln(I_{SHG}^{2\omega_0})$ Vs. I^{ω_0} for PS beads showing the exponential growth of SHG signal during transition region.

Table 6.2: Fitting Parameters for Transition Region

type	diameter(μm)	lnA	α
PS	1.1	-57.69±21.35	9.35±3.17
	2.2	-57.50±21.35	9.13±3.16
	4.3	-86.40±24.45	8.46±2.20
PMMA	3.1	-96.40±33.43	4.86±1.56
	4.3	-121.92±50.31	5.65±2.18

while the electric field can be written as

$$E(\omega_0) \propto e^{i(kz-\omega_0 t)}$$

if some higher-order process occurs (such as self-focusing), then we can write

$$n(\omega_0) = n_0(\omega_0) + n_2 I(\omega_0)$$

or

$$k = k^0 + \Delta n \frac{\omega_0}{c}$$

here $\Delta n = n_2 I$, n_2 is the nonlinear index of refraction. From reference [52], we know that $n_2 \propto \frac{1}{n_0^2}\chi^{(3)}$, if we substitute into above expression, we finally arrive

$$I(2\omega_0) \propto e^{CI(\omega_0)} \tag{6.3}$$

while C is constant and is related to the third-order nonlinear optical susceptibility

as

$$C \propto Im(\chi^{(3)}) \tag{6.4}$$

This provides one possible explanation of our observation of the exponential increase of the SHG signal. It suggests that higher order nonlinear processes are involved, and the exponential growth coefficient is proportional to the imaginary part of third-order nonlinear susceptibility.

The fact that these enhancements occur near the damage threshold of the particles suggests that large local fields at the fundamental wavelength arise in the particles and induce multi-photon ionization processes (e.g. presumably through particle cavity modes and possibly third-order nonlinear optical effects). These multi-photon ionization processes, in turn, can dramatically alter the linear and nonlinear properties of the particles. Further work remains to clarify these issues.

To conclude, we have reported on SHG microscopy of single, micron-sized particles in air. Three particle types and several particle sizes were employed. Quadratic and exponential responses were observed, depending on input light intensity. We have parameterized the data with a simple model, and have suggested a possible cause of the exponential enhancement. The measurements provide a new benchmark about signal size and experimental conditions in single particle SHG experiments. With continued improvements in theory, it should be possible to understand these data more quantitatively.

Chapter 7

Linear Optical Measurements

In this chapter, we discuss two background linear optical measurements that we performed to obtain particle index of refraction, and the microscope objective focus spot size at the optical wavelength we used.

7.1 Measurements of Particle Index of Refraction

In this section, we discuss the linear optical light scattering we used to measure the index of refraction of particle.

Refractive indices of particles are very important in both linear and nonlinear light scattering. For example, in linear dynamic light scattering, people often use the information about refractive index of particle plus others to derive other information such as particle size, particle polydispersity, and even particle shape. To accurately obtain this particle information, the refractive index information has to be precise.

In the nonlinear optical case, we use ultrashort light pulses whose impact on index of refraction is unclear. Moreover, we generally only have index of refraction numbers

for our particles obtained through the bulk material instead of the micron-size particle. The known index of refraction value is also usually for visible region instead of our 840nm near infrared. Furthermore, it is well known that index of refraction value plays important role in determining the possible Morphology Dependent Resonance (MDRs) in the particle [92, 93]. We therefore performed our own linear measurements to determine the index of refraction value for the particles we used.

The idea in our linear optical experiment is that we measure the linear optical light scattering form factor from the same colloidal sample using 840nm fundamental light and then compare the form factor with Mie theory to derive the particle index of refraction. Although Mie theory is a rigorous theoretical solution, it is not an easy job to fit the particle index of refraction using Mie theory from the form factor measurements owing to the analytical complexity of Mie theory. Therefore, in this section, instead of fitting the index of refraction from Mie theory, we calculate the chi-square and identify the index of refraction with the least chi-square.

The experimental setup we used is shown in Fig. 7.1. Using an optical fiber, we couple our Ti:Al_2O_3 laser of 840nm to a dynamic light scattering apparatus. We collimate the laser beam immediately after the exit of fiber and pass it through a $\frac{\lambda}{2}$ waveplate before passing through a s-polarizer and being focused into the sample. The waveplate is used to convert the input laser beam to s-polarized. The scattering light from sample is picked up by a Brookhaven Instruments corporation dynamic

light scattering detection arm which comprises of a series of slits and filters and one PMT whose output is sent to model BI-2030AT correlator analyzer and analyzed by computer. Sample is sitting at the center of goniometer model BI-160. The whole dynamic light scattering apparatus is already well-aligned in daily operations and every time before the experiment, we check our sample particle size using the dynamic light scattering method. The particle size and particle polydispersity results from dynamic light scattering analysis agree well with our sample's nominal specifications, thus ensure that our sample is good and the apparatus alignment is good.

A typical linear light scattering form factor measurement is shown in Fig. 7.2 for a polystyrene particle of diameter of $1.1\mu m$. From the measurements, we normalize all the data to $\theta = 10^0$ value which is the smallest angle we measured. Then we do Mie calculations (Appendix F) of the form factor using a series of index of refraction values. The Mie-calculated data points are also normalized to $\theta = 10^0$ point. We then compared these two normalized data sets and calculate the chi-square defined as following

$$\chi^2 \equiv (\sum_i (x_i - x_{0i})^2) \times 100$$

where coefficient 100 is introduced for the convenience of presenting the χ^2 values. x_i is the measurement data points for our sample, x_{0i} is the Mie calculation points. By using a series of index refraction values in Mie theory, we obtain a series of χ^2 values. We identify the least χ^2 with the index of refraction of our particle. We present the

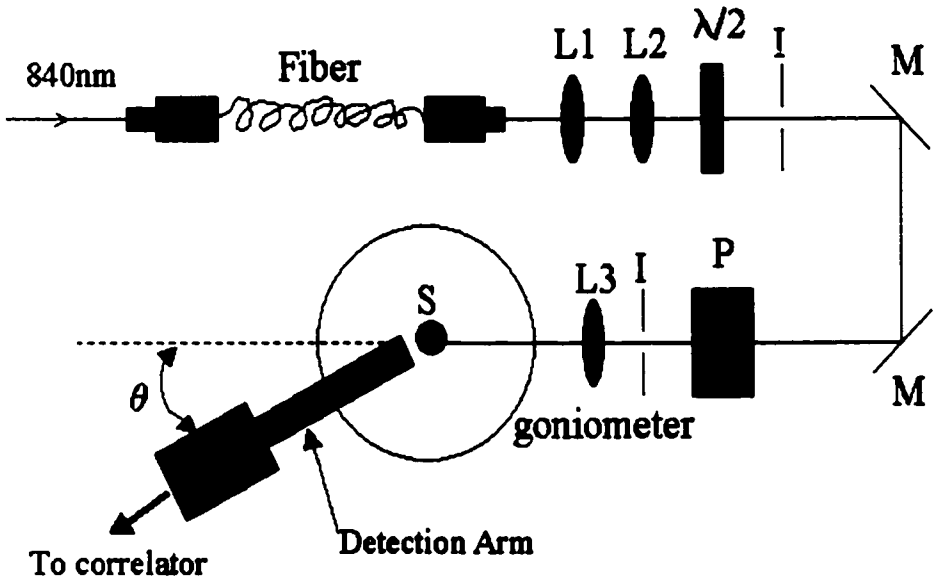

Figure 7.1: Experimental setup for linear light scattering form factor measurement. Notations: L:lens, $\lambda/2$:waveplate, I:iris, M:mirror, P:polarizer, S:sample

Table 7.1: χ^2 Values For Our Polystyrene Particles

n	1.55	1.56	1.57	1.58	1.59
D=1.1μm	1.29684	0.700653	0.408801	0.422152	0.739286
D=2.2μm	0.609971	0.307185	0.109363	0.0853988	0.314437
D=4.3μm	0.6606	0.221915	0.238104	0.272702	0.320533

results for all three polystyrene particles in Table 7.1. Table 7.2 and Table 7.3 are the corresponding χ^2 results for PMMA and silica particles respectively.

From Table 7.1, 7.2, and 7.3, we conclude that at 840nm, the index of refraction for our sample is roughly

$$n_{ps} \sim 1.57$$

$$n_{pmma} \sim 1.47$$

$$n_{silica} \sim 1.44$$

7.2 Measurement of Focus Spot Size of Microscope Objective

The laser spot size characterization is a routine job in optical experiment. Traditionally, one use either a pinhole or a blade to scan through the beam profile and from the measurement to obtain the beam spot size. However, these methods present serious

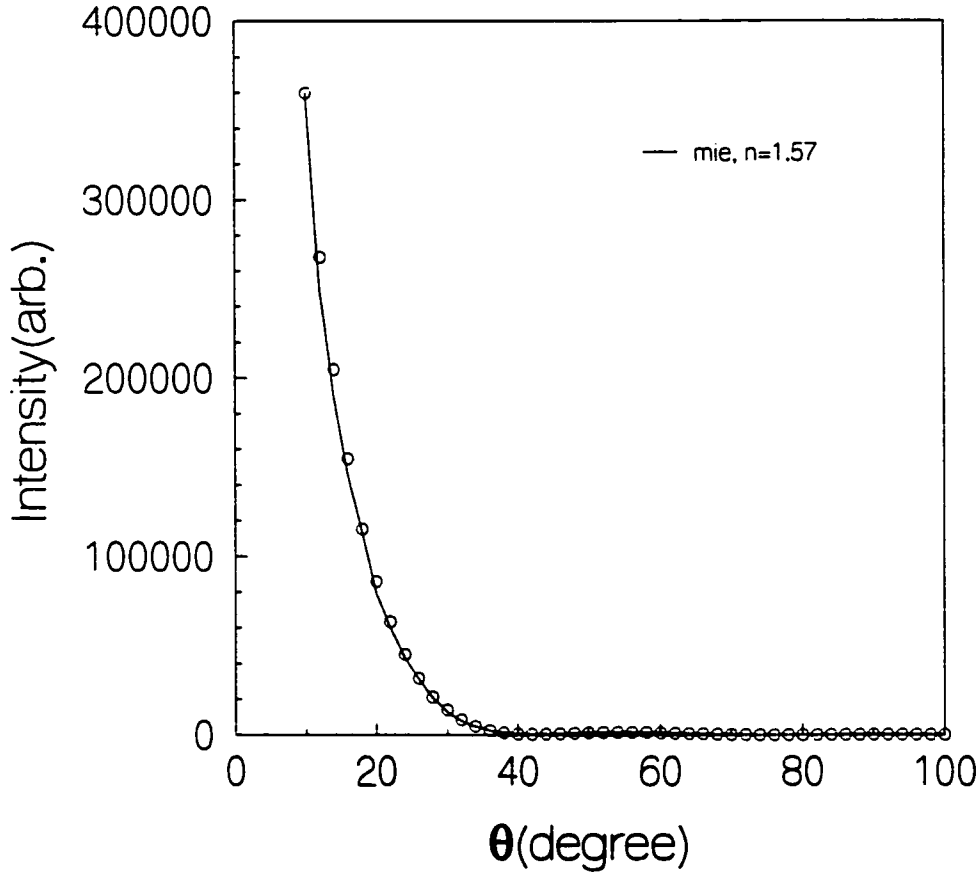

Figure 7.2: Linear light scattering form factor measurement. The sample is PS of D=1.1μm. The solid line is Mie calculation using n=1.57.

Table 7.2: χ^2 Values For Our PMMA Particles

n	1.45	1.46	1.47	1.48	1.49
D=1.1μm	0.874763	0.444429	0.257122	0.321082	0.646658
D=3.1μm	0.190475	0.118105	0.0670016	0.0649116	0.152608
D=4.3μm	0.534391	0.236084	0.0465878	0.175694	0.987166

Table 7.3: χ^2 Values For Our Silica Particles

n	1.41	1.42	1.43	1.44	1.45
D=1.4μm	0.601702	0.264732	0.0740452	0.0230668	0.104306
D=3.5μm	0.118213	0.110682	0.107816	0.107619	0.112649

difficulties when applied to measure the beam spot size from a microscope objective. There are several reasons for this. One, the microscope objective (N.A. = 0.85 in our experiment) focuses the beam to a very tight spot, usually only a couple of microns. To measure the spot size using traditional pinhole method, one needs a pinhole of at most several hundred nanometers to ensure decent accuracy. But such small pinhole is extremely rare. Secondly, if one uses a blade to scan through the spot, one has to be very capable of controlling the movement of blade precisely. This presents a difficult practical challenge. Thirdly, and also most importantly, the microscope ob-

jective focus spot is usually located very close to the objective tip (usually <1mm) and almost there is no way beforehand to know for sure where the focus spot is and therefore, it is very difficult to use the traditional method to scan through it. Even the commercial products for such small spot size measurement are hard to find.

In lieu of these, we developed a very simple, yet very effective and very comfortable method to measure such small spot size indirectly. We present the model in Fig. 7.3. The idea is that instead of measuring the focus spot directly, we measure two different spots (z_1 and z_2 in the figure) which are a little bit far from the objective and are much bigger compared with the pinhole. Therefore, we can be very comfortable in measuring the two spots at z_1 and z_2. After we measure the two spots, we can infer the true focus spot size in a simple way as described below.

In Fig. 7.3, the objective is rigidly mounted on the optical table, the pinhole instead is mounted on a xyz translation stage. We first adjust the x- and y- translational stage to maximize the signal. This way, we make sure pinhole and the focus spot are exactly at the same height and aligned. A high O.D (optical density) neutral density filter was put before the objective to attenuate the laser light to avoid the detector saturation. A photodiode is rigidly attached to the back of pinhole, so all the through light is picked up by the detector. After x- and y- translation stage alignments are done, we don't need to adjust them anymore. Only z-translation stage is needed to adjust.

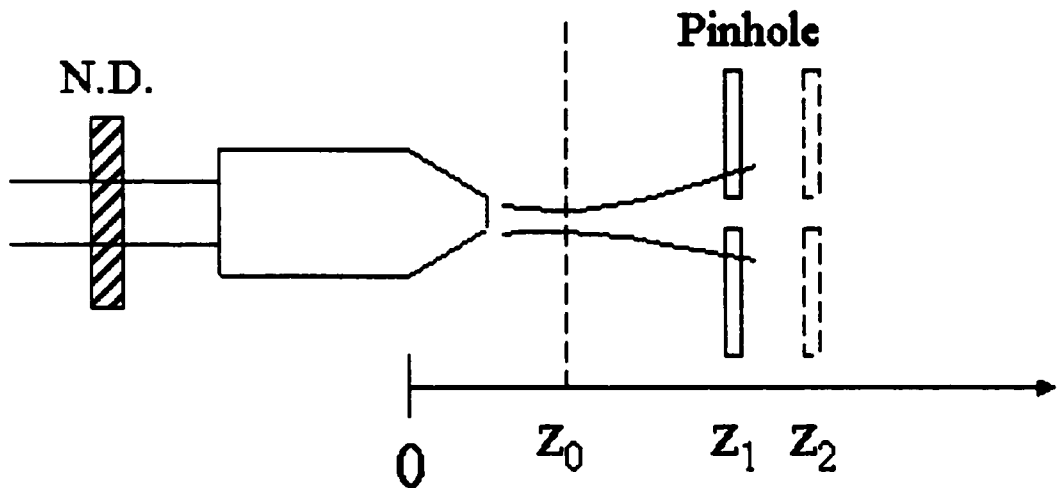

Figure 7.3: Schematic view for the measurement of objective focus spot size. z_0 is the focus spot position, z_1 and z_2 are the two positions we measure beam profiles.

In the following, we only consider z-dimension as variable.

Origin "O" can be chosen arbitrarily. For convenience, we choose "O" at the zero origin of z-micrometer. We assume z_0 is the true focus spot size position. We denote the beam diameter at z_0, z_1, z_2 are $2\omega_0$, $2\omega_1$ and $2\omega_2$ respectively. We draw these quantities in Fig. 7.4 for clarity. We always have the following relationship [115, 116]:

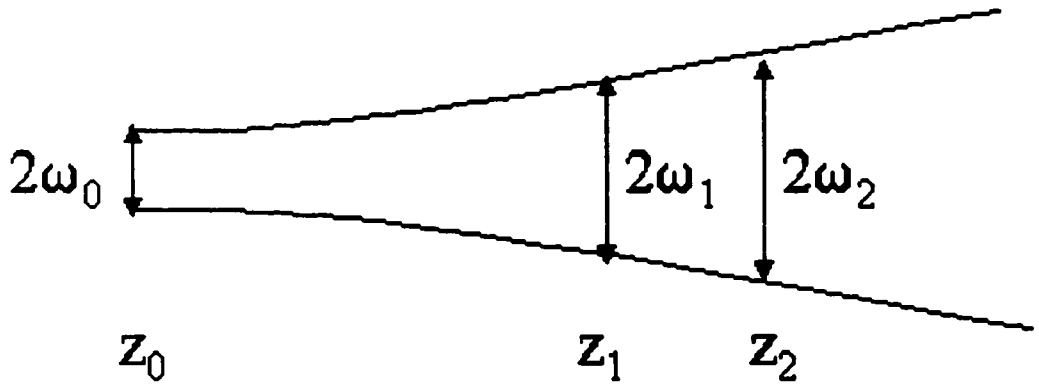

Figure 7.4: Schematic showing the definition of beam diameter at different positions.

$$\omega^2(z - z_0) = \omega_0^2(1 + \frac{(z - z_0)^2}{\xi^2}), \tag{7.1}$$

where $\xi = \frac{\pi\omega_0^2}{\lambda}$ is confocal length. $(z - z_0)$ is a variable meaning the distance from z to z_0. Now plug ω_1 and ω_2 into equation (7.1), we get

$$\omega_1^2 = \omega_0^2 + \frac{\lambda^2}{\pi^2\omega_0^2}(z_1 - z_0)^2, \tag{7.2}$$

$$\omega_2^2 = \omega_0^2 + \frac{\lambda^2}{\pi^2\omega_0^2}(z_2 - z_0)^2, \tag{7.3}$$

now (7.2)-(7.3):

$$\omega_1^2 - \omega_2^2 = \frac{\lambda^2}{\pi^2\omega_0^2}[(z_1 - z_0)^2 - (z_2 - z_0)^2]. \tag{7.4}$$

We also have

$$\frac{\omega_1^2 - \omega_0^2}{\omega_2^2 - \omega_0^2} = \frac{(z_1 - z_0)^2}{(z_2 - z_0)^2}, \tag{7.5}$$

from (7.5):

$$\omega_0^2 = \frac{(z_1 - z_0)^2\omega_2^2 - (z_2 - z_0)^2\omega_1^2}{(z_1 - z_0)^2 - (z_2 - z_0)^2}. \tag{7.6}$$

(7.6) in (7.4):

$$\omega_1^2 - \omega_2^2 = \frac{\lambda^2}{\pi^2}\frac{[(z_1 - z_0)^2 - (z_2 - z_0)^2]^2}{(z_1 - z_0)^2\omega_2^2 - (z_2 - z_0)^2\omega_1^2}, \tag{7.7}$$

let

$$k \equiv \frac{\pi^2}{\lambda^2}(\omega_1^2 - \omega_2^2), \tag{7.8}$$

equation (7.7) finally can be written as:

$$az_0^2 + bz_0 + c = 0, \tag{7.9}$$

where

$$a = 4(z_1 - z_2)^2 - K(\omega_2^2 - \omega_1^2), \tag{7.10}$$

$$b = 2K(z_1\omega_2^2 - z_2\omega_1^2) - 4(z_1 - z_2)^2(z_1 + z_2), \tag{7.11}$$

$$c = (z_1 - z_2)^2(z_1 + z_2)^2 + K(\omega_1^2 z_2^2 - \omega_2^2 z_1^2). \tag{7.12}$$

Now, z_0 can be solved to get

$$z_0 = \frac{-b \pm \sqrt{b^2 - 4ac}}{2a}. \tag{7.13}$$

Now, after solve the z_0, we can get ω_0 from (7.6). Thus we completely solve the equations and obtain the focus spot size. One thing to note is that the "+" or "-" sign is decided by physical meaning, i.e., z_0 value has to be less than z_1 and z_2 as depicted in Fig. 7.3.

We give specific example about our measurement on N.A. 0.85, 60X objective. We first set micrometer reading at z_1=6.985mm. Then we do a normal beam profile scan. The profile is shown in Fig. 7.5. We then translate z-micrometer to z_2=7.620mm and do another scan for beam profile. The profile for z_2 is shown in Fig. 7.6.

We now fit the observed profiles to following Gaussian beam shape:

$$a_1 e^{-\frac{2(x-a_2)^2}{\omega^2}}$$

here a_1, a_2 and ω are fitting parameters. We get the fitting values of ω_1=0.580242mm, ω_2 = 0.762624mm respectively.

From these ω_1, ω_2 values, plus the z_1 and z_2 coordinates, using λ=840nm, we finally solve for z_0 and ω_0 as follows:

$$z_0^+ = 7.25938mm \qquad \omega_0^+ = 0.000126436mm$$

$$z_0^- = 4.96477mm \qquad \omega_0^- = 0.000930938mm$$

Because $z_0^+ > z_1$ which is non-sensible, we therefore only retain the "-" sign solution. Therefore, we finally arrive at our focus spot size for objective N.A. = 0.85, 60X as

$$\omega_0^- = 0.930938\mu m$$

or, the focus spot diameter is

$$2\omega_0 \sim 1.8\mu m$$

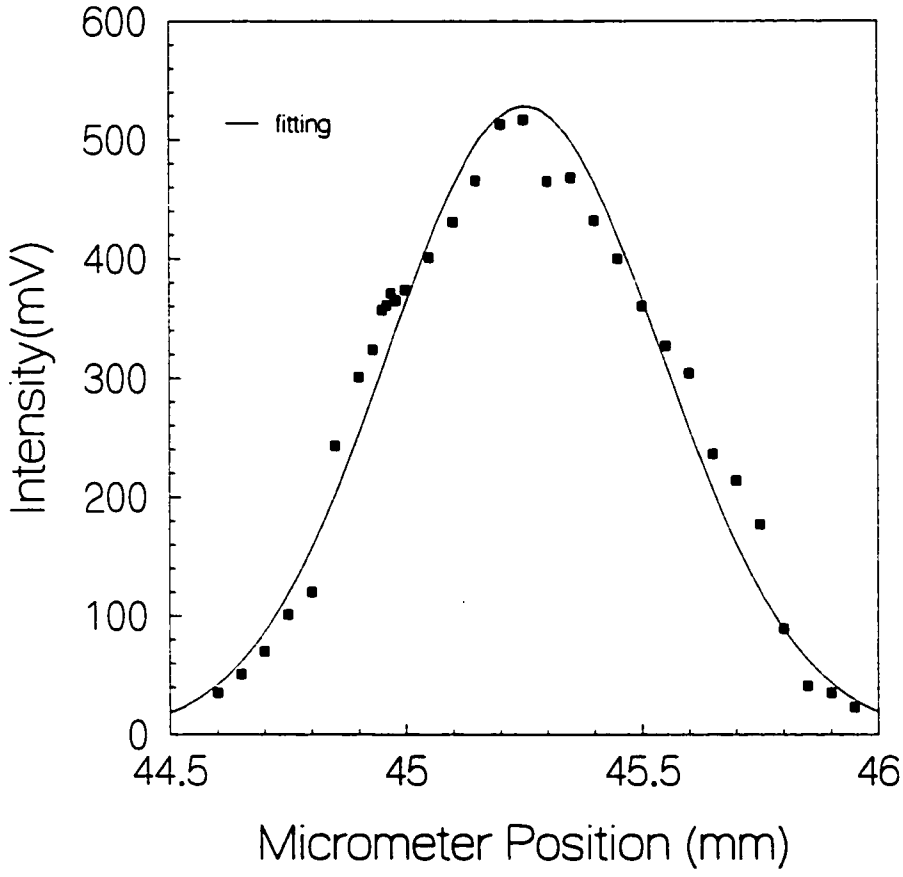

Figure 7.5: The scanned laser beam profile at position z_1. Solid line is fitting to Gaussian shape. The fitting values are a_1=528.518, a_2=45.2522, ω=0.580242.

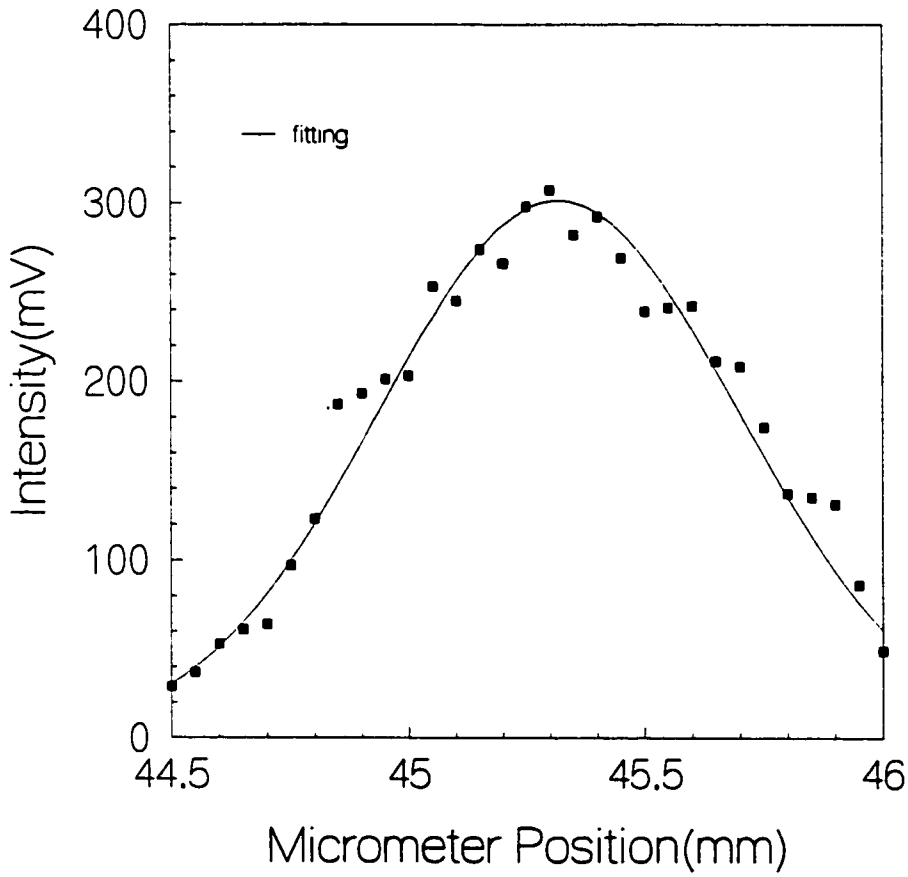

Figure 7.6: The scanned laser beam profile at position z_2. Solid line is fitting to Gaussian shape. The fitting values are a_1=301.363, a_2=45.3169, ω=0.762624.

Chapter 8

Conclusion

We have reported the angle-resolved Second-Harmonic Generation (SHG) light scattering from colloidal particles in Malachite Green solution. SHG is generally thought to be forbidden from centrosymmetric system such as liquid solutions in dipole approximation. The observation of SHG from such isotropic liquid medium suggests a new origin for the SHG: the interface between particle and the surrounding medium. This new phenomenon provides an interesting methodology in studying surface process in colloidal suspension.

We carried out the first experimental measurements of angular characteristics in SHG light scattering from colloidal suspension. We measured in detail the angular profiles for different particle sizes and for different light beam polarization configurations. We found uncharacteristic forward scattering signal in our raw data measurements. We identified the origin for this forward scattering signal. We then were able to extract the SHG signal from the colloidal sample. We theoretically solve

the Rayleigh-Gans-Debye approximation in SHG light scattering context. From this RGD theory, we are able to fit our extracted SHG signal. We compare the difference between linear and SHG light scattering. We conclude that for SHG light scattering, the forward scattering is forbidden. We also found that s-polarized SH radiation is depressed no matter what input polarization is used. Our SHG light scattering analysis shows that SHG scattering mainly occurs at a small but non-zero angle and this result is significant in that people can design their experiment to detect SHG off-axis to increase their signal to noise ratio.

In our nonlinear optical microscope project, we report the implementation of a nonlinear microscope. We report the first observations for SHG from single particle. We studied three particle types and several particle sizes. We observe exponentially enhanced SHG signals in addition to the expected quadratic response. For the quadratic regime, we have parameterized the data with a simple model. We conclude that the effective nonlinear susceptibility depends on particle type, but not so much on particle size. We also point out the general theoretical difficulty associated with this kind of nonlinear microscope. For the exponentially enhanced regime, we provide a simple model to mathematically suggest that higher-order nonlinear optical process is responsible for this exponential enhancement. We suggest that the enhancement is proportional to the imaginary part of the third-order nonlinear optical susceptibility. We also propose that the enhancement is related to the large local electric fields

which induce multi-photon ionization processes (e.g. presumably through particle cavity modes and possible third-order nonlinear optical effects). These multi-photon ionization processes, in turn, can dramatically alter the linear and nonlinear properties of the particles. In the future, when people can comfortably characterize the tightly focused laser beam, people can then calculate the local electric field inside the particles. From the calculations, it is then possible to find out the mechanism that triggers the exponential growth.

Appendix A

Theory of Dye Adsorption on Particles

The theory of dye adsorption on particles has been well written by Wang [36] et al. Here, I will only summarize the main points.

Langmuir model [117] regarding adsorption states that the surface can be treated as lattice of noninteracting sites with the adsorption process described as the "reaction" between bulk molecules (M) and empty surface sites (ES) to give filled sites (FS)

$$M + ES \rightleftharpoons FS \tag{A.1}$$

The kinetic equation is:

$$\frac{dN}{dt} = k_a \frac{C - N}{55.5}(N_{max} - N) - k_b N \tag{A.2}$$

here, N is the number of adsorbed molecules at the interface per unit volume, N_{max} is the maximum number of sites per unit volume, and k_a and k_d are the rate constants for adsorption and desorption, respectively. C is the total number of adsorbed and bulk molecules per unit volume. (C-N)/55.5 is the mole fraction of the adsorbing

molecules in the bulk solution, where 55.5 is the molarity of water.

The physical meaning of equation (A.2) is obvious. The first term on the right side means the rate at which adsorbate (MG) molecules strike a surface of an adsorbent (PS) is proportional to the product of the number of available adsorbates and the unabsorbed number of sites on the surface. The second term means the rate of desorption from the surface is directly proportional to the surface coverage. The left side is the net rate at which surface population changes.

Note that we use (C-N) instead of C on the first term of the right side. This is the modified Langmuir model which states that the depletion of adsorbates in the bulk solution due to adsorption to the interface can't be neglected. This is true for dye adsorption on the spherical surface, in which case the total surface area of a suspension of microparticles such as beads can be very large and hence N can be comparable with C.

When in equilibrium, $\frac{dN}{dt} = 0$, eq.(A.2) becomes:

$$k_a \frac{C-N}{55.5}(1 - \frac{N}{N_{max}}) = k_d \frac{N}{N_{max}} \tag{A.3}$$

Rearrange, we get

$$KN_{max}(\frac{N}{N_{max}})^2 - (55.5 + KN_{max} + KC)\frac{N}{N_{max}} + KC = 0 \tag{A.4}$$

Solve we get

$$\frac{N}{N_{max}} = \frac{(C + N_{max} + 55.5/K) \pm \sqrt{(C + N_{max} + 55.5/K)^2 - 4CN_{max}}}{2N_{max}} \tag{A.5}$$

When $C \rightarrow \infty$, the coverage should approach 1, therefore only "-" sign is physically meaningful. We retain the "-" sign and then it is equation (4.2).

Appendix B

Surface Potential of Charged Colloidal Particle

In this Appendix, we will derive the surface potential of charged colloidal particle. The model used is the widely accepted Gouy-Chapman model [118].

When immersed in an electrolyte solution, a charged colloidal particle will be surrounded by ions of opposite sign so that, from a distance, it appears to be electrically neutral. The surrounding ions are, however, able to move under the influence of thermal diffusion so that the region of charge imbalance, due to the presence of the particle, can be quite significant, relative to the size of the particle itself. The arrangement of electric charge on the particle, together with the balancing charge in the solution, is called an electrical double layer. The surface potential of charged particle is therefore dependent upon the electrolyte concentration, particle surface charge, etc. We use the simple model in Fig.B.1. Here $\hat{x}$ direction is normal to particle surface. The origin is set at the particle surface (x=0). The double layer is between surface and somewhere in $x > 0$ region. We represent the double layer dielectric constant the

same as that of bulk solution as ϵ. ϕ_b means the electrostatic potential far away in the bulk solution. The question is what is the potential any point inside the double layer? We consider $x > 0$ region in the following.

We start from Poisson equation [57]:

$$\nabla^2\phi = -\frac{4\pi\rho}{\epsilon} \tag{B.1}$$

The ions distribution will be influenced by the local electrostatic potential and the accumulation of oppositely charged ions. The distribution is given by Boltzmann equation:

$$n_i = n_i^0 e^{-\frac{w_i}{kT}} \tag{B.2}$$

Here w_i is the work needed to bring an ion i up from the bulk solution (where $\phi = \phi_b$) to a point in the double layer where the potential is ϕ and n_i^0 is the bulk concentration of ions of type i.

As a first approximation, we assume that

$$w_i = z_i e(\phi - \phi_b) \equiv z_i e\psi \tag{B.3}$$

where $\psi = \phi - \phi_b$, z_i is the valency of ions. Plugging $\rho = \sum_i n_i z_i e$, we get

$$\nabla^2\psi = -\frac{4\pi}{\epsilon}\sum_i n_i^0 z_i e e^{-\frac{z_i e\psi}{kT}} \tag{B.4}$$

or explicitly

$$\begin{aligned}\nabla^2\psi &= -\frac{4\pi}{\epsilon}(n_+^0 z_+ e e^{-\frac{z_+ e\psi}{kT}} + n_-^0 z_- e e^{-\frac{z_- e\psi}{kT}}) \\ &= \frac{4\pi}{\epsilon}2n^0 z e sinh\frac{ze\psi}{kT}\end{aligned} \tag{B.5}$$

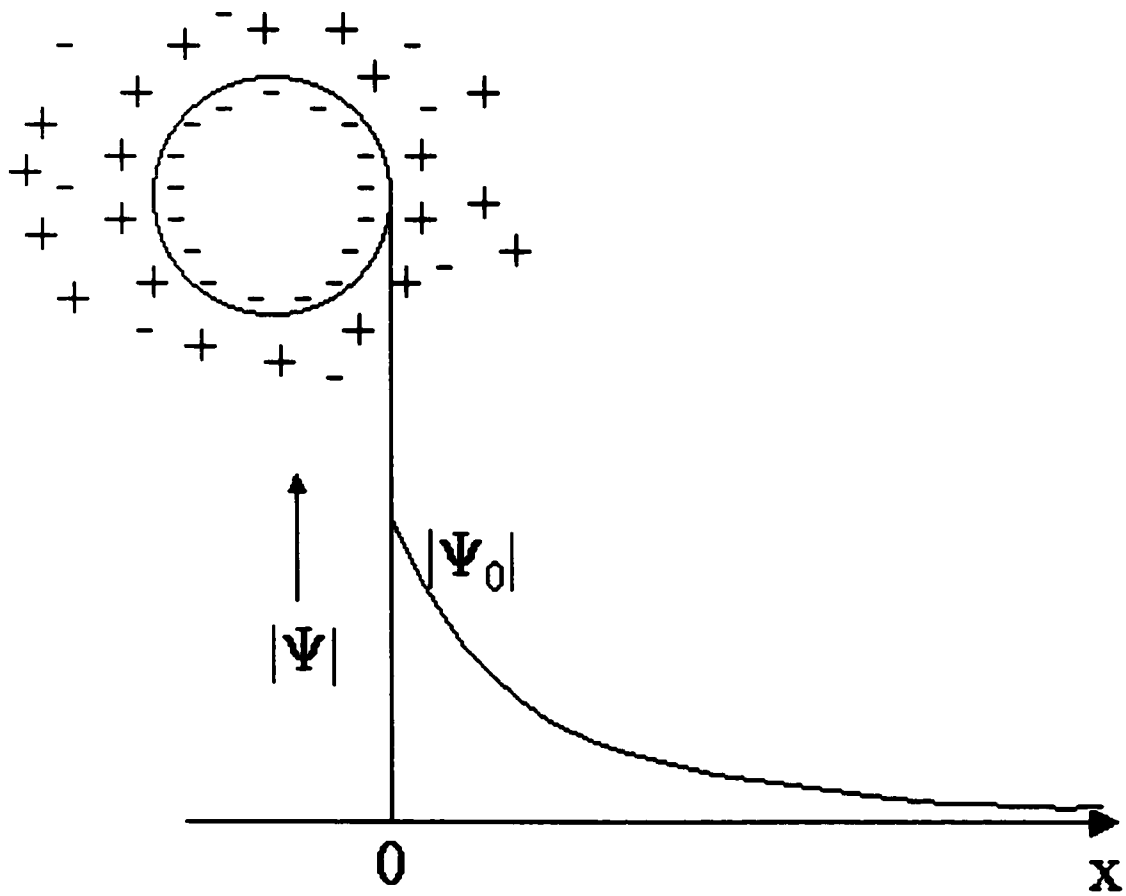

Figure B.1: Double layer model for colloidal solution. $|\Psi_0|$ is the electric potential on particle surface.

Here, we let $n^0 = n^0_+ = n^0_-$, $z^+ = -z_- = z$ (consider symmetric electrolyte such as our KCl case). Two sides $\times 2\frac{d\psi}{dx}$ and integrate (using the boundary condition that in the bulk solution, both ψ and $\frac{d\psi}{dx}$ are zeros):

$$\frac{d\psi}{dx} = \sqrt{\frac{16\pi n^0 kT}{\epsilon}(cosh\frac{ze\psi}{kT} - 1)} \tag{B.6}$$

using $\sqrt{coshx - 1} = \pm\sqrt{2}sinh\frac{x}{2}$, and we get

$$\frac{d\psi}{dx} = -\sqrt{\frac{32\pi n^0 kT}{\epsilon}}sinh\frac{ze\psi}{2kT} \tag{B.7}$$

where we only retain the "-" sign, this can be understood for example, when surface charge is positive, $\psi = \phi - \phi_b > 0$, so $sinh\frac{ze\psi}{2kT} > 0$, so when x increase, we expect $|\psi|$ decrease, i.e. expect $\frac{d\psi}{dx} < 0$, so should choose "-" sign. Similar analysis can be done for surface charge is negative case.

Now define $\kappa = \sqrt{\frac{8\pi e^2 n^0 z^2}{\epsilon kT}}$ and integrate we can get

$$tanh\frac{ze\psi}{4kT} = tanh\frac{ze\psi_0}{4kT}e^{-\kappa x} \tag{B.8}$$

where ψ_0 is the potential on the surface. Notice that we use the fact $\int \frac{dx}{sinhx} = ln(tanh\frac{x}{2})$ and $(tanhx)' = sech^2x$. It is clear now that κ^{-1} is the physical double layer width.

Equation (B.8) is the final solution to our Poisson equation (B.1). It relates ψ anywhere in the double layer to the potential ψ_0 of the surface. Now we can try to relate surface potential to diffuse layer surface charge σ_0.

The diffuse layer surface charge density σ_0 is

$$\begin{aligned}\sigma_0 &= \int_0^\infty \rho dx \\ &= \int_\infty^0 \frac{\epsilon}{4\pi}\frac{d^2\psi}{dx^2}dx \\ &= \frac{\epsilon}{4\pi}\frac{d\psi}{dx}|_\infty^0 \end{aligned} \tag{B.9}$$

In the bulk, we have $\frac{d\psi}{dx}|_\infty = 0$, therefore

$$\sigma_0 = \frac{\epsilon}{4\pi}(\frac{d\psi}{dx})_{x=0} \tag{B.10}$$

from equation (B.7), we get

$$\sigma_0 = -\sqrt{\frac{2\epsilon n^0 kT}{\pi}} sinh\frac{ze\psi_0}{2kT} \tag{B.11}$$

or,

$$\psi_0 = \frac{2kT}{ze} sinh^{-1}(-\sigma_0\sqrt{\frac{\pi}{2n^0\epsilon kT}}\ ) \tag{B.12}$$

Now, if we assume particle surface charge is σ, and we assume no free-charge region exist, then we have $\sigma = -\sigma_0$ and we finally relate the particle surface charge with the surface potential:

$$\psi_0 = \frac{2kT}{ze} sinh^{-1}(\sigma\sqrt{\frac{\pi}{2n^0\epsilon kT}}\ ) \tag{B.13}$$

Now if we replace n^0 with C and ψ_0 with $\Phi(0)$, we get equation (4.7).

Appendix C

Derivation of Integral in Equation (5.13)

The integral in equation (5.13) is

$$I \equiv \int d^3\mathbf{r}'(\hat{e_y} \cdot \hat{e_{r'}})^2 e^{i\mathbf{q}\cdot\mathbf{r}'} \hat{e_{r'}}$$

We can move $\hat{e_y}$ outside and get

$$I = \hat{e_y} \cdot (\int d^3\mathbf{r}' \hat{e_{r'}} \hat{e_{r'}} \hat{e_{r'}} e^{i\mathbf{q}\cdot\mathbf{r}'}) \cdot \hat{e_y} \tag{C.1}$$

To calculate this integral, we now choose a new set of coordinate system. As shown in Fig.5.14, we choose $(\hat{i}\hat{j}\hat{k})$ system, i.e. we choose $\mathbf{q}$ as $\hat{k}$, $\hat{j}$ parallel to $\hat{y}$ and $\hat{i}$ perpendicular to $\hat{j}$ and $\hat{k}$. We have

$$\hat{e_r}' = sin\theta' cos\phi' \hat{i} + sin\theta' sin\phi' \hat{j} + cos\theta' \hat{k} \tag{C.2}$$

Considering that there is $\hat{e_y} = \hat{j}$ on left side and right side of the integral, we only need to write down the terms of dyadic that has $\hat{j}$ component on left and right side, i.e. we only concern

$$(\hat{e_r'}\hat{e_r'}\hat{e_r'})_{jnj} = sin\theta' sin\phi' \hat{j}(sin\theta' cos\phi' \hat{i} + sin\theta' sin\phi' \hat{j} + cos\theta' \hat{k}) sin\theta' sin\phi' \hat{j} \tag{C.3}$$

where subscript "n" means that it can be any component. We substitute above equation into equation (C.1) and immediately get

$$I = \int sin^2\theta' sin^2\phi'(sin\theta' cos\phi' \hat{i} + sin\theta' sin\phi' \hat{j} + cos\theta' \hat{k}) d^3\mathbf{r} e^{i\mathbf{q}\cdot\mathbf{r}} \tag{C.4}$$

There are three components in this integral, we denote each component using subscript corresponding to the component index, e.g, use I_i to denote the i-component. By this way, through some calculations, we find out

$$I_i = I_j = 0$$

and

$$I_k = -\frac{4\pi R}{iq} F_s(\theta)$$

where $F_s(\theta)$ is defined in equation (5.17). We use the relationship

$$\int_0^{2\pi} d\phi' sin^2\phi' cos\phi' = \int_0^{2\pi} sin^3\phi' d\phi' = 0$$

and

$$\int_0^{2\pi} sin^2\phi' d\phi' = \pi$$

substitute these results into equation (C.4) we finally obtain

$$\int d^3\mathbf{r}'(\hat{e_y} \cdot \hat{e_{r'}})^2 e^{i\mathbf{q}\cdot\mathbf{r}'} \hat{e_{r'}} = -\frac{4\pi R}{iq} F_s(\theta)\hat{k} \tag{C.5}$$

$$= -\frac{4\pi R}{iq} F_s(\theta)(-cos\frac{\theta}{2}\hat{x} + sin\frac{\theta}{2}\hat{z}) \tag{C.6}$$

Appendix D

Derivation of Integral (5.19)

The integral in (5.19) is

$$\int d^3\mathbf{r}'(\hat{e_x}\cdot\hat{e_{r'}})^2 e^{i\mathbf{q}\cdot\mathbf{r}'}\hat{e_r'}$$

Use I to denote the integral, after rearrangement, we get

$$I = \hat{e_x}\cdot(\int d^3\mathbf{r}'\hat{e_{r'}}\hat{e_{r'}}\hat{e_{r'}}e^{i\mathbf{q}\cdot\mathbf{r}'})\cdot\hat{e_x} \tag{D.1}$$

similar to the integral in Appendix C, we write out explicitly the terms involved dyadic whose left and right side has $\hat{i}$ or $\hat{k}$ components

$$\begin{aligned}(\hat{e_r'}\hat{e_r'}\hat{e_r'})_{eff} &= (sin\theta' cos\phi'\hat{i} + cos\theta'\hat{k})(sin\theta' cos\phi'\hat{i} + sin\theta' sin\phi'\hat{j} + cos\theta'\hat{k}) \\ &\quad \cdot(sin\theta' cos\phi'\hat{i} + cos\theta'\hat{k})\end{aligned} \tag{D.2}$$

There are 12 terms, each with 3 indices. Again, we use same subscripts as those indices to denote each term of integral, for example, we use I_{ijk} to denote the term with indices of (ijk). After some calculations, we can obtain the value for each integral and tabulate them in Table D.1. where $F_s(\theta)$ and $F_p(\theta)$ are defined in equation (5.17)

and (5.20) respectively.

Now, equation (D.1) become:

$$I = \hat{e_x} \cdot [-\frac{4\pi R}{iq} F_s(\theta)(\hat{i}\hat{i}\hat{k} + \hat{i}\hat{k}\hat{i} + \hat{k}\hat{i}\hat{i}) + \frac{8\pi R}{iq} F_p(\theta)\hat{k}\hat{k}\hat{k}] \cdot \hat{e_x} \tag{D.3}$$

From the directional relationship Fig.5.14, we easily find

$$\hat{e_x} \cdot \hat{i} = sin\frac{\theta}{2}, \qquad \hat{e_x} \cdot \hat{k} = -cos\frac{\theta}{2}$$

Finally, we obtain the solution

$$\int d^3\mathbf{r}'(\hat{e_x} \cdot \hat{e_{r'}})^2 e^{i\mathbf{q}\cdot\mathbf{r}'} \hat{e_r'} = -\frac{4\pi R}{iq} F_s(\theta)(-sin\theta\hat{i} + sin^2\frac{\theta}{2}\hat{k}) + \frac{8\pi R}{iq} F_p(\theta)cos^2\frac{\theta}{2}\hat{k} \tag{D.4}$$

Table D.1: The Integral Value For Each Term in Equation (D.1)

term	value
I_{iii}	0
I_{iik}	$-\frac{4\pi R}{iq}F_s(\theta)$
I_{iji}	0
I_{ijk}	0
I_{iki}	$-\frac{4\pi R}{iq}F_s(\theta)$
I_{ikk}	0
I_{kii}	$-\frac{4\pi R}{iq}F_s(\theta)$
I_{kik}	0
I_{kji}	0
I_{kjk}	0
I_{kki}	0
I_{kkk}	$\frac{8\pi R}{iq}F_p(\theta)$

Appendix E

Rayleigh-Gans-Debye Approximation for Linear Light Scattering

In linear light scattering, the form factor is defined as:

$$S(\mathbf{K}) = \frac{Scattered\ intensity\ observed\ at\ \theta_s}{Scattered\ intensity\ without\ interference(\theta_s = 0)}. \tag{E.1}$$

We show the coordinate system in Fig. E.1. Where, OO' represents the reference plane for incident wave, PP' represents the reference plane for scattering wave. θ_s is the scattering angle, $\mathbf{r}_j$ is the position vector for one point in the scattering medium. We use $\mathbf{k}_i$ and $\mathbf{k}_s$ to represent the incident and scattering wave vector respectively. The phase difference for two rays are:

$$\phi = \mathbf{r}_j \cdot \mathbf{k}_i - \mathbf{r}_j \cdot \mathbf{k}_s. \tag{E.2}$$

If we let $\mathbf{Q} = \mathbf{k}_i - \mathbf{k}_s$ (scattering vector), then we get

$$\phi = \mathbf{r}_j \cdot \mathbf{Q}. \tag{E.3}$$

The magnitude of $\mathbf{Q}$ can be shown to be (see Fig. E.2):

$$|\mathbf{Q}| = \frac{4\pi n}{\lambda_0} sin\frac{\theta_s}{2}, \tag{E.4}$$

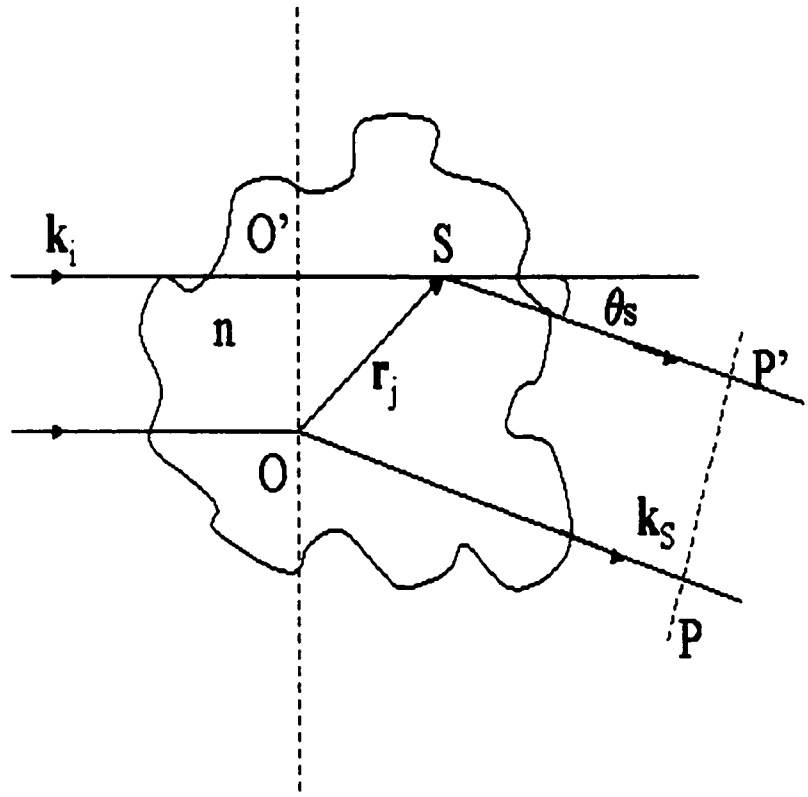

Figure E.1: Schematic of coordinate system for Rayleigh-Gans-Debye approximation for linear light scattering. OO' and PP' are reference plane for incident and scattering wave respectively. θ_s is the scattering angle. $\mathbf{k}_i$ and $\mathbf{k}_s$ are incident and scattering wave vector respectively. $\mathbf{r}_j$ is the position vector inside the scattering volume. n is the index of refraction of scattering medium.

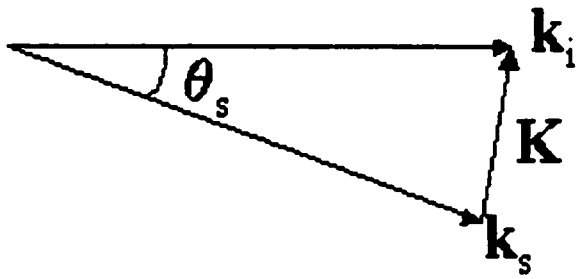

Figure E.2: Geometrical relationship between $\mathbf{k}_i$, $\mathbf{k}_s$ and $\mathbf{Q}$. θ_s is the scattering angle. here n is the index of refraction of particle and λ_0 is the wavelength in vacuum. $|\mathbf{k}_i| = |\mathbf{k}_s| = \frac{2\pi n}{\lambda_0}$.

The electric field of light scattered by the jth segment is:

$$\mathbf{E}_j = \mathbf{a}_j e^{i\mathbf{Q}\cdot\mathbf{r}_j} E_0 e^{-i\omega_0 t}. \tag{E.5}$$

Total scattered electric field is:

$$\begin{aligned} \mathbf{E}_s &= \sum_{j=1}^{n} \mathbf{E}_j \\ &= E_0 e^{-i\omega_0 t} \sum_{j=1}^{n} \mathbf{a}_j e^{i\mathbf{Q}\cdot\mathbf{r}_j}, \end{aligned} \tag{E.6}$$

here n is the total number of segments. The scattered light intensity is then:

$$I_s(\theta_s) \propto |\sum_{j=1}^{n} \mathbf{a_j} e^{i\mathbf{Q}\cdot\mathbf{r}_j}|^2 E_0^2. \tag{E.7}$$

Equation (E.7) is for the light scattering intensity from one particle with a fixed orientation. For an ensemble of randomly oriented particles, the intensity is given by

$$I_s(\theta_s) \propto N < |\sum_{j=1}^{n} \mathbf{a_j} e^{i\mathbf{Q}\cdot\mathbf{r}_j}|^2 >_{angle} E_0^2. \tag{E.8}$$

Where N is the total number of particles per unit volume and $< \ >_{angle}$ is ensemble average of randomly oriented particles.

At $\theta_s = 0$, we have

$$I_s(\theta_s = 0) \propto Nn^2|a|^2 E_0^2, \tag{E.9}$$

here we assume $\mathbf{a_1} = \mathbf{a_2} = \mathbf{a_3} = ...$, the form factor is then calculated to be:

$$S(\mathbf{Q}) =< |\frac{1}{n}\sum_{j=1}^{n} e^{i\mathbf{Q}\cdot\mathbf{r}_j}|^2 >_{angle} . \tag{E.10}$$

Equation (E.10) is the general formula for calculating the linear light scattering form factor. Now we examine the case for uniform spherical scatters.

Because of spherical symmetry, $< \ >_{angle}$ can be ignored because all particles have same orientation, we therefore get

$$\begin{aligned} S(\mathbf{Q}) &= |\frac{1}{n}\sum_{j=1}^{n} e^{i\mathbf{Q}\cdot\mathbf{r}_j}|^2 \\ &= |\frac{2\pi \int_0^R \int_{\alpha=0}^{\pi} e^{iQr cos\alpha} sin\alpha d\alpha r^2 dr}{4\pi \int_{r=0}^{R} r^2 dr}|^2 \\ &= |\frac{2\pi \int_0^R \frac{2sinQr}{Qr} r^2 dr}{\frac{4\pi}{3}R^3}|^2. \end{aligned} \tag{E.11}$$

Here we use the result $\int_0^\pi e^{iQrcos\alpha} = \frac{2sinQr}{Qr}$. After further integration, we finally obtain the form factor for linear light scattering:

$$S(\mathbf{Q}) = \frac{9}{(QR)^6}(sinQR - QRcosQR)^2. \tag{E.12}$$

Appendix F

Coding for Mie Scattering Calculations

In this Appendix, we will first summarize the Mie theory and then include the coding we wrote for the Mie scattering calculation.

Mie theory is the rigorous way to solove the wave equation for the electric field inside or outside particle [2]. We use SI unit system in this Appendix. The spherical polar coordinate system is shown in Fig.F.1. The origin is at the center of particle, incident wave is along z-direction. Particle radius is R. We use $\mathbf{E}_i$ to indicate the field inside particle, $\mathbf{E}_s$ to indicate the field outside the particle, i.e. $\mathbf{E}_s$ is also the scattering field.

For convenience, we use the p-polarized incident wave, i.e., the incident wave is

$$\mathbf{E}_0 = E_0 e^{i\mathbf{k}\cdot\mathbf{r}} \hat{e_x} \tag{F.1}$$

After solving the appropriate wave equation, the complete solution for electric fields are [2]:

$$\mathbf{E}_i = \sum_{n=1}^{\infty} E_n (C_n \mathbf{M}_{o1n}^{(1)} - i d_n \mathbf{N}_{e1n}^{(1)}) \tag{F.2}$$

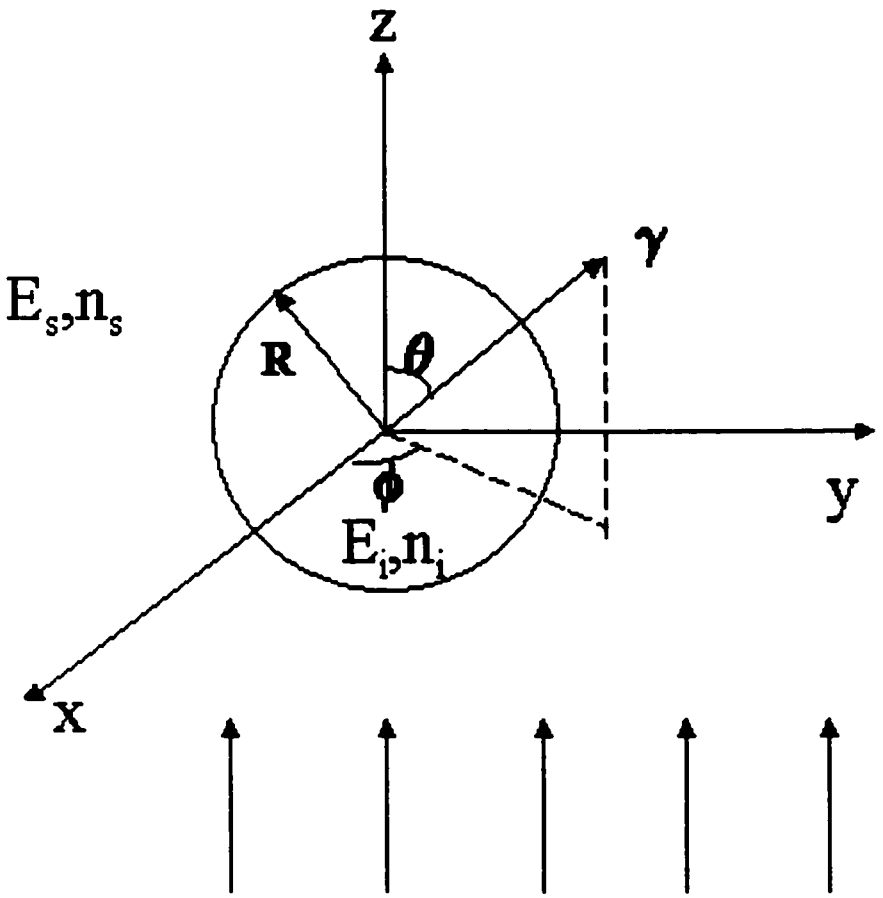

Figure F.1: Coordinate system for Mie calculations. Subscript "s" denote the scattering medium, "i" denote the particle. Particle radius is R.

for the field inside the particle and

$$\mathbf{E}_s = \sum_{n=1}^{\infty} E_n(ia_n\mathbf{N}_{e1n}^{(3)} - b_n\mathbf{M}_{o1n}^{(3)}) \tag{F.3}$$

for the scattered field.

We will summerize the meaning for each variable in the following:

(1)E_n equals:

$$E_n = \frac{i^n E_0(2n+1)}{n(n+1)} \tag{F.4}$$

(2)a_n, b_n, c_n, d_n are all coefficients defined by boundary conditions as

$$a_n = \frac{\mu_s m^2 j_n(mx)[xj_n(x)]' - \mu_1 j_n(x)[mxj_n(mx)]'}{\mu_s m^2 j_n(mx)[xh_n^{(1)}(x)]' - \mu_1 h_n^{(1)}(x)[mxj_n(mx)]'} \tag{F.5}$$

$$b_n = \frac{\mu_1 j_n(mx)[xj_n(x)]' - \mu_s j_n(x)[mxj_n(mx)]'}{\mu_1 j_n(mx)[xh_n^{(1)}(x)]' - \mu_s h_n^{(1)}(x)[mxj_n(mx)]'} \tag{F.6}$$

$$c_n = \frac{\mu_1 j_n(x)[xh_n^{(1)}(x)]' - \mu_1 h_n^{(1)}(x)[xj_n(x)]'}{\mu_1 j_n(mx)[xh_n^{(1)}(x)]' - \mu_s h_n^{(1)}(x)[mxj_n(mx)]'} \tag{F.7}$$

$$d_n = \frac{\mu_1 m j_n(x)[xh_n^{(1)}(x)]' - \mu_1 m h_n^{(1)}(x)[xj_n(x)]'}{\mu_s m^2 j_n(mx)[xh_n^{(1)}(x)]' - \mu_1 h_n^{(1)}(x)[mxj_n(mx)]'} \tag{F.8}$$

where $x = kR = \frac{2\pi n_s}{\lambda}$, $m = \frac{n_i}{n_s}$. n_i isthe refractive index of particle, n_s is the refractive index of medium surrounding the particle, λ is the wavelength of incident wave. μ_s and μ_i are the magnetic permeability of scattering medium and of the particle respectively. For our non-magnetic particle, we treat μ_s and μ_i as 1 in this here.

$j_n(\rho)$ is spherical Bessel functions, $h_n^{(1)}(\rho) = j_n(\rho) + iy_n(\rho)$ is the spherical Hankel functions. The functions are discussed in the following:

$j_n(\rho)$ and $y_n(\rho)$ are both called spherical Bessel functions. They satisfy the same important recurrence relations:

$$z_{n-1}(\rho) + z_{n+1}(\rho) = \frac{2n+1}{\rho} z_n(\rho) \tag{F.9}$$

$$(2n+1)\frac{d}{d\rho} z_n(\rho) = n z_{n-1}(\rho) - (n+1) z_{n+1}(\rho) \tag{F.10}$$

where z_n is either j_n or y_n. From the first two orders

$$j_0(\rho) = \frac{sin\rho}{\rho}, \qquad j_1(\rho) = \frac{sin\rho}{\rho^2} - \frac{cos\rho}{\rho},$$

$$y_0(\rho) = -\frac{cos\rho}{\rho}, \qquad y_1(\rho) = -\frac{cos\rho}{\rho^2} - \frac{sin\rho}{\rho}$$

higher-order functions are generated by recurrence. Note that for all orders n, $y_n(kr)$ becomes infinite as r approaches the origin. For far field $kr \gg n^2$, $h_n^{(1)} \sim \frac{(-i)^n e^{ikr}}{ikr}$.

$[\rho j_n(\rho)]'$ is derivative with respective to ρ. The higher-order values of derivatives of $j_n(\rho)$ and $h_n^{(1)}(\rho)$ can also be generated from above recurrence relations.

(3)M and N are called vector harmonics. They are defined by following:

$$\mathbf{M}_{o1n}^{(1)} = \frac{1}{sin\theta} cos\phi P_n^1(cos\theta) j_n(\rho)\hat{e_\theta} - sin\phi \frac{dP_n^1(cos\theta)}{d\theta} j_n(\rho)\hat{e_\phi} \tag{F.11}$$

$$\begin{aligned}\mathbf{N}_{e1n}^{(1)} &= \frac{j_n(\rho)}{\rho} cos\phi n(n+1) P_n^1(cos\theta)\hat{e_r} + cos\phi \frac{dP_n^1(cos\theta)}{d\theta}\frac{1}{\rho}\frac{d}{d\rho}[\rho j_n(\rho)]\hat{e_\theta} \\ &\quad - sin\phi \frac{P_n^1(cos\theta)}{sin\theta}\frac{1}{\rho}\frac{d}{d\rho}[\rho j_n(\rho)]\hat{e_\phi}\end{aligned} \tag{F.12}$$

where supscript "(1)" and "(3)" means that the radial function is j_n and $h_n^{(1)}$ respectively. $P_n^m(cos\theta)$ is associated Legendre functions of the first kind of degree n and order m, where n=m, m+1,.....

$P_n^1(cos\theta)$ is calculated by following

$$P_n^1(cos\theta) = \frac{1}{sin\theta}(ncos\theta P_n - nP_{n-1}) \tag{F.13}$$

where P_n is Legendre polynomials and has following recurrence relationship

$$(n+1)P_{n+1} - (2n+1)cos\theta P_n + nP_{n-1} = 0 \tag{F.14}$$

From the first two orders $P_0(cos\theta) = 1, P_1(cos\theta) = cos\theta$, we can generate all higher order of $P_n(cos\theta)$ and also $P_n^1(cos\theta)$.

Thus, given the particle radius, particle index of refraction, medium index of refraction, the incident wavelength, we can use above recurrence relationships to generate all high-order functions and calculate the electric field inside and outside the particle.

Attached below is the coding in C++ we wrote to calculate the scattering electric field. Its correctness is checked by comparing the coefficients it computed with the published values (e.g. [2]) and they are exactly identical. To compile the code, use command "g++ Iscatter_angular.cc -o Iscatter_angular" and the excutable file will be "Iscatter_angular".

```
/*********************************************************************
**    Filename: Iscatter_angular.cc                                **
**    author: Ningping Yang                                        **
**    Date: 3/10/98                                                **
```

```
**                                                                    **
**    Note: This code is used to calculate the scattering  electric **
**          field intensity from a particle using Mie theory. Input **
**          the radius, the index of refraction (could  be complex) **
**          for  both  the  particle  and  the  medium,  input  the **
**          wavelength of the incident wave, then can calculate the **
**          scattering electric field intensity.                    **
**                                                                    **
**          The format data in record is: phi theta  rou  Intensity **
**                                                                    **
**********************************************************************/


#include <stdio.h>
#include <iostream.h>
#include <complex.h>
#include <fstream.h>

#define Pi 3.1415926
#define N 6
```

```
#define ROU_N 50

#define THETA_N 50

#define PHI_N 50

#define rou_outer 1000000 //outside field from 1000000*g_Radius


double LAMDA;

complex<double> index_sphere;

complex<double> index_medium;

double g_Radius; //unit: nm ; correspond to Diameter/2

complex<double> pure_imag(0, 1);



class field_intensity {

private:

  int n;

  complex<double> rou, rou2;

  double x;

  complex<double> jn_value, jn2_value;

  complex<double> djn_value, djn2_value;

  complex<double> drou_jn_value, drou2_jn2_value;
```

```
  complex<double> yn_value, dyn_value;

  complex<double> hn_value, dhn_value, drou_hn_value;

  complex<double> cn_value, dn_value, an_value, bn_value;

  double pn_value, pn1_value, dpn1_dtheta_value;

  field_intensity *F1, *F2;

public:

  field_intensity(complex<double> in_rou,double in_x,int in_n)

          {rou = in_rou; rou2 =index_sphere*in_rou/index_medium;

           x = in_x; n = in_n;}


  set_F1(field_intensity *in_F1){F1 = in_F1;}

  set_F2(field_intensity *in_F2){F2 = in_F2;}

  complex<double> get_jn_value();

  complex<double> get_jn2_value();

  complex<double> get_djn_value();

  complex<double> get_djn2_value();

  complex<double> get_yn_value();

  complex<double> get_dyn_value();

  complex<double> get_hn_value();

  complex<double> get_dhn_value();
```

```
  complex<double> get_drou_jn_value();

  complex<double> get_drou2_jn2_value();

  complex<double> get_drou_hn_value();

  complex<double> get_cn_value();

  complex<double> get_dn_value();

  complex<double> get_an_value();

  complex<double> get_bn_value();

  double  get_pn_value();

  double  get_pn1_value();

  double  get_dpn1_dtheta_value();

  void calculate();

  void calculate_p_theta(); // calculate theta relevant terms

  void calculate_j_rou(); // calculate rou relevant terms

  void calculate_coeff(); // calculate an,bn,cn,dn


private:


  void calc_jn_value();

  void calc_jn2_value();

  void calc_djn_value();
```

```
  void calc_djn2_value();

  void calc_yn_value();

  void calc_dyn_value();

  void calc_hn_value();

  void calc_dhn_value();

  void calc_drou_jn_value();

  void calc_drou2_jn2_value();

  void calc_drou_hn_value();

  void calc_cn_value();

  void calc_dn_value();

  void calc_an_value();

  void calc_bn_value();

  void calc_pn_value();

  void calc_pn1_value();

  void calc_dpn1_dtheta_value();

};



void field_intensity::calculate(){

  calc_jn_value();
```

```
  calc_jn2_value();

  calc_djn_value();

  calc_djn2_value();

  calc_yn_value();

  calc_dyn_value();

  calc_hn_value();

  calc_dhn_value();

  calc_drou_jn_value();

  calc_drou_hn_value();

  calc_drou2_jn2_value();

  calc_cn_value();

  calc_dn_value();

  calc_an_value();

  calc_bn_value();

  calc_pn_value();

  calc_pn1_value();

  calc_dpn1_dtheta_value();

}


void field_intensity::calculate_p_theta(){
```

```
  calc_pn_value();
  calc_pn1_value();
  calc_dpn1_dtheta_value();
}

void field_intensity::calculate_j_rou(){
  calc_jn_value();
  calc_jn2_value();
  calc_djn_value();
  calc_djn2_value();
  calc_yn_value();
  calc_dyn_value();
  calc_hn_value();
  calc_dhn_value();
  calc_drou_jn_value();
  calc_drou_hn_value();
  calc_drou2_jn2_value();
}

void field_intensity::calculate_coeff(){
```

```
  calc_cn_value();
  calc_dn_value();
  calc_an_value();
  calc_bn_value();
}

void field_intensity::calc_jn_value(){
  if (n == 0) {
jn_value = sin(rou)/rou;
return;
}
  if (n == 1) {
jn_value = sin(rou)/rou/rou - cos(rou)/rou;
return;
}
  jn_value = (2*n-1)*F1->get_jn_value()/rou - F2->get_jn_value();
}

void field_intensity::calc_jn2_value(){
  if (n == 0) {
```

```
jn2_value = sin(rou2)/rou2;
return;
}
  if (n == 1) {
jn2_value = sin(rou2)/rou2/rou2 - cos(rou2)/rou2;
return;
}
  jn2_value = (2*n-1)*F1->get_jn2_value()/rou2 - F2->get_jn2_value();
}


void field_intensity::calc_djn_value(){
  if (n == 0) {
djn_value = cos(rou)/rou - sin(rou)/rou/rou;
return;
}
  djn_value = F1->get_jn_value() - (n + 1)/rou*jn_value;
}



void field_intensity::calc_djn2_value(){
```

```
  if (n == 0) {
djn2_value = cos(rou2)/rou2 - sin(rou2)/rou2/rou2;
return;
}
  djn2_value = F1->get_jn2_value() - (n + 1)/rou2*jn2_value;
}



void field_intensity::calc_yn_value(){
  if (n == 0) {
yn_value = -cos(rou)/rou;
return;
}
  if (n == 1) {
yn_value = -cos(rou)/rou/rou - sin(rou)/rou;
return;
}
  yn_value = (2*n-1)/rou*F1->get_yn_value() - F2->get_yn_value();
}
```

```
void field_intensity::calc_dyn_value (){
  if (n==0) {
dyn_value = cos(rou)/rou/rou + sin(rou)/rou;
return;
}
  dyn_value = F1->get_yn_value() - (n+1)/rou*yn_value;
}

void field_intensity::calc_hn_value(){
  hn_value = jn_value + pure_imag * yn_value;
}

void field_intensity::calc_dhn_value(){
  dhn_value = djn_value + pure_imag * dyn_value;
}

void field_intensity::calc_drou_jn_value(){
  drou_jn_value = jn_value + rou*djn_value;
}
```

```
void field_intensity::calc_drou2_jn2_value(){
   drou2_jn2_value = jn2_value + rou2*djn2_value;
}

void field_intensity::calc_drou_hn_value(){
  drou_hn_value = hn_value + rou*dhn_value;
}

void field_intensity::calc_cn_value(){
  cn_value = (jn_value*drou_hn_value - hn_value*drou_jn_value)
          /(jn2_value*drou_hn_value - hn_value*drou2_jn2_value);
}

void field_intensity::calc_dn_value(){
  dn_value = (index_sphere*jn_value*drou_hn_value/index_medium
           - index_sphere*hn_value*drou_jn_value/index_medium)
           /(index_sphere*index_sphere*jn2_value*drou_hn_value
           /index_medium/index_medium - hn_value*drou2_jn2_value);
}
```

```
void field_intensity::calc_an_value(){
  an_value = (index_sphere*index_sphere*jn2_value*drou_jn_value
             /index_medium/index_medium - jn_value*drou2_jn2_value)
             /(index_sphere*index_sphere*jn2_value*drou_hn_value
             /index_medium/index_medium - hn_value*drou2_jn2_value);
}

void field_intensity::calc_bn_value(){
  bn_value = (jn2_value*drou_jn_value - jn_value*drou2_jn2_value)
           /(jn2_value*drou_hn_value - hn_value*drou2_jn2_value);
}

void field_intensity::calc_pn_value(){
  if(n == 0) {
    pn_value = 1;
    return;
}
  if(n == 1) {
    pn_value = x;
```

```
    return;
}
  pn_value=(2*n-1)*x*F1->get_pn_value()/n-(n-1)*F2->get_pn_value()/n;
}


void field_intensity::calc_pn1_value(){
  if(n == 0) {
    pn1_value = 0;
    return;
  }
  pn1_value = (n*x*pn_value - n*F1->get_pn_value())/sqrt(1-x*x);
}


void field_intensity::calc_dpn1_dtheta_value(){
  if(n == 0) {
    dpn1_dtheta_value = 0;
    return;
  }
  dpn1_dtheta_value = -(n*n + n/(1-x*x))*pn_value
                    + n*x*F1->get_pn_value()/(1-x*x);
```

```
}


complex<double> field_intensity::get_jn_value(){ return jn_value;}
complex<double> field_intensity::get_jn2_value(){ return jn2_value;}
complex<double> field_intensity::get_djn_value(){ return djn_value;}
complex<double> field_intensity::get_yn_value(){ return yn_value;}
complex<double> field_intensity::get_dyn_value(){ return dyn_value;}
complex<double> field_intensity::get_hn_value(){ return hn_value;}
complex<double> field_intensity::get_dhn_value(){ return dhn_value;}
complex<double> field_intensity::get_drou_jn_value()
                                { return drou_jn_value;}
complex<double> field_intensity::get_drou2_jn2_value()
                                { return drou2_jn2_value;}
complex<double> field_intensity::get_drou_hn_value()
                                { return drou_hn_value;}
complex<double> field_intensity::get_cn_value(){ return cn_value;}
complex<double> field_intensity::get_dn_value(){ return dn_value;}
complex<double> field_intensity::get_an_value(){ return an_value;}
```

```
complex<double> field_intensity::get_bn_value(){ return bn_value;}
double field_intensity::get_pn_value(){ return pn_value;}
double field_intensity::get_pn1_value(){ return pn1_value;}
double field_intensity::get_dpn1_dtheta_value()
                                { return dpn1_dtheta_value;}


main(){
  double theta, x;
  complex<double> rou;
  ofstream outFile;
  char file_name_str[100];


  cout <<"--------------- WELCOME -------------------"<<endl;
  cout <<"This code will calculate scattering field angular
         distribution"<<endl;
  cout <<"and save result in file. There are 4 columns in datafile,
          they are"<<endl;
  cout<<" -------- phi, theta, rou, intensity_value ------- "<<endl;
  cout << "Please input LAMDA (unit: nm): ";
  cin >> LAMDA;
```

```
cout << "Please input Radius (unit: nm): ";
cin >> g_Radius;

cout << "Input refractive index of sphere in format (real,imag): ";
cin >> index_sphere;
cout << "Input refractive index of medium in format (real,imag): ";
cin >> index_medium;

cout << "Please input the file name: ";
cin >> file_name_str;

cout << "LAMDA = "<< LAMDA<< ", "<< "Radius = "<< g_Radius << endl;
cout << "index_sphere (" << real(index_sphere) << ", "
        << imag(index_sphere)<< ")" << endl;
cout << "index_medium (" << real(index_medium) << ", "
        << imag(index_medium)<< ")" << endl;
cout << "file name = " << file_name_str << endl;
```

```
  outFile.open( file_name_str );
  field_intensity **F = new field_intensity*[N];



  double pn1_theta[THETA_N][N];
  double dpn1_dtheta[THETA_N][N];

for( int k = 1; k < THETA_N; k++)
{
        theta = k*Pi/THETA_N;
x = cos(theta);

for( int i = 0; i < N; i++ )
{
F[i] = new field_intensity( 0, x, i );
if( i == 1 ) {
     F[i] -> set_F1(F[i-1]);
   }
   if(i >= 2){
     F[i] -> set_F1(F[i-1]);
```

```
     F[i] -> set_F2(F[i-2]);
}
   F[i] -> calculate_p_theta();
pn1_theta[k][i] = F[i]->get_pn1_value();
dpn1_dtheta[k][i] = F[i]->get_dpn1_dtheta_value();
}
}

for( int i = 0; i < N; i++ )
{
delete F[i];
}


complex<double> jn_rou[ROU_N][N], drou_jn_rou[ROU_N][N];
complex<double> hn_rou[ROU_N][N], drou_hn_rou[ROU_N][N];


        for( int k = 1; k < ROU_N; k++ )
{
```

```
rou = (k + rou_outer) * 2 * Pi * index_medium*g_Radius / LAMDA  ;

for( int i = 0; i < N; i++ )
{
F[i] = new field_intensity( rou, 0, i );
if( i == 1 ) {
     F[i] -> set_F1(F[i-1]);
   }
   if(i >= 2){
     F[i] -> set_F1(F[i-1]);
     F[i] -> set_F2(F[i-2]);
}
   F[i] -> calculate_j_rou();

jn_rou[k][i] = F[i]->get_jn_value(); //k is rou,i is sub n
drou_jn_rou[k][i] = F[i]->get_drou_jn_value();
hn_rou[k][i] = F[i]->get_hn_value();
drou_hn_rou[k][i] = F[i]->get_drou_hn_value();
}
```

```
for( int i = 0; i < N; i++ )
delete F[i];
}


complex<double> rou_surface;
complex<double> cn_rou[N],dn_rou[N],an_rou[N],bn_rou[N];
rou_surface = 2*Pi*index_medium*g_Radius/LAMDA;


for(int i=0; i<N; i++)
  {
    F[i] = new field_intensity(rou_surface,0,i);
    if(i == 1){
      F[i]->set_F1(F[i-1]);
    }
    if(i >= 2){
      F[i]->set_F1(F[i-1]);
      F[i]->set_F2(F[i-2]);
    }
    F[i] ->calculate_j_rou();
    F[i] ->calculate_coeff();
```

```
    cn_rou[i] = F[i]->get_cn_value();
    dn_rou[i] = F[i]->get_dn_value();
    an_rou[i] = F[i]->get_an_value();
    bn_rou[i] = F[i]->get_bn_value();
    cout<<"an["<<i<<"] = "<< an_rou[i]<<endl;
    cout<<"bn["<<i<<"] = "<<bn_rou[i]<<endl;
  }

for(int i = 0; i<N; i++)
  delete F[i];

/* declaraion */
complex<double> m_theta_comp[N], m_phi_comp[N];
complex<double> ms_theta_comp[N], ms_phi_comp[N];
complex<double> n_rou_comp[N], n_theta_comp[N], n_phi_comp[N];
complex<double> ns_rou_comp[N], ns_theta_comp[N], ns_phi_comp[N];
complex<double> e_rou_comp, e_theta_comp, e_phi_comp;
complex<double> es_rou_comp, es_theta_comp, es_phi_comp;
complex<double> coeff; // 1, (0, 1), -1, (0, -1) = i^n
```

```
double phi;
double intensity_value, intensity_scatter_value, power_scatter_value;

for( int k = 1; k < PHI_N; k++ )
{
phi = 2 * Pi * k / PHI_N;

for( int j = 1; j < THETA_N; j++ )
{

theta = Pi * j / THETA_N;

for( int i = 1; i < ROU_N; i++)
{

rou = (i+rou_outer) * 2 * Pi * index_medium*g_Radius / LAMDA ;
for( int m = 1; m < N; m++ )
{
m_theta_comp[m] =
cos(phi)/sin(theta)*pn1_theta[j][m]*jn_rou[i][m];
```

```
ms_theta_comp[m] =
        cos(phi)/sin(theta)*pn1_theta[j][m]*hn_rou[i][m];
m_phi_comp[m] =
-sin(phi)*dpn1_dtheta[j][m]*jn_rou[i][m];
ms_phi_comp[m] =
        -sin(phi)*dpn1_dtheta[j][m]*hn_rou[i][m];
n_rou_comp[m] =
jn_rou[i][m]*cos(phi)*m*(m+1)*pn1_theta[j][m]/rou;
ns_rou_comp[m] =
        hn_rou[i][m]*cos(phi)*m*(m+1)*pn1_theta[j][m]/rou;
n_theta_comp[m] =
cos(phi)*dpn1_dtheta[j][m]*drou_jn_rou[i][m]/rou;
ns_theta_comp[m] =
        cos(phi)*dpn1_dtheta[j][m]*drou_hn_rou[i][m]/rou;
n_phi_comp[m] =
-sin(phi)*pn1_theta[j][m]*drou_jn_rou[i][m]/rou/sin(theta);
ns_phi_comp[m] =
        -sin(phi)*pn1_theta[j][m]*drou_hn_rou[i][m]/rou/sin(theta);
}
e_rou_comp = 0;
```

```
e_theta_comp = 0;

e_phi_comp = 0;

es_rou_comp = 0;

es_theta_comp = 0;

es_phi_comp = 0;

for( int m = 1; m < N; m++ )

{

switch( m % 4 )

{

case 0:

coeff = 1;

break;

case 1:

coeff = pure_imag;

break;

case 2:

coeff = -1;

break;

case 3:

coeff = -pure_imag;
```

```
break;
}
e_rou_comp += -coeff*(2*m+1)/m/(m+1)
* pure_imag*dn_rou[m]*n_rou_comp[m];
es_rou_comp += coeff*(2*m+1)/m/(m+1)
*pure_imag*an_rou[m]*ns_rou_comp[m];
e_theta_comp += coeff*(2*m+1)/m/(m+1)
* (cn_rou[m]*m_theta_comp[m] - pure_imag*dn_rou[m]*n_theta_comp[m]);
es_theta_comp += coeff*(2*m+1)/m/(m+1)*(pure_imag*an_rou[m]
*ns_theta_comp[m] - bn_rou[m]*ms_theta_comp[m]);
e_phi_comp += coeff*(2*m+1)/m/(m+1)
* (cn_rou[m]*m_phi_comp[m] - pure_imag*dn_rou[m]*n_phi_comp[m]);
es_phi_comp += coeff*(2*m+1)/m/(m+1)*(pure_imag*an_rou[m]
*ns_phi_comp[m] - bn_rou[m]*ms_phi_comp[m]);
}
intensity_value =
norm(e_rou_comp) + norm(e_theta_comp) + norm(e_phi_comp);
intensity_scatter_value =
        norm(es_rou_comp) + norm(es_theta_comp) + norm(es_phi_comp);
power_scatter_value = norm(rou)*intensity_scatter_value;
```

```
// k is phi, j is theta, i is rou
outFile << k << "\t" << j << "\t" << i << "\t" << power_scatter_value
<< endl;
}
}
}
outFile.close();
}
```

Bibliography

[1] M. Kerker, *The Scattering of Light and Other Electromagnetic Radiation* (Academic Press, Inc., New York, 1969).

[2] C. F. Bohren and D. R. Huffman, *Absorption and Scattering of Light by Small Particle* (John Wiley & Sons, Inc., New York, 1983).

[3] M. S. Yeganeh, J. Qi, A. G. Yodh, and M. C. Tamargo, Phys. Rev. Lett. **69**, 3579 (1992).

[4] M. S. Yeganeh, J. Qi, J. P. Culver, A. G. Yodh, and M. C. Tamargo, Phys. Rev. B **49**, 11196 (1994).

[5] J. Qi, W. Angerer, M. S. Yeganeh, A. G. Yodh, and W. M. Theis, Phys. Rev. Lett. **75**, 3174 (1995).

[6] J. Qi, W. Angerer, M. S. Yeganeh, A. G. Yodh, and W. M. Theis, Phys. Rev. B **51**, 13533 (1995).

[7] W. E. Angerer, N. Yang, A. G. Yodh, M. A. Khan, and C. J. Sun, Phys. Rev. B **59**, 2932 (1999).

[8] J. A. Giordmaine, Phys. Rev. **138**, A1599 (1965).

[9] R. W. Terhune, P. D. Maker, and C. M. Savage, Phys. Rev. Lett. **14**, 681 (1965).

[10] R.Bersohn, Y.-H. Pao, and H. L. Frisch, J. Chem. Phys. **45**, 3184 (1966).

[11] S. Kielich, J. R. Lalanne, and F. B. Martin, Phys. Rev. Lett. **26**, 1295 (1971).

[12] K. clays and A. Persoons, Phys. Rev. Lett. **66**, 2980 (1991).

[13] S. Houbrechts, K. clays, A. Persoons, Z. Pikramenou, and J.-M. Lehn, Chem. Phys. Lett. **258**, 485 (1996).

[14] G. Olbrechts, E. J. H. Put, K. Clays, A. Persoons, and N. Matsuda, Chem. Phys. Lett. **253**, 135 (1996).

[15] T. Kodaira, A. Watanabe, O. Ito, M. Matsuda, K. Clays, and A. Persoons, Jpn. J. Appl. Phys. I **35**, 6074 (1996).

[16] K. Clays, G. Olbrechts, and A. Persoons, Chem. Phys. Lett. **288**, 171 (1998).

[17] K. D. Singer and A. F. Garito, J. Chem. Phys. **75**, 3572 (1981).

[18] C. C. Teng and A. F. Garito, Phys. Rev. Lett. **50**, 350 (1983).

[19] S. Stadler, R. Dietrich, G. Bourhill, C. Bräuchle, A. Pawlik, and W. Grahn, Chem. Phys. Lett. **247**, 271 (1995).

[20] M. C. Flipse, R. de Jonge, R. H. Woudenberg, A. W. Marsman, C. A. van Walree, and L. W. Jenneskens, Chem. Phys. Lett. **245**, 297 (1995).

[21] O. K. Song, C. H. Wang, B. R. Cho, and J. T. Je, J. Phys. Chem. **99**, 6808 (1995).

[22] S. Stadler, G. Bourhill, and C. Bräuchle, J. Phys. Chem. **100**, 6927 (1996).

[23] P. Allcock, D. L. Andrews, S. R. Meech, and A. J. Wigman, Phys. Rev. A **53**, 2788 (1996).

[24] M. A. Pauley and C. H. Wang, Chem. Phys. Lett. **280**, 544 (1997).

[25] F. W. Vance, B. I. Lemon, and J. T. Hupp, J. Phys. Chem. B **102**, 10091 (1998).

[26] D. L. Andrews, P. Allcock, and A. A. Demidov, Chem. Phys. **190**, 1 (1995).

[27] G. J. T. Heesink, A. G. T. Ruiter, N. F. van Hulst, and B. Bölger, Phys. Rev. Lett. **71**, 999 (1993).

[28] B. F. Levine and C. G. Bethea, J. Chem. Phys. **65**, 2429 (1976).

[29] R. Cammi, B. Mennucci, and J. Tomasi, J. Phys. Chem. A **104**, 4690 (2000).

[30] S. J. Cyvin, J. E. Rauch, and J. C. Decius, J. Chem. Phys. **43**, 4083 (1965).

[31] W. P. Acker, D. H. Leach, and R. K. Chang, Chem. Phys. Lett. **155**, 491 (1989).

[32] H. Wang, E. C. Y. Yan, E. Borguet, and K. B. Eisenthal, Chem. Phys. Lett. **259**, 15 (1996).

[33] J. M. Hartings, A. Poon, X. Pu, R. K. Chang, and T. M. Leslie, Chem. Phys. Lett. **281**, 389 (1997).

[34] J. Martorell, R. Vilaseca, and R. Corbalán, Phys. Rev. A **55**, 4520 (1997).

[35] E. C. Y. Yan, Y. Liu, and K. B. Eisenthal, J. Phys. Chem. B **102**, 6331 (1998).

[36] H. Wang, E. C. Y. Yan, Y. Liu, and K. B. Eisenthal, J. Phys. Chem. B **102**, 4446 (1998).

[37] C. S. Yang, H. W. Tom, and M. A. Anderson, in *Centennial Meeting Bulletin of The American Physical Society* (American Physical Society, Atlanta, Georgia, 1999), vol. 44, p. 1580.

[38] J. I. Dadap, J. Shan, K. B. Eisenthal, and T. F. Heinz, Phys. Rev. Lett. **83**, 4045 (1999).

[39] R. Hellwarth and P. Christensen, Opt. Comm. **12**, 318 (1974).

[40] R. Hellwarth and P. Christensen, Appl. Opt. **12**, 247 (1975).

[41] J. R. Sheppard and R. Kompfner, Appl. Opt. **17**, 2879 (1978).

[42] K. A. Schultz, I. I. Suni, and E. G. Seebauer, J. Opt. Soc. Am. B **10**, 546 (1993).

[43] J. Deitche, M. Kempe, and W. Rudolph, J. Microscopy **174**, 69 (1994).

[44] M. Florsheimer, H. Looser, M. Kupfer, and P. Gunter, Thin Solid Films **244**, 1001 (1994).

[45] Y. Uesu, S. Kurimura, and Y. Yamamoto, Appl. Phys. Lett. **66**, 2165 (1995).

[46] V. Kirilyuk, A. Kirilyuk, and T. Rasing, Appl. Phys. Lett. **70**, 2306 (1997).

[47] Y. Guo, P. P. Ho, H. Savage, D. Harris, P. Sacks, S. Schantz, F. Liu, N. Zhadin, and R. R. Alfano, Opt. Lett. **22**, 1323 (1997).

[48] Y. R. Shen, *The Principles of Nonlinear Optics* (John Wiley & Sons, Inc., New York, 1984).

[49] M. S. Yeganeh, *Nonlinear Optical Spectroscopy of Solid/Solid Interfaces*, Ph.D. thesis, University of Pennsylvania (1992).

[50] J. Qi, *Nonlinear Optical Spectroscopy of Gallium Arsinide Interfaces*, Ph.D. thesis, University of Pennsylvania (1995).

[51] W. E. Angerer, *SHG Spectroscopy of Gallium Nitride Thin Films On Sapphire With Ultrashort Pulses*, Ph.D. thesis, University of Pennsylvania (1998).

[52] R. W. Boyd, *Nonlinear Optics* (Academic Press, Inc., San Diego, 1992).

[53] N. Bloembergen, R. K. Chang, S. S. Jha, and C. H. Lee, Phys. Rev. **174**, 813 (1968).

[54] J. A. Litwin, J. E. Sipe, and H. M. van Driel, Phys. Rev. B **31**, 5543 (1983).

[55] P. Guyot-Sionnest, W. Chen, and Y. R. Shen, Phys. Rev. B **33**, 8254 (1986).

[56] J. E. Sipe, D. J. Moss, and H. M. van Driel, Phys. Rev. B **35**, 1129 (1987).

[57] J. D. Jackson, *Classical Electrodynamics* (John Wiley & Sons, Inc., 1975), 2nd ed.

[58] W. H. Carter, J. Opt. Soc. Am. **62**, 1195 (1972).

[59] W. H. Carter, App. Opt. **12**, 1732 (1973).

[60] P. W. Milonni and J. H. Eberly, *Lasers* (John Wiley & Sons, New York, 1988).

[61] M. Maier, W. Kaiser, and J. A. Giordmaine, Phys. Rev. Lett. **17**, 1275 (1966).

[62] J. A. Armstrong, Appl. Phys. Lett. **10**, 16 (1967).

[63] E. P. Ippen and C. V. Shank, in *Ultrashort Light Pulses*, edited by S. L. Shapiro (Springer-Verlag, New York, 1977), pp. 83–122.

[64] K. L. Sala, G. A. Kenney-Wallace, and G. E. Hall, IEEE J. Quan. Elec. **QE-16**, 990 (1980).

[65] From the Coherent Inc. technical notes.

[66] R. J. Goldacre and J. N. Phillips, J. Chem. Soc. **Part III**, 1724 (1949).

[67] *Sigma-Aldrich Handbook of Stains, Dyes and Indicators* (Sigma Chemical Company, St. Louis, 1982).

[68] Private communications with Dr. Hongfei Wang.

[69] V. Sundström, T. Gillbro, and H. Bergström, Chem. Phys. **73**, 439 (1982).

[70] T. Doust, Chem. Phys. Lett. **96**, 522 (1983).

[71] D. Ben-Amotz and C. B. Harris, J. Chem. Phys. **86**, 4856 (1987).

[72] D. J. Erskine, A. J. Taylor, and C. L. Tang, J. Chem. Phys. **80**, 5338 (1984).

[73] D. Ben-Amotz and C. B. Harris, Chem. Phys. Lett. **119**, 305 (1985).

[74] R. Menzel, C. W. Hoganson, and M. W. Windsor, Chem. Phys. Lett. **120**, 29 (1985).

[75] D. Ben-Amotz and C. B. Harris, in *Ultrafast Phenomena V*, edited by G. R. Fleming and A. E. Siegman (Springer, New York, 1986).

[76] G. Oster and Y. Nishijima, J. Am. Chem. Soc. **78**, 1581 (1956).

[77] T. Forster and G. Hoffmann, Z. Phys. Chem. **NF 75**, 63 (1971).

[78] C. J. Mastangelo and M. W. Offen, Chem. Phys. Lett. **46**, 588 (1977).

[79] L. A. Brey, G. B. Schuster, and H. G. Dricamer, J. Chem. Phys. **67**, 2648 (1977).

[80] S. R. Meech and K. Yoshihara, Chem. Phys. Lett. **174**, 423 (1990).

[81] M. J. E. Morgenthaler and S. R. Meech, Chem. Phys. Lett. **202**, 57 (1993).

[82] X. Shi, E. Borguet, A. N. Tarnovsky, and K. B. Eisenthal, Chem. Phys. **205**, 167 (1996).

[83] M. Yoshizawa, K. Suzuki, A. Kubo, and S. Saikan, Chem. Phys. Lett. **290**, 43 (1998).

[84] A. Marcano and F. G. Golding, J. Chem. Phys. **82**, 1242 (1985).

[85] A. Marcano and L. Aranguren, J. Appl. Phys. **62**, 3100 (1987).

[86] S. W. Ong, X. L. Zhao, and K. B. Eisenthal, Chem. Phys. Lett. **191**, 327 (1992).

[87] X. L. Zhao, S. W. Ong, and K. B. Eisenthal, Chem. Phys. Lett. p. 513 (1993).

[88] B. Chu, *Laser Light Scattering* (Academic Press, Inc., New York, 1991), 2nd ed.

[89] A. Janowski and J. Rzeszotarska, J. Lumin. **21**, 409 (1980).

[90] M. Yoshizawa, K. Suzuki, A. Kubo, and S. Saikan, Chem. Phys. Lett. **290**, 43 (1998).

[91] R. K. Chang and A. J. Campillo, *Optical Processes In Microcavities* (World Scientific, 1996).

[92] A. Ashkin, Science **210**, 1081 (1980).

[93] J. F. Owen, P. W. Barber, B. J. Messinger, and R. K. Chang, Opt. Lett. **6**, 272 (1981).

[94] P. R. Conwell, P. W. Barber, and C. K. Rushforth, J. Opt. Soc. Am. A **1**, 62 (1984).

[95] S.-X. Qian, J. B. Snow, H. ming Tzeng, and R. K. Chang, Science **231**, 486 (1986).

[96] J.-Z. Zhang and R. K. Chang, Opt. Lett. **13**, 916 (1988).

[97] S.-X. Qian and R. K. Chang, Opt. Lett. **11**, 371 (1986).

[98] S. C. Hill, D. H. Leach, and R. K. Chang, J. Opt. Soc. Am. B **10**, 16 (1993).

[99] W. P. Acker, D. H. Leach, and R. K. Chang, Opt. Lett. **14**, 402 (1989).

[100] J.-Z. Zhang and R. K. Chang, J. Opt. Soc. Am. B **6**, 151 (1989).

[101] S.-X. Qian, J. B. Snow, and R. K. Chang, Opt. Lett. **10**, 499 (1985).

[102] S.-X. Qian and R. K. Chang, Phys. Rev. Lett. **56**, 926 (1986).

[103] W.-F. Hsieh, J. biao Zheng, and R. K. Chang, Opt. Lett. **13**, 497 (1988).

[104] G. Chen, R. K. Chang, S. C. Hill, and P. W. Barber, Opt. Lett. **16**, 1269 (1991).

[105] S. C. Hill and R. E. Benner, J. Opt. Soc. Am. B **3**, 1509 (1986).

[106] S. C. Ching, H. M. Lai, and K. Young, J. Opt. Soc. Am. B **4**, 1995 (1987).

[107] S. C. Hill, C. K. Rushforth, R. E. Benner, and P. R. Conwell, Appl. Opt. **24**, 2380 (1985).

[108] A. B. Pluchino, Appl. Opt. **20**, 2986 (1981).

[109] P. Chýlek, J. T. Kiehl, and M. K. W. Ko, Appl. Opt. **17**, 3019 (1978).

[110] J. F. Owen, R. K. Chang, and P. W. Barber, Opt. Lett. **6**, 540 (1981).

[111] P. Chýlek, J. D. Pendleton, and R. G. Pinnick, Appl. Opt. **24**, 3940 (1985).

[112] D. S. Benincasa, P. W. Barber, J.-Z. Zhang, W.-F. Hsieh, and R. K. Chang, Appl. Opt. **26**, 1348 (1987).

[113] N. Yang, W. E. Angerer, and A. G. Yodh, in *Centennial Meeting Bulletin of The American Physical Society* (American Physical Society, Atlanta, Georgia, 1999), vol. 44, p. 1431.

[114] N. Yang, W. E. Angerer, and A. G. Yodh, in *Quantum Electronics and Laser Science Conference* (American Physical Society, Baltimore, Maryland, 1999), vol. QELS'99, p. 178.

[115] A. E. Siegman, *An introduction to Lasers and Masers* (McGraw-Hill, New York, 1971).

[116] A. Yariv, *Quantum Electronics* (Johns & Wiley, New York, 1975), 2nd ed.

[117] I. Langmuir, J. Am. Chem. Soc. **40**, 1361 (1981).

[118] R. J. Hunter, *Foundations of Colloid Science* (Clarendon Press, New York, 1992).

30

037 09

UMI
MICROFILMED 2001

INFORMATION TO USERS

This manuscript has been reproduced from the microfilm master. UMI films the text directly from the original or copy submitted. Thus, some thesis and dissertation copies are in typewriter face, while others may be from any type of computer printer.

The quality of this reproduction is dependent upon the quality of the copy submitted. Broken or indistinct print, colored or poor quality illustrations and photographs, print bleedthrough, substandard margins, and improper alignment can adversely affect reproduction.

In the unlikely event that the author did not send UMI a complete manuscript and there are missing pages, these will be noted. Also, if unauthorized copyright material had to be removed, a note will indicate the deletion.

Oversize materials (e.g., maps, drawings, charts) are reproduced by sectioning the original, beginning at the upper left-hand corner and continuing from left to right in equal sections with small overlaps.

Photographs included in the original manuscript have been reproduced xerographically in this copy. Higher quality 6" x 9" black and white photographic prints are available for any photographs or illustrations appearing in this copy for an additional charge. Contact UMI directly to order.

Bell & Howell Information and Learning
300 North Zeeb Road, Ann Arbor, MI 48106-1346 USA
800-521-0600

UMI®

ANGLE-RESOLVED SECOND HARMONIC LIGHT SCATTERING FROM COLLOIDAL SUSPENSIONS AND SECOND HARMONIC PARTICLE MICROSCOPY

Ningping Yang

A DISSERTATION

in

PHYSICS AND ASTRONOMY

Presented to the Faculties of the University of Pennsylvania in Partial Fulfillment of the Requirements for the Degree of Doctor of Philosophy

2001

Arjun G. Yodh

Supervisor of Dissertation

Randall D. Kamien

Graduate Group Chairperson

30

037 09

UMI
MICROFILMED 2001

INFORMATION TO USERS

This manuscript has been reproduced from the microfilm master. UMI films the text directly from the original or copy submitted. Thus, some thesis and dissertation copies are in typewriter face, while others may be from any type of computer printer.

The quality of this reproduction is dependent upon the quality of the copy submitted. Broken or indistinct print, colored or poor quality illustrations and photographs, print bleedthrough, substandard margins, and improper alignment can adversely affect reproduction.

In the unlikely event that the author did not send UMI a complete manuscript and there are missing pages, these will be noted. Also, if unauthorized copyright material had to be removed, a note will indicate the deletion.

Oversize materials (e.g., maps, drawings, charts) are reproduced by sectioning the original, beginning at the upper left-hand corner and continuing from left to right in equal sections with small overlaps.

Photographs included in the original manuscript have been reproduced xerographically in this copy. Higher quality 6" x 9" black and white photographic prints are available for any photographs or illustrations appearing in this copy for an additional charge. Contact UMI directly to order.

Bell & Howell Information and Learning
300 North Zeeb Road, Ann Arbor, MI 48106-1346 USA
800-521-0600

UMI®

ANGLE-RESOLVED SECOND HARMONIC LIGHT SCATTERING FROM COLLOIDAL SUSPENSIONS AND SECOND HARMONIC PARTICLE MICROSCOPY

Ningping Yang

A DISSERTATION

in

PHYSICS AND ASTRONOMY

Presented to the Faculties of the University of Pennsylvania in Partial Fulfillment of the Requirements for the Degree of Doctor of Philosophy

2001

Arjun G. Yodh

Supervisor of Dissertation

Randall D. Kamien

Graduate Group Chairperson

UMI Number: 3003709

UMI®

UMI Microform 3003709
Copyright 2001 by Bell & Howell Information and Learning Company.
All rights reserved. This microform edition is protected against
unauthorized copying under Title 17, United States Code.

Bell & Howell Information and Learning Company
300 North Zeeb Road
P.O. Box 1346
Ann Arbor, MI 48106-1346

30

037 09

UMI
MICROFILMED 2001

INFORMATION TO USERS

This manuscript has been reproduced from the microfilm master. UMI films the text directly from the original or copy submitted. Thus, some thesis and dissertation copies are in typewriter face, while others may be from any type of computer printer.

The quality of this reproduction is dependent upon the quality of the copy submitted. Broken or indistinct print, colored or poor quality illustrations and photographs, print bleedthrough, substandard margins, and improper alignment can adversely affect reproduction.

In the unlikely event that the author did not send UMI a complete manuscript and there are missing pages, these will be noted. Also, if unauthorized copyright material had to be removed, a note will indicate the deletion.

Oversize materials (e.g., maps, drawings, charts) are reproduced by sectioning the original, beginning at the upper left-hand corner and continuing from left to right in equal sections with small overlaps.

Photographs included in the original manuscript have been reproduced xerographically in this copy. Higher quality 6" x 9" black and white photographic prints are available for any photographs or illustrations appearing in this copy for an additional charge. Contact UMI directly to order.

Bell & Howell Information and Learning
300 North Zeeb Road, Ann Arbor, MI 48106-1346 USA
800-521-0600

UMI®

ANGLE-RESOLVED SECOND HARMONIC LIGHT SCATTERING FROM COLLOIDAL SUSPENSIONS AND SECOND HARMONIC PARTICLE MICROSCOPY

Ningping Yang

A DISSERTATION

in

PHYSICS AND ASTRONOMY

Presented to the Faculties of the University of Pennsylvania in Partial Fulfillment of the Requirements for the Degree of Doctor of Philosophy

2001

Arjun G. Yodh

Supervisor of Dissertation

Randall D. Kamien

Graduate Group Chairperson

30

03709

UMI

MICROFILMED 2001

INFORMATION TO USERS

This manuscript has been reproduced from the microfilm master. UMI films the text directly from the original or copy submitted. Thus, some thesis and dissertation copies are in typewriter face, while others may be from any type of computer printer.

The quality of this reproduction is dependent upon the quality of the copy submitted. Broken or indistinct print, colored or poor quality illustrations and photographs, print bleedthrough, substandard margins, and improper alignment can adversely affect reproduction.

In the unlikely event that the author did not send UMI a complete manuscript and there are missing pages, these will be noted. Also, if unauthorized copyright material had to be removed, a note will indicate the deletion.

Oversize materials (e.g., maps, drawings, charts) are reproduced by sectioning the original, beginning at the upper left-hand corner and continuing from left to right in equal sections with small overlaps.

Photographs included in the original manuscript have been reproduced xerographically in this copy. Higher quality 6" x 9" black and white photographic prints are available for any photographs or illustrations appearing in this copy for an additional charge. Contact UMI directly to order.

Bell & Howell Information and Learning
300 North Zeeb Road, Ann Arbor, MI 48106-1346 USA
800-521-0600

UMI®

ANGLE-RESOLVED SECOND HARMONIC LIGHT SCATTERING FROM COLLOIDAL SUSPENSIONS AND SECOND HARMONIC PARTICLE MICROSCOPY

Ningping Yang

A DISSERTATION

in

PHYSICS AND ASTRONOMY

Presented to the Faculties of the University of Pennsylvania in Partial Fulfillment of the Requirements for the Degree of Doctor of Philosophy

2001

Arjun G. Yodh

Supervisor of Dissertation

Randall D. Kamien

Graduate Group Chairperson